PFG

Photogrammetrie Fernerkundung Geoinformation

Journal for Photogrammetry, Remote Sensing and Geoinformation Science

Organ der Deutschen Gesellschaft für Photogrammetrie, Fernerkundung und Geoinformation (DGPF) e. V.

Jahrgang 2015, Heft 1

E. Schweizerbart'sche Verlagsbuchhandlung
(Nägele u. Obermiller) Stuttgart 2015

Deutsche Gesellschaft für Photogrammetrie, Fernerkundung
und Geoinformation (DGPF) e.V.
Gegründet 1909

Die *Deutsche Gesellschaft für Photogrammetrie, Fernerkundung und Geoinformation* (DGPF) e.V. unterstützt als Mitglieds- bzw. Trägergesellschaft die folgenden Dachverbände:

International Society
for Photogrammetry
and Remote Sensing

Deutsche Arbeits-
gemeinschaft für
Mustererkennung e.V.

GeoUnion
Alfred-Wegener-Stiftung

Herausgeber:

Präsident: Prof. Dr. Thomas Kolbe, Technische Universität München, Institut für Geodäsie, GIS und Landmanagement, Lehrstuhl für Geoinformatik, Arcisstraße 21, 80333 München, Germany, Tel. +49-89-289-23888
Geschäftsstelle: Tanja Nyc, c/o Technische Universität München, Institut für Geodäsie, GIS und Landmanagement, Lehrstuhl für Geoinformatik, Arcisstraße 21, 80333 München, Germany, Tel.: +49-89-289-22578, e-mail: geschaeftsstelle@dgpf.de
Published by: E. Schweizerbart'sche Verlagsbuchhandlung (Nägele u. Obermiller), Johannesstraße 3A, 70176 Stuttgart, Germany, Tel.: +49-711 351456-0, Fax: +49-711 351456-99, e-mail: mail@schweizerbart.de
Internet: http://www.schweizerbart.de
⊗ Gedruckt auf alterungsbeständigem Papier nach ISO 9706-1994

ISSN 1432-8364 / e-ISSN 2363-7145
Science Citation Index Expanded (also known as SciSearch®) Journal Citation Reports/Science Edition
Hauptschriftleiter: Prof. Dr.-Ing. Wolfgang Kresse, Hochschule Neubrandenburg, Fachbereich Landschaftswissenschaften und Geomatik, Brodaer Straße 2, 17033 Neubrandenburg, Germany, e-mail: kresse@hs-nb.de
Schriftleiter: Prof. Dr.-Ing. Stefan Hinz, Karlsruher Institut für Technologie – KIT, Institut für Photogrammetrie und Fernerkundung, Englerstraße 7, 76131 Karlsruhe, Germany, e-mail: stefan.hinz@ipf.uni-karlsruhe.de, Privatdozent Dr. techn. Franz Rottensteiner, Leibniz Universität Hannover, Institut für Photogrammetrie und GeoInformation, Nienburger Straße 1, 30167 Hannover, Germany, e-mail: rottensteiner@ipi.uni-hannover.de, Prof. Dr. rer. nat. Ulrich Michel, Pädagogische Hochschule Heidelberg, Czernyring 22/11–12, 69115 Heidelberg, Germany, e-mail: michel@ph-heidelberg.de, Prof. Dr. rer. nat. Lars Bernard, Technische Universität Dresden, Fachrichtung Geowissenschaften, Helmholtzstraße 10, 01062 Dresden, Germany, e-mail: lars.bernard@tu-dresden.de, und Dr.-Ing. Eckhardt Seyfert, Landesvermessung und Geobasisinformation Brandenburg, Heinrich-Mann-Allee 103, 14473 Potsdam, Germany, e-mail: eckhardt.seyfert@geobasis-bb.de
Erscheinungsweise: 6 Hefte pro Jahrgang.
Bezugspreis im Abonnement: € 249,– pro Jahrgang. Mitglieder der DGPF erhalten die Zeitschrift kostenlos. Der Online-Zugang ist im regulären Subskriptionspreis enthalten.
Anzeigenverwaltung: E. Schweizerbart'sche Verlagsbuchhandlung (Nägele u. Obermiller), Johannesstraße 3A, 70176 Stuttgart, Germany, Tel.: +49-711 351456-0; Fax: +49-711 351456-99.
e-mail: mail@schweizerbart.de, Internet: http://www.schweizerbart.de
Bernhard Harzer Verlag GmbH, Westmarkstraße 59/59a, 76227 Karlsruhe, Germany, Tel.: +49-721 944020, Fax: +49-721 9440230, e-mail: Info@harzer.de, Internet: www.harzer.de
Printed in Germany by Tutte Druckerei & Verlagsservice GmbH, 94121 Salzweg, Germany.

PFG – Jahrgang 2015, Heft 1
Inhaltsverzeichnis

Editorial

Originalbeiträge

Mitteilungen

Zusammenfassungen der „Originalbeiträge“ und der „Beiträge aus Wissenschaft und Praxis“ (deutsch und englisch) sind auch verfügbar unter www.dgpf.de/neu/pfg/ausgaben.htm

PFG 2015 / 1, 0005–0006
Stuttgart, February 2015

Editorial

Themenheft Fernerkundung für Agrarmonitoring

Dieses Themenheft der PFG präsentiert aktuelle Fortschritte aus dem Bereich Agrarmonitoring. Satellitenbild-Fernerkundung dient heute als zuverlässige und wertvolle Informationsquelle für die Landwirtschaft und zur Beobachtung der landwirtschaftlichen Produktion auf lokaler bis globaler Ebene. Die Fernerkundung kann zur genaueren, objektiven, schnellen und häufigen Erfassung von Agrardaten beitragen und Modelle für landwirtschaftliche Prognosen wie beispielsweise Ernteschätzungen ergänzen sowie den Zustand der Agrarflächen auf verschiedenen räumlichen und zeitlichen Skalen erfassen. Dennoch sieht sich die technologische Entwicklung immer noch vielfältigen Herausforderungen gegenüber.

Neben der steigenden Verfügbarkeit räumlich immer höher aufgelöster Daten stellt die Analyse multitemporaler und Multi-Sensor-Ansätze heute und zukünftig sehr interessante Herausforderungen für Forschung und Entwicklung dar. Zum einen können dadurch größere Klassifizierungsgenauigkeiten erzielt und künftig wohl auch das Monitoring landwirtschaftlicher Produktion (Ernte) mit hoher Detailschärfe durchgeführt werden. Jedoch stellt die Verarbeitung solcher Datensätze den Anwender oft vor große Herausforderungen, da Methoden zur Bewältigung solch großer Datenmengen entwickelt werden müssen. Durch den gestiegenen Bedarf nach operationalisierbaren Methoden für ein regelmäßiges Agrarmonitoring kommt zudem der räumlichen und zeitlichen Übertragbarkeit von Fernerkundungsmethoden immer mehr Bedeutung zu. Durch die Auswertung von Satellitenbild-Archiven ist die Möglichkeit gegeben, vergangene Zustände von Agrarsystemen zu erfassen und deren raumzeitliche Veränderungen im Kontext sich verändernder sozioökonomischer oder Umweltbedingungen zu untersuchen. Fernerkundungsbasiertes Agrarmonitoring ist daher durch folgende Schwerpunkte gekennzeichnet:

- Methoden zur multiskaligen und multitemporalen Landnutzungsklassifizierung
- Synergetischer Nutzen von Multi-Sensor-Daten (optisch, Radar, hyperspektral)
- Einsatz von Lidar-Technologie
- Erkennung und Quantifizierung von Zustandsveränderung sowie agrarischer Landnutzungsdynamik
- Ableitung von feldfruchtspezifischen biophysikalischen Parametern als Grundlage für das Monitoring von landwirtschaftlicher Produktion (Ernte)
- Nutzung von Unmanned Aerial Vehicles (UAVs) und Precision Farming

In den letzten Jahren wurden erfolgreich verschiedene Fernerkundungsmethoden entwickelt, welche zur Unterstützung und Aktualisierung bestehender Landnutzungsdaten und Modelle entscheidend sind. In dieser Ausgabe stellen wir Methoden und Forschungsergebnisse aus verschiedenen Bereichen des Agrarmonitorings vor. Die vorliegenden Beiträge dieses Themenhefts decken die oben aufgeführten Bereiche bereits teilweise ab und zeigen somit ein breites Spektrum des Agrarmonitorings auf. Die Artikel sind thematisch wie folgt gegliedert: Multitemporale Feldfruchtklassifizierung, Landnutzungsveränderung und Ableitung biophysikalischer Parameter.

Im einführenden Artikel *Impact of Categorical and Spatial Scale on Supervised Crop Classification using Remote Sensing* präsentieren Fabian Löw, Grégory Duveiller, Christopher Conrad und Ulrich Michel eine Methode, um für verschiedene Agrarlandschaften quantitativ geeignete Charakteristika von Fernerkundungsdaten hinsichtlich Pixelgröße- und -reinheit in Bezug auf die Identifizierung von Feldfrüchten zu definieren. Die vorgestellte Methode kann im Kontext von satellitengestütztem Agrarmonitoring genutzt werden, um Empfehlungen für die Wahl von geeigneten Pixelgrößen und Sensoren sowie auch geeigneter Klassenschlüssel zu formulieren.

Florian Beyer, Thomas Jarmer und Bastian Siegmann untersuchen in ihrem Beitrag *Identification of Agricultural Crop Types in Northern Israel using Multitemporal Rapid-*

www.schweizerbart.de
DOI: 10.1127/pfg/2015/0254 1432-8364/15/0254 $ 0.50

Eye Data den Einfluss der Anzahl und der Aufnahmezeitpunkte von optischen Satellitenbilddaten auf die Klassifizierungsgenauigkeit. Sie verwendeten das Trennbarkeitsmaß *Jeffries-Matusita Separability*, um den besten multitemporalen Datensatz aus den verfügbaren einzelnen Aufnahmezeitpunkten für die Klassifizierung mittels *Support Vector Machines* zu ermitteln.

Eine mehrjährige Landnutzungsanalyse zur Dokumentation des landwirtschaftlichen Wandels auf Teneriffa wird in dem Beitrag *Multitemporale und kantenbasierte Analyseverfahren zur Detektion agrarischer Landnutzungsdynamiken auf Teneriffa* von Sebastian Günthert, Simone Naumann und Alexander Siegmund vorgestellt. Die agrarischen Landnutzungsdynamiken werden durch eine quantitative Auswertung objektbasierter Landnutzungsklassifizierungen mittels Multi-Sensor-Daten erfasst und durch einen modifizierten multitemporalen Post-Klassifizierungs-Vergleich analysiert. Hauptaugenmerk dieses Verfahrens liegt auf der texturbasierten Detektion von Agrarflächen inklusive landwirtschaftlich stillgelegter Areale bzw. Sukzessionsbrachen.

In dem Aufsatz *Estimate Leaf Chlorophyll of Rice Using Reflectance Indices and Partial Least Squares* von Kang Yu, Martin Leon Gnyp, Lei Gao, Yuxin Miao, Xinping Chen und Georg Bareth wurde das Potential optimierter Spektralindizes und *Partial Least Squares* zur Ableitung des Chlorophyllgehalts im Blatt von Reis untersucht. Die Ergebnisse zeigen das Potential zur Optimierung von spektralen Indizes sowie der Verwendung von *Partial Least Squares* für die Bestandskartierung von biochemischen Variationen.

Der Beitrag *Comparison of two Statistical Methods for the Derivation of the Fraction of Absorbed Photosynthetic Active Radiation for Cotton* von Sylvia Lex, Sarah Asam, Fabian Löw und Christopher Conrad stellt einen Vergleich von zwei statistischen Verfahren zur Ableitung des biophysikalischen Parameters „Anteil absorbierter Photosynthese-wirksamer Strahlung“ (FAPAR) für Baumwolle vor und vergleicht direse in zwei Studiengebieten. Die direkte Ableitung von FAPAR mittels Umskalierung des *Normalized Difference Vegetation Index* im *Perzentil-Ansatz* ohne Hinzunahme von Felddaten erzielte ähnliche Genauigkeiten wie die empirische Regression von FAPAR-Feldmessungen mit dem NDVI, was auf eine gute Eignung des vergleichsweise einfachen Perzentil-Ansatzes als Alternative zu messdatenintensiven Methoden zur Bestimmung von FAPAR auf Baumwollfeldern rückschließen lässt.

Der abschließende Beitrag des Themenhefts, *Low-Weight and UAV-Based Hyperspectral Full-Frame Cameras for Monitoring Crops: Spectral Comparison with Portable Spectroradiometer Measurements*, von Georg Bareth, Helge Aasen, Juliane Bendig, Martin Leon Gnyp, Andreas Bolten, András Jung, René Michels und Jussi Soukkamäki zeigt die Anwendung von zwei durch leichte Unmanned Aerial Vehicles (UAV) getragene hyperspektrale, bildgebende Kameras zur Beobachtung von landwirtschaftlichen Pflanzenbeständen. Die Ergebnisse zeigen, dass die Kombination von 3D-Bildverarbeitungsverfahren sowie räumlich und zeitlich hochaufgelösten hyperspektralen Bilddaten ein genaues Monitoring des Pflanzenwachstums ermöglicht.

Im weiteren Beitrag *Comparison of SVM and Boosted Regression Trees for the Delineation of Lacustrine Sediments using Multispectral ASTER Data and Topographic Indices in the Lake Manyara Basin* präsentieren Felix Bachofer, Geraldine Quénéhervé, Michael Märker und Volker Hochschild einen Vergleich des Stützvektorverfahrens mit einem Klassifizierungsbaum-Ansatz zur überwachten Klassifizierung von lakustrinen Sedimenten basierend auf multispektralen ASTER Daten und topographischen Parametern von SRTM-X Höhendaten. Obwohl die Klassifizierungsgenauigkeiten beider Verfahren ähnlich hoch waren, lieferte das Stützvektorverfahren durchgängig bessere Ergebnisse.

Fabian Löw, Würzburg und
Ulrich Michel, Heidelberg

Am Ende des Heftes finden wir den Artikel von Paul Czioska, in dem er einen Algorithmus zur Herstellung eines topologisch sauberen Netzes von Bahnlinien aus OpenStreetMap-Daten vorstellt. Dieser Artikel ist aus einem Vortrag bei der DGPF-Jahrestagung 2013 hervorgegangen.

Wolfgang Kresse, Neubrandenburg

PFG 2015 / 1, 0007–0020
Stuttgart, February 2015

Article

Impact of Categorical and Spatial Scale on Supervised Crop Classification using Remote Sensing

Fabian Löw, Würzburg, Grégory Duveiller, Ispra, Italy, Christopher Conrad, Würzburg & Ulrich Michel, Heidelberg

Keywords: agricultural monitoring, crop classification, categorical scale, spatial scale, pixel purity

Summary: High temporal revisit frequency over vast geographic areas is necessary to properly use satellite earth observation for monitoring agricultural production. However, this often limits the spatial resolution that can be used. The challenge of discriminating pixels that correspond to a particular crop type, a prerequisite for crop specific monitoring remains daunting when the signal encoded in pixels stems from several land uses (mixed pixels). Naturally, the concept of spatial scale arises but the issue of selecting a proper class legend (the categorical scale) should not be neglected. A framework is presented that addresses these issues and that can be used to quantitatively define pixel size requirements for crop identification and to assess the effect of categorical scale. The framework was applied over two agricultural landscapes. It was demonstrated that there was no unique spatial resolution that provided the best classification result for all classes at once at a given categorical scale. The suitability of pixel populations characterized by pixel size and purity differed for identifying specific crops within tested landscapes, and for one crop there were large differences among the landscapes. In the context of agricultural crop growth monitoring the framework described above can be used to draw guidelines for selecting appropriate imagery, e.g. suitable pixel sizes, and for selecting class legends suitable for accurate crop classification when the interest is only on pixels covering arable land as a prerequisite for crop specific monitoring. The framework could be used to plot the suitability (or accuracy) of pixels as a function of their purity to provide a spatial assessment of classification performance.

Zusammenfassung: *Einfluss der thematischen und räumlichen Auflösung auf die überwachte, fernerkundungsbasierte Feldfrucht-Klassifizierung.* Häufige und regelmäßige Aufnahmen über großen Gebieten sind wichtige Voraussetzungen für das Monitoring von Agrarproduktion basierend auf Erdbeobachtungsdaten. Jedoch schränken diese Voraussetzungen oftmals die räumliche Auflösung (Pixelgröße) ein, welche von bestehenden Sensorsystemen genutzt werden kann. Die Unterscheidung unterschiedlicher Landnutzungstypen, eine Voraussetzung für ein Feldfrucht spezifisches Monitoring, mittels Klassifizierung wird erschwert, wenn das in einem Pixel kodierte Signal von mehreren Landnutzungstypen stammt (Mischpixel-Problematik). Dies wirft Fragen bezüglich der Wahl der optimalen Pixelgröße, aber auch der thematischen Auflösung, also eines geeigneten Klassenschlüssels auf. Um diese Fragen zu beantworten, wird eine Methode vorgestellt, um quantitativ geeignete Charakteristika von Pixelpopulationen hinsichtlich deren Größe und Reinheit in Bezug auf die zu klassifizierende Klasse zu bestimmen. Zudem wurde der Einfluss von verschiedenen Klassenschlüsseln auf das Klassifizierungsergebnis untersucht. Die Methode wurde in zwei landwirtschaftlich genutzten Gebieten getestet. Es wurde gezeigt, dass es keine spezifische „optimale" Pixelgröße gibt, welche für alle Klassen und bei einem bestimmten Klassenschlüssel gleichermaßen das beste Klassifizierungsergebnis liefert. Die Eignung von Pixelpopulationen charakterisiert durch Pixelgröße und -reinheit unterschied sich innerhalb einer bestimmten Landschaft für verschiedene Landnutzungsklassen bzw. für eine spezifische Klasse in verschiedenen Landschaften deutlich. Die vorgestellte Methode kann im Kontext von satellitengestütztem Agrar-Monitoring genutzt werden, um Empfehlungen für die Wahl von geeigneten Pixelgrößen und Sensoren sowie auch geeigneter Klassenschlüssel zu formulieren.

 www.schweizerbart.de
DOI: 10.1127/pfg/2015/0252 1432-8364/15/0252 $ 3.50

1 Introduction

Crop type identification and discrimination are essential for subsequent crop-specific agricultural production monitoring using satellite earth observation (EO), e.g. when crop maps are used as input for agricultural modelling. However, the high temporal revisit frequency and the large geographic swath that are required to do a proper monitoring often limit the spatial resolution that can be used. An instrument that satisfies the criteria of swath and revisit frequency is MODIS, but its spatial resolution of 250/500 m is often coarser than desired for many agricultural landscapes. When such data is used as input for crop classification, its coarse observation supports can lead to non-detection of certain land use fragments, e.g. when individual fields of a certain crop type are smaller than individual pixels and the signal encoded in coarser pixels stems from several land uses (mixed pixels). The question of determining the optimal pixel size for an application such as crop identification is therefore inclined towards finding the coarsest acceptable pixel sizes.

When discussing spatial scale, the issue of the choice of a categorical scale, e.g. the number and type of classes used in classification, or class legend, naturally arises and should not be neglected (Ju et al. 2005). In general it would be desirable to have all land use types in a landscape included in the class legend. In reality, however, not all classes will be present in all regions of an image at all scales and there is indication in the literature that there exist different ranges of "optimal" pixel sizes for different classes (Aplin 2006). When selecting coarser pixels the spatial scale increases relative to the patch sizes, e.g. size of agricultural fields, in the underlying landscape and forces to use labels of coarser categorical scale, e.g. "arable land" instead of land use types like "rice" or "wheat" (Ju et al. 2005). In such a situation classification quality can deteriorate when selecting pixel sizes that are too coarse since this can result in excessive mixed pixels when the heterogeneity of the land cover class in one pixel increases (Hsieh et al. 2001, Smith et al. 2003). Selecting too small pixels can result in increased within class variability. Such variation can lead to errors in the class identification (Atkinson & Aplin 2004, Cushnie 1987, Hsieh et al. 2001), and better classification accuracies may sometimes be attained using coarser pixel sizes (McCloy & Bøcher 2007). The issue of pixel size and its implications for image classification have long been noted (Hsieh et al. 2001, Marceau et al. 1994a, McCloy & Bøcher 2007, Woodcock & Strahler 1987) and the selection of one single optimal scale has been questioned (Aplin 2006, Levin 1992). Yet, the effect of categorical scale in combination with spatial scale has been analysed to a lesser extent. Marceau et al. (1994b) demonstrated for different pixel sizes that the definition of the categorical scale can considerably influence classification accuracy. It was shown that the range of pixel sizes for which maximum accuracy can be achieved is specific to certain land cover categories (McCloy & Bøcher 2007). Ju et al. (2005) suggested a method to jointly adapt spatial, e.g. pixel size, and categorical scale in an object-based context. But the dominant standard in remote sensing classification studies often remained being a classification at a single spatial and a fixed categorical scale, i.e. with category labels from only one level of a potential categorical hierarchy (Ju et al. 2005).

But what type of remote sensing data with respect to spatial resolution should be used as classification input and what is the impact of categorical scale on the definition of suitable pixel sizes? To answer these questions, this study builds upon a previous framework by Löw & Duveiller (2014), which was used to quantitatively define pixel size requirements for crop identification via image classification. In this study, this framework will be extended to assess the impact of categorical scale and to explore trade-offs between pixel size and pixel purity when addressing the question of crop classification via image classification. The analysis is restricted to pixels covering arable land using a dedicated masking procedure, based on high-resolution data and simulating how much crop specific signal is encoded in coarser pixels. This procedure restricts the analysis to a subset of the region's pixels to better explore the effect of pixel purity on crop classification, thereby allowing to draw guidelines for selecting suitable class legends and

pixel sizes, respectively. More specifically, this study assesses the impact of the categorical scale on crop classification accuracy in different agricultural landscapes, using satellite images with different pixel sizes as classification input. Second, the impact of the categorical scale on the definition of suitable pixel sizes for crop classification, e.g. maximum and minimum tolerable pixel sizes, is analysed.

2 Study Area

This study is based on two contrasting agro-ecological landscapes in Central Asia. They are located between the Amu-Darya and Syr-Darya Rivers. They are characterized by vast agricultural systems, which were extensively developed under the aegis of the former Soviet Union during the second half of the 20th century. Each test site is 30 km × 30 km.

The first site is located in the Khorezm region (KHO) in the north-western part of Uzbekistan. The agricultural landscape appears heterogeneous due to a comparatively high diversity of crops, e.g. cotton, rice, sorghum, maize, winter wheat, and fruit trees. Cover fraction (C_f, the fraction of the sites covered by agricultural fields) is high (Tab. 1). Multiple cropping is sometimes practiced, e.g. growing sequentially two or more crops in the same field within a single growing season, typically starting with wheat and following with another crop. In this study, such land use type will be labelled: "wheat-other".

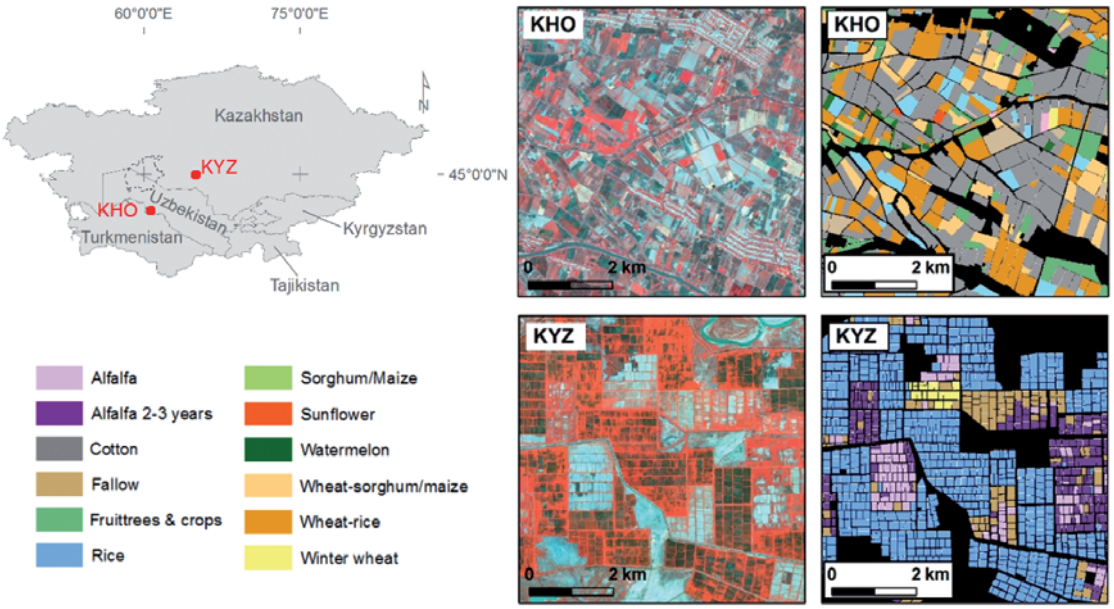

Fig. 1: Subsets (6.5 km × 6.5 km) of the satellite imagery and crop masks illustrating the typical cropping patterns within the two test sites Khorezm (KHO) in Uzbekistan and Kyzyl-Orda (KYZ) in Kazakhstan. The imagery is displayed using a near-infrared-green-blue band combination of the RapidEye sensor recorded in May.

Tab. 1: Characteristics of the four study sites. Total number of fields, field sizes and cover fractions C_f are based on own calculations based on segmented image objects.

Study site	Scene centre [Lat/Lon]	Total number of fields	Mean, median, and standard deviation of field size (ha)	C_f
KHO	60.69°E, 41.53°N	22,247	4.31, 3.21, 2.07	0.59
KYZ	64.55°E, 44.58°N	14,561	2.45, 2.14, 1.62	0.25

The second site is located in Kyzl-Orda (KYZ) in southern Kazakhstan, and was chosen to have an example with more regularly shaped field structures. Only few crops are dominating the agricultural landscape: rice and alfalfa. Large and regular shaped agricultural fields of approx. 2 ha – 3 ha each characterize this landscape, where the same crop is often grown on adjacent fields, that are aggregated to blocks which together exceed the area of between 500 m × 500 m and 1,000 m × 1,000 m (25 ha – 100 ha). Due to this pattern, the agricultural landscape in KYZ with smaller fields (2.45 ha) appears more homogeneous than in KHO with larger mean field sizes (4.31 ha).

3 Data and Methods

Images from the RapidEye mission with a ground sampling distance (GSD) of 6.5 m, were available for each site in 2011 (KYZ) and 2010 (KHO) (Fig. 2). These images have five spectral bands: blue (440 nm – 510 nm), green (520 nm – 590 nm), red (630 nm – 685 nm), red edge (690 nm – 730 nm), and near infrared (NIR, 760 nm – 850 nm). Images were atmospherically corrected using the ATCOR-2 module (Richter 2011), and geometrically corrected and co-registered with ground control points, resulting in RMSEs of < 6.5 m.

Crop specific masks are necessary to identify the target objects, i.e. agricultural fields cultivated with a certain crop, in the scene, and later for calculating the purity of coarser pixels with regard to specific crops. For the study sites access to vector databases of the agricultural fields including information on crops was either non-existent or restricted. Crop masks for the two sites were created according to the methodology described in Löw et al. (2012). These masks were created using supervised object-based image classification applied to a set of high-resolution time series of RapidEye images acquired over the growing seasons. The overall accuracies of the crop masks were more than reasonable (> 93%) and assumed to have a negligible error for the purpose of this study. Sorghum and maize in KHO were merged into the class "sorghum/maize" because they could not be distinguished from each other (Fig. 1).

3.1 *Simulating Coarser Images*

The methodology employed here is based on the same conceptual framework designed in a previous study for determining pixel size requirements for crop growth monitoring (Duveiller & Defourny 2010) that was extended by Löw & Duveiller (2014) for an application to crop classification. It relies on using high spatial resolution images and corresponding crop specific masks to generate various sets of pixel populations over which a classification step can be applied. The pixel populations are characterized by increasingly coarser pixel sizes and with a range of different crop specific purity thresholds. To simulate coarser pixel sizes, a spatial response model is convolved over the original RapidEye images. It consists of a point spread function (PSF) that characterizes both optical (PSF_{opt}) and detector (PSF_{det}) components of a generic sensor:

$$PSF_{net} = PSF_{opt} * PSF_{det}\,, \tag{1}$$

$$PSF_{opt}(x,y) = exp\left(-\frac{x^2+y^2}{2*(w*\sigma)^2}\right), \tag{2}$$

$$PSF_{det(x,y)} = rect(x-w) * rect(y-w). \tag{3}$$

Fig. 2: Acquisition dates of the datasets from the RapidEye instrument utilised in this study.

where x and y are the cross-track and in-track coordinates, respectively, in the image space with their origin at the centroid of the ground instantaneous field of view (GIFOV), w the width of the optics, and σ the standard deviation of the Gaussian curve. Note that the width of the detector in both in-track and cross-track directions, respectively, is assumed to be equal. *rect* is the rectangular function, a uniform square pulse function with amplitude one and width w. The simulation was done in increments of 6.5 m, in order to simulate a continuum of coarser images, with pixel sizes ranging from 6.5 m – 747.5 m. More information on the simulation of coarser data in this framework can be found in Duveiller & Defourny (2010).

As mentioned in the introduction this study focuses on detecting and discriminating agricultural fields of specific crops within successively coarser pixels. In order to select pixels covering arable land and to further assess the effect of pixel purity on crop classification accuracy, the convolution of the same spatial response model over the high-resolution crop masks was performed. This produced crop specific "purity maps" at each scale, which map the pixel purity with respect to the spatial structures represented in the high resolution crop masks (Duveiller & Defourny 2010). This allows controlling the degree at which the footprints of coarser pixels coincide with the target structures, e.g. fields belonging to certain crops. At each spatial resolution, pixel populations can be selected based on thresholds on the pixel purity, here denoted π. A threshold can be chosen to separate the aggregated binary crop masks into two sets: target pixels and non-target pixels. The threshold can vary from 0, where all pixels in the images are selected as target, to 1, where only completely pure pixels, e.g. pixels lying completely within agricultural fields are selected. The results are the sets of selected target pixels, or "pixel populations", defined by their pixel size (v) and by the minimum acceptable purity threshold that defines them (π).

3.2 *Image Classification*

The second step consists in applying supervised classification procedures to the pixel populations selected in the previous step. The implementation of Breiman's RF (Breiman 2001) within the randomForest package (Liaw 2013) in the R programming environment was used for the classification in this study. The number of trees in the ensemble was set to a relatively high value of 500 so that the out-of-bag error (OOB) converges. OOB is calculated based on roughly 1/3 of the reference data, which are withheld from tree construction and used to calculate an error matrix and unbiased estimate of accuracy (Liaw & Wiener 2002). The remainder 2/3 of the reference data is used to build each tree. The number of features at each split node was set to the square root of the total number of input features $\sqrt{f}$ where f is the number of predictor variables within the corresponding input dataset. The NDVI and EVI plus RapidEye bands were the input to the classification, calculated for eight acquisition dates (f = 56). At each spatial scale and for each pixel purity threshold (here from 0 to 1 in increments of 0.05), independent training and testing datasets were generated following an equalized random sampling design to obtain approximately the same number of pixels for each class. The target size of both the training and testing sets was initially set to 400 randomly selected pixels per class, the minimum number per class required was set to 20, e.g. when coarser pixels were selected. RF was trained and applied to the entire time series data at each spatial scale, and all classes present in the corresponding study sites were included in the legend. To enhance the reliability of the experiments the random draws of training and validation data were repeated 10 times, and the classification performance estimates (see next section) were averaged over the 10 independent model runs.

3.3 *Characterizing Crop Identification Performance*

Pixel size and pixel purity can be considered as two dimensions of a $v - \pi$ space. For each selected pixel population in this $v - \pi$ space,

information regarding the classification performance, e.g. overall accuracy, can be calculated. Similar to the method proposed by Löw & Duveiller (2014) variables describing crop classification performance are calculated for each pixel population:

3.3.1 Quantifying classification performance

A set of confusion matrices (Congalton 1991) was computed on the hard result of the test sets defined along the $\pi - v$ dimensions. The overall accuracy parameter (ACC) is defined as the total proportion of correctly classified test pixels per total number of test pixels:

$$ACC = \frac{n_c}{n} \tag{4}$$

where n is the number of test samples, and n_c the number of correctly allocated test samples. As class-wise accuracy metric the F_β-measure of van Rijsbergen (1979) was employed. This measure combines the precision pr_i (which gives the proportion of samples, which truly have class i among all samples that were classified as class i) and the recall tp_i (the TPR which gives the proportion of samples classified into class i among all samples which truly have class i). The former determines the error of omission (false exclusion), the latter the error of commission (false inclusion). The traditional F_β-measure equally weights precision and recall ($\beta = 1$) and is sometimes referred to as F_1 measure:

$$CA_i = (1+\beta^2)\frac{pr_i * tp_i}{\beta^2 * pr_i + tp_i} \tag{5}$$

Measures of classification uncertainty like entropy assess the spatial variation of the classification quality on a per-case, e.g. per-pixel, basis, and can be used to supplement the global summary provided by standard accuracy statements like overall accuracy (Foody 2002). It can be characterized as a quantitative measure of doubt when a final classification decision is made. Beneath the final ("hard") class label, non-parametric algorithms such as support vector machines or RF can generate for each classified case x (agricultural field or pixel) a "soft" output in form of a vector $p(x) = (p_1, ..., p_i, ..., p_n)$ that contains the probabilities that a pixel is classified into a class i, n being the total number of classes (Löw et al. 2013). Each of the elements in $p(x)$ can be interpreted as a degree of belief or posterior probability that a pixel actually belongs to i. From this vector, the α-quadratic entropy (Pal & Bezdek 1994) for a given pixel (x) can be calculated as a measure of uncertainty, which is defined as:

$$\overline{\mathrm{AQE}}(x) = \frac{1}{n * (2^{-2\propto})} * \sum_{i=1}^{n} p_i^{\propto}(1-p_i)^{\propto} \tag{6}$$

Where p_i is one element in $p(x)$, n the number of classes, and α an exponent that determines the behaviour of AQE(x). The entropy of the total classified pixel population can be quantified with the median of all classified pixels $\overline{\mathrm{AQE}}(x)$, denoted AQE. This can also be done at the per-class basis, by calculating the median entropy of all pixels classified into a class i, denoted AQE_i.

The number of available reference pixels N_i of a given class i represents the total available size of pixel populations in the $v - \pi$ dimensions that can be used for training and testing the classifier. In supervised crop classification a minimum number of pixels per crop class can be desirable to assure the generalizability of the classifier model to the unseen dataset, and to reduce the influence of (random) variability in the training data on the classification result.

3.3.2 Determining suitable pixel populations

The final step to determine the suitable pixel populations for crop classification is to isolate the (v, π) combinations for which the classification performance fulfils certain criteria. This is accomplished by defining acceptable thresholds for the variables defined above. Such thresholds will be used to define a frontier in this $v - \pi$ space dividing pixel populations that are above or below the acceptable threshold for a given surface. As an example, if an application requires a minimum class-wise accuracy of 80%, the surface CA_i is sliced by a plane passing by the value $CA_i = 0.80$ (see Fig. 3, left images). When the inter-

section of CA_i and the plane is projected onto the 2-D space $v - \pi$, it separates this domain into the region where selected pixel populations have classification accuracy higher than 75% and the region where the accuracy of the remaining population will be lower than 75% (Fig. 3, right image). By drawing limits on the different parameters, the parameter surfaces were sliced and the intersection points of these slices in $v - \pi$ space were used to identify the position of the coarsest acceptable pixel sizes (v_{max}) and the corresponding minimum required pixel purities π respectively (Fig. 3, right image). Accordingly, pixel population suitability is defined by the number of fulfilled criteria, e.g. highest suitability means that all criteria were fulfilled. In this study, thresholds were defined as follows: $ACC/CA_i > 0.75$, $AQE/AQE_i < 0.50$, and $N_i > 100$.

3.3.3 Selecting categorical scale

Three levels of aggregation were created by grouping or discarding certain crop classes, hereafter called level I, II, and III (Fig. 4). The rationale for defining the class legends in the aggregation levels was (i) to group crop classes with similar spectral and temporal NDVI

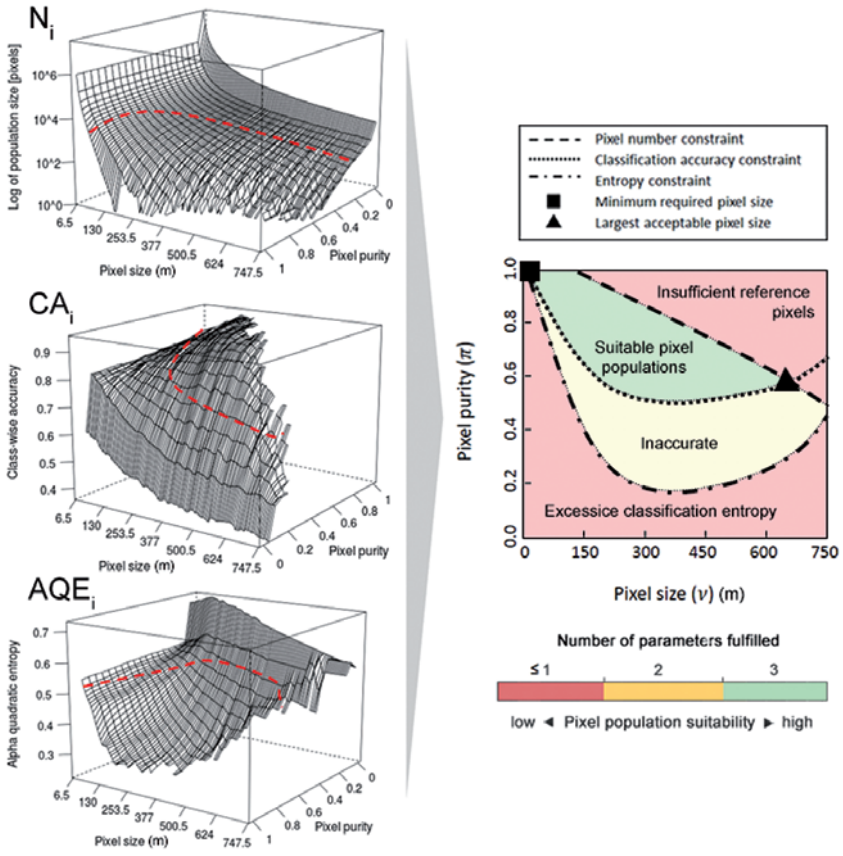

Fig. 3: Left column: Schematic examples of parameters chosen for crop identification for the pixel populations along the pixel size – pixel purity dimensions. Red dashed line indicates were predefined thresholds slice the parameter surfaces and separate $v - \pi$ space into two domains: one that fulfils a certain threshold and a second one that does not. Note that the pixel purity axis is inverted for N_i and AQE. Right column: Suitability map with theoretical boundaries in $v - \pi$ space used to define the requirements for pixel populations to be used for supervised classification. Circle indicates the position of maximum tolerable pixel size v_{max}, black filled square the minimum required pixel size v_{min}.

signatures and (ii) to discard classes that cover only a small fraction of the landscape (C_f < 0.01) and that are spectrally too distinct from other classes to be merged. Crop rotation classes in KHO ("Wheat-Sorghum / Maize" and "Wheat-rice") were merged in level II due to the similarity of the temporal NDVI profiles. Further, minor classes (C_f < 0.01) were merged to one class "mixed crops", due to their spectral similarity. Likewise, "Alfalfa 1y" and "Alfalfa 3y" were merged in level II in KYZ due to their spectral similarity, reducing the number of classes from five to three. Winter wheat was discarded in level II due to its marginal cover fraction in both sites (C_f < 0.01). Fallow fields and mixed crops in KHO, which together cover less than 2% of the landscape were completely removed from the class legend in level III, reducing the number of classes from eleven to six. In this level a binary class legend was established in KYZ, i.e. active, e.g. rice, vs. unused, e.g. fallow, alfalfa, fields. The pixel population suitability was then determined separately at each aggregation level, according to the methodology described in the previous section. The pixel population suitability was then determined separately at each aggregation level, according to the methodology described in the previous section.

4 Results and Discussion

As expected, the suitability of pixel populations for classifying crops varied in the $v - \pi$ space and the suitability was enhanced when selecting higher aggregation levels (Fig. 5) as was demonstrated in previous studies (e.g. Marceau et al. 1994b). Suitable pixel populations were restricted to rather small pixel sizes at level I, with v_{max} = 162.5 m in KYZ, similar to KHO (v_{max} = 149.5 m). In KYZ aggregating crop classes in level II resulted in enhancing the suitability of pixel populations in the $v - \pi$ space, in particular coarser pixels could be tolerated (v_{max} = 747.5 m at level III) and the minimum purity requirements could be relaxed for v_{max} (the corresponding π at level I was 0.60, and decreased to 0.45 for v_{max} at level III). Likewise, in KHO aggregating classes enhanced the suitability of pixel populations for crop identification, but compared with KYZ the use of coarser pixels was limited, most obvious because of the spatial pattern of fields in the KHO landscape, e.g. more crop classes in a more heterogeneous landscape where the use of coarser pixels resulted in a higher degree of pixel mixing, which resulted in having generally higher purity requirements than in KYZ. This could be explained by the limited availability of purer reference pixels in this landscape. Further, tolerating some signal contamination may be beneficial

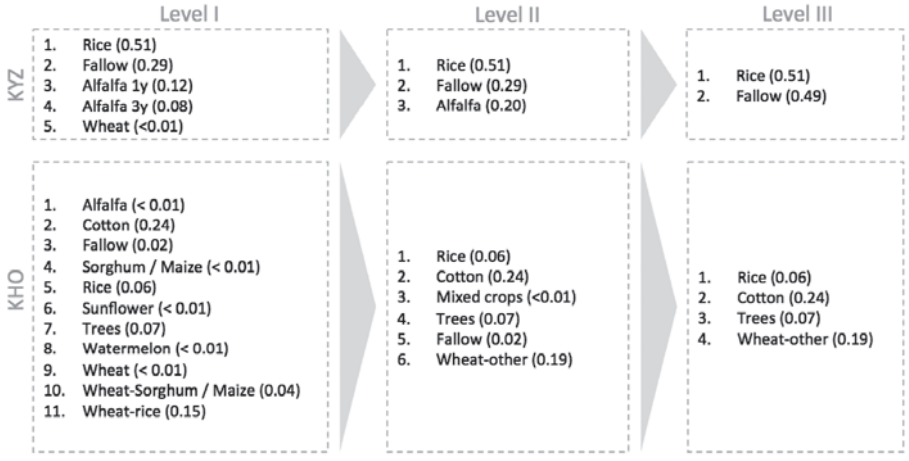

Fig. 4: Class legends according to three levels of aggregation in the two study sites. Cover fractions (C_f), i.e. the fraction of the sites covered by agricultural fields of a certain crop class, are given in brackets.

in the case of crop identification in KHO, e.g. a larger sample size for classification training including mixed pixels may better represent the diversity of the spectral response of the target class within this landscape (Foody 1996).

For specific classes the required conditions to achieve highest CA_i varied among the three aggregation levels (Fig. 6). The corresponding pixel sizes tended to become coarser when increasing the aggregation level. An explanation why coarser pixel sizes generally achieve higher accuracy could be the interplay of increasing error-rates of smaller but purer pixels, which become more abundant when pixels become smaller, caused by increasing within-class variability (Hsieh et al. 2001) and decreasing error of mixed pixels, which become less abundant when pixels become smaller. The within-class variability might in particular become an important issue when such heterogeneous crop classes like alfalfa and other fallow fields are merged, e.g. in KYZ. In such a situation it might be better to have coarser pixels (McCloy & Bøcher 2007), thereby reducing this variance and counterbalancing the effect of pure-pixel heterogeneity within smaller pixels. After merging quite diverse crop classes in KYZ in level III (two types of alfalfa fields and other fallow land to one class "fallow") the condition for best CA_i was pushed to 604.5 m, compared to 195.0 m at level I. In this context, image segmentation should be considered (Blaschke 2010, Yan & Roy 2014). Image segmentation of high spatial resolution images or time series results in image-objects that minimize the variance but that are not constrained by the rectangular nature of the pixels. Analysing the optimal size of multi-date image objects for crop identification could be an interesting extension of the proposed conceptual framework. Another advantage of object-based image analysis (OBIA) is that different segment sizes for specific land use types can be used and analyzed. Image-objects could also be analysed with respect to their homogeneity at different spatial scales using a concept analogous to pixel purity. However, such questions are beyond the scope of this current paper.

For fallow fields in KYZ the pixel sizes for which maximum CA_i was archived were in the same order at level I and II (195.0 m and 208.0 m), but coarser pixel sizes were required at level III (604.5 m), which could be attributed to the spatial aggregation pattern of fields

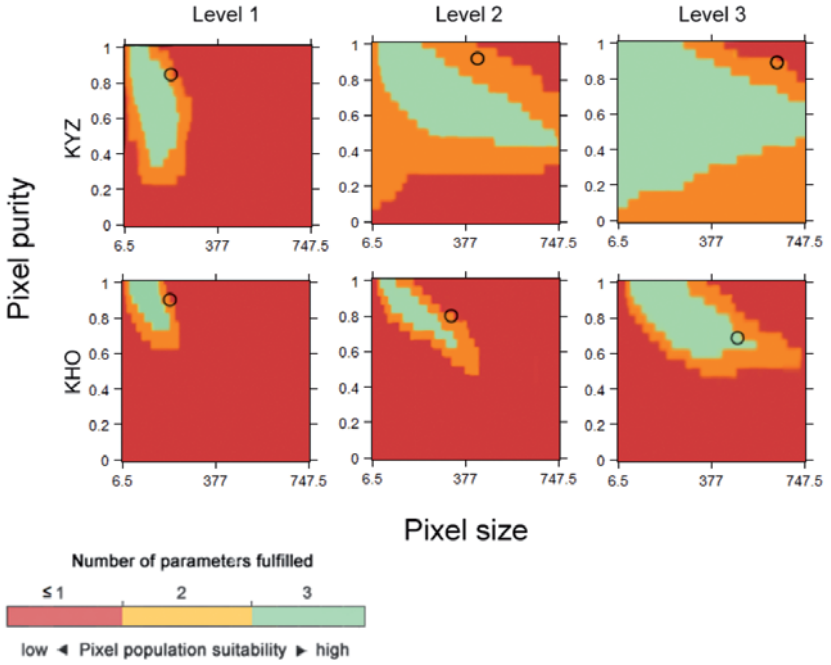

Fig. 5: Suitability maps for three different class aggregation levels for all classes. Circles indicate position of maximum achievable ACC in $v - \pi$ space.

in this landscape, i.e. large blocks of fields with the same crop class "fallow" in level III. In KHO pixel populations suitable for classifying rice and fallow fields were characterized by higher pixel purity requirements than in KYZ. This can be explained by the spatial pattern or field fields which are more spatially dispersed than in KYZ (Fig. 1), resulting in mixed signal once the purity of the (coarser) pixels becomes too low, e.g. $\pi < 0.7$. Likewise, the maximum possible CA_i for rice fields in KHO was achieved with smaller pixels than in KYZ.

The high ACC in KYZ when selecting level II or III (Fig. 7) offers positive prospects for using images from existing satellite missions (Landsat 30 m, MODIS 250 m / 500 m, NPP-VIIRS 747.5 m) used for crop mapping. Yet, results also highlight the need to consider that the class legend must be selected properly and separately adapted in different agricultural landscapes. The lowest ACC and CA_i of rice

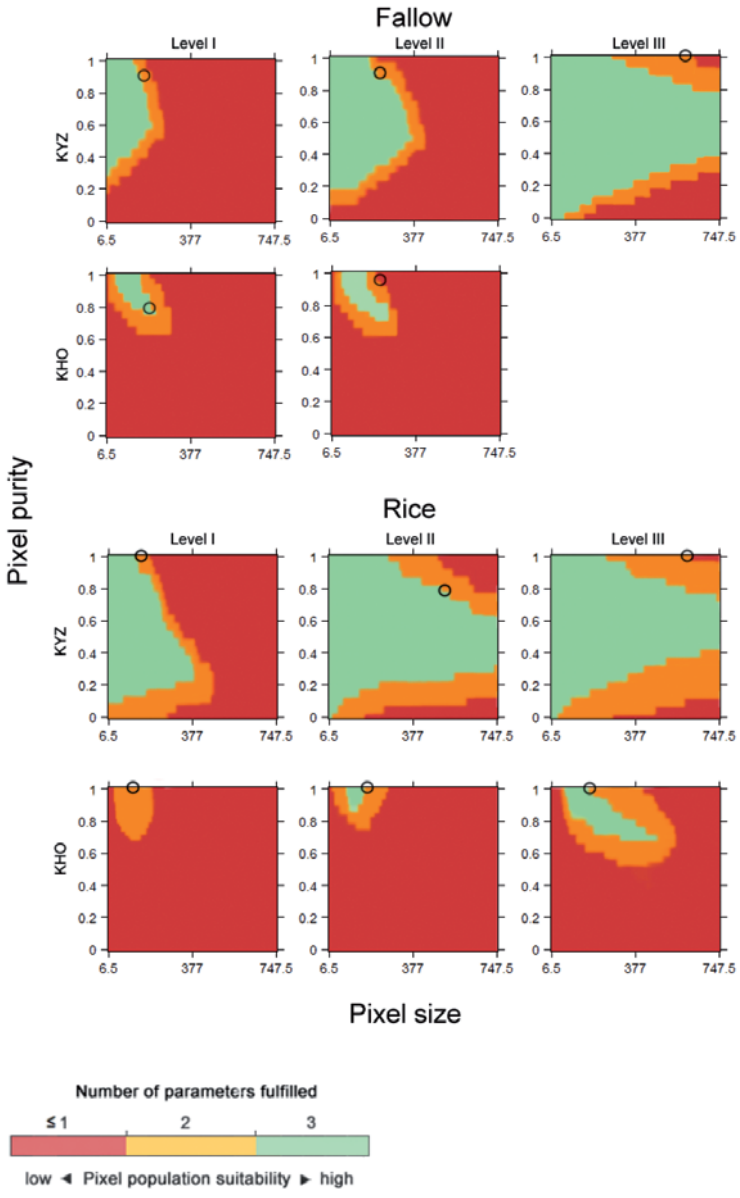

Fig. 6: Suitability maps for three different class aggregation levels and for class fallow (top rows) and fallow (bottom rows). Ovals indicate position of maximum achievable CA_i in $\nu - \pi$ space.

and fallow fields were achieved when selecting coarser pixels (745.5 m) at level I. The smaller the pixel sizes the higher was ACC at this level. Further, the higher the aggregation level the smaller was the absolute differences between ACC, e.g. at 0.043 at level III but 0.791 and 0.103 in level I and II, respectively. CA_i of fallow fields in KYZ increased when shifting from level II to III, whilst the difference in CA_i for rice was within 0.01, i.e. for 32.5 m and 247.5 m. In KHO using coarser pixels (247.5 m and 747.5 m) resulted in a clear drop in CA_i for rice fields, for which smaller pixels gave better results due to the spatial pattern of fields (see above).

Overall, the results indicate that there was no unique spatial resolution for identifying and discriminating all classes at once at a given aggregation level, confirming previous studies (Marceau et al. 1994b, Löw & Duveiller 2014). Within a particular aggregation level, some classes are better classified at fine spatial resolutions, while others require coarser spatial resolutions. Further, the suitability of pixel populations for identifying specific crops differed within the landscapes, and for a given crop there were large differences among the landscapes. Of course, the results are only valid within the parameterization chosen for this study, and the user might select other metrics more appropriate to the targeted application which is not limited to crop discrimination. The parameters in this study were purposefully selected because different metrics evaluate different components of accuracy as they are based on different statistical assumptions on the input data. Consequently, seeking to optimize classifier algorithm performance or defining suitable pixel sizes with only one metric may have led to a non-optimal result when viewed from another point of view or quantified with a different metric that is sensitive to different features concerning accuracy (Foody 2002, Provost & Fawcett 1997).

Landscape heterogeneity, e.g. the size of agricultural fields and the properties of their neighbourhood, were shown to be important factors determining classification accuracy. When the crops were grown on larger fields, or when the cover fraction was high, coarser pixel sizes could be tolerated for crop identification. Crops grown on fields dispersed over

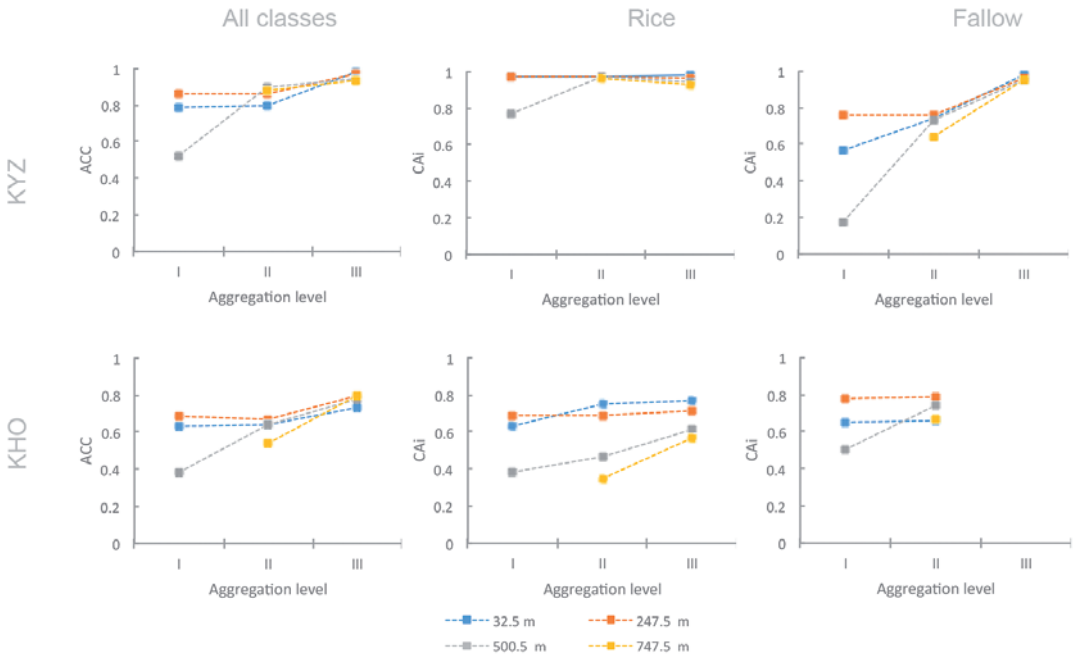

Fig. 7: Maximum achievable overall and class-wise accuracies (ACC and CA_i) for selected pixel sizes at different aggregation levels. Note that in KHO the class "fallow" was omitted in aggregation level III. At aggregation level I the number of reference pixels in KHO and KYZ dropped below 20 for at least one class at 747.5 m ($N_i < 20$), which forced the experiments to stop.

the landscape like rice in KHO could only be detected using smaller pixel sizes, and only using relatively pure pixels. However, the crop classes displayed differences in the specific nature of these relationships, and the landscape heterogeneity with respect to the spatial pattern also influenced the choice of pixel sizes. For instance, while the median field sizes in KYZ and KHO are comparable, the farmer's fields are more regular in shape, less variable in size, and the same crops are found on blocks of fields that together can aggregate to more than 100 ha in size. Due to this spatial aggregation pattern, it is easier to have coarser pixels fall within target fields and thus conferring higher acceptable pixel sizes for crop identification, resulting in notably higher values for v_{max} in KYZ than in KHO.

The results confirm previous studies that found large differences in accuracy depending on the degree of pixel mixing, e.g. Foody (1996). Therefore, this study suggests for a more spatially explicit assessment of accuracy. The framework could be used to plot the suitability (or accuracy) of each pixel covering arable land as a function of its purity. This is similar to spatial assessments of classification uncertainty (Löw et al. 2013) and could be of interest when coarser satellite sensors like MODIS or Sentinel-3 are to be used for crop mapping. For instance, one practical utility of this framework could be "masking out" unsuitable pixel populations, according to the user's specific needs, before applying them in agricultural crop-specific growth modelling. Further, knowledge on the spatial distribution of map quality, e.g. defined as pixel suitability, allows for a better interpretation of the results of agricultural model outputs.

5 Conclusions

The overall methodology presented in this study was used to assess the impact of categorical and spatial scale (pixel size) on crop classification accuracy. Coarser satellite images were simulated, based on RapidEye data, and classified using the RF algorithm. Different class legends (aggregation levels) were tested, which were created based on merging spectrally similar classes or by discarding classes that only covered small fractions of the landscapes. The results show that there was no unique spatial resolution that provided the best classification result for all classes at once at a given aggregation level. Classification accuracy could be improved by aggregating certain crop classes. Further, the suitability of pixel populations for crop discrimination differed within the landscapes, and for a given crop there were differences among the landscapes. The results imply that classifications based on purer pixels were generally the most suitable (and most accurate) for crop type discrimination, but the number of such pure pixels might be limited in heterogeneous landscapes, where only a few pixels fall into larger fields. Although crops within mixed pixels could be more accurately distinguished when aggregating crop classes, a meaningful evaluation of classification accuracy still could only be achieved when accommodating the effect of pixel purity.

The results of this study suggest that it is important to consider the field size distribution and pattern when shifting between regions, and not every sensor might be equally suitable for a given application like crop mapping in a large region with different spatial pattern like in Central Asia or other regions worldwide. Neglecting the effect of pixel purity and aggregation level might produce haphazard results, which could negatively impact spatial modelling when crop maps are taken as input. In the context of agricultural crop growth monitoring the framework described above can be used to draw guidelines for selecting appropriate imagery, e.g. suitable pixel sizes, and for selecting appropriate class legends for accurate crop identification and crop type discrimination over a given agricultural landscape when the interest is only on a subset of the landscape, e.g. pixels covering arable land. In the context of the CAWa-project this framework is recently being implemented to define pixel size requirements and appropriate class legends for crop identification in the irrigated landscapes in Fergana Valley and Karakalpakstan (Uzbekistan). This is of relevance because agricultural production monitoring (yield, evapotranspiration) in this project is based on MODIS data, which delivers the required swath and high revisit frequen-

cy. Due to the need for crop specific masks at the MODIS scale, knowledge about the constraints of such coarse image data for crop identification is essential. The results of this study provide an opportunity to discuss the effects of pixel size and purity and the classification algorithm independent factors such as parcel size, spatial distribution of crop types and crop patterns on agricultural monitoring related applications. In a world with increasingly diverse geospatial data sources in terms of combinations of spatial and temporal resolutions, the tool can also help users to choose the different data sources that meet the requirements imposed by their applications.

Acknowledgements

This study was undertaken at the Department of Remote Sensing (University of Würzburg) within the CAWa project funded by the German Federal Foreign Office, and within the German-Uzbek Khorezm project. We thank the German Aerospace Center (DLR) for providing data from the RapidEye Science Archive (RESA). The German National Academic Foundation (Studienstiftung des deutschen Volkes) funded this research by way of a PhD grant to the first author. The authors also acknowledge the support of the Deutsche Gesellschaft für Internationale Zusammenarbeit (GIZ) during the field studies in Uzbekistan and Kazakhstan.

References

Aplin, P., 2006: On scales and dynamics in observing the environment. – International Journal of Remote Sensing **27** (11): 2123–2140.

Atkinson, P.M. & Aplin, P., 2004: Spatial variation in land cover and choice of spatial resolution for remote sensing. – International Journal of Remote Sensing **25** (18): 3687–3702.

Blaschke, T., 2010: Object based image analysis for remote sensing. – ISPRS Journal of Photogrammetry and Remote Sensing **65** (1): 2–16.

Breiman, L., 2001: Random forests. – Machine Learning **45** (1): 5–32.

Congalton, R.G., 1991: A review of assessing the accuracy of classifications of remotely sensed data. – Remote Sensing of Environment **37** (1): 35–46.

Cushnie, J.L., 1987: The interactive effect of spatial resolution and degree of internal variability within land-cover types on classification accuracies. – International Journal of Remote Sensing **8** (1): 15–29.

Duveiller, G. & Defourny, P., 2010: A conceptual framework to define the spatial resolution requirements for agricultural monitoring using remote sensing. – Remote Sensing of Environment **114** (11): 2637–2650.

Foody, G.M., 1996: Incorporating mixed pixels in the training, allocation and testing stages of supervised classifications. – Pattern Recognition Letters **17** (13): 1389–1398.

Foody, G.M., 2002: Status of land cover classification accuracy assessment. – Remote Sensing of Environment **80** (1): 185–201.

Hsieh, P., Lee, L.C. & Chen, N., 2001: Effect of spatial resolution on classification errors of pure and mixed pixels in remote sensing. – IEEE Transactions on Geoscience and Remote Sensing **39** (12): 2657–2663.

Ju, J., Gopal, S. & Kolaczyk, E.D., 2005: On the choice of spatial and categorical scale in remote sensing land cover classification. – Remote Sensing of Environment **96** (1): 62–77.

Levin, S.A., 1992: The problem of pattern and scale in ecology. – Ecology **73** (6): 1943–1967.

Liaw, A. & Wiener, M., 2002: Classification and Regression by randomForest. – R News **2** (3): 18–22

Löw, F., Schorcht, G., Michel, U., Dech, S. & Conrad, C., 2012: Per-field crop classification in irrigated agricultural regions in Middle Asia using random forest and support vector machine ensemble. – Proceedings of SPIE 8538, Edinburgh, United Kingdom.

Löw, F. & Duveiller, G., 2014: Defining the spatial resolution requirements for crop identification using optical remote sensing. – Remote Sensing **6** (9): 9034–9063.

Löw, F., Michel, U., Dech, S. & Conrad, C., 2013: Impact of feature selection on the accuracy and spatial uncertainty of per-field crop classification using Support Vector Machines. – ISPRS Journal of Photogrammetry and Remote Sensing **85:** 102–119.

Marceau, D.J., Howarth, P.J. & Gratton, D.J., 1994a: Remote sensing and the measurement of geographical entities in a forested environment. 1: The scale and spatial aggregation problem. – Remote Sensing of Environment **49** (2): 93–104.

Marceau, D.J., Gratton, D., Fournier, R. & Fortin, J., 1994b: Remote sensing and the measurement of geographical entities in a forested environment. 2. – The optimal spatial resolution. Remote Sensing of Environment **49** (2): 105–117.

McCloy, K. & Bøcher, P., 2007: Optimizing image resolution to maximize the accuracy of hard classification. – Photogrammetric Engineering and Remote Sensing **73** (8): 893–903.

Pal, N.R. & Bezdek, J.C., 1994: Measuring fuzzy uncertainty. – IEEE Transactions on Fuzzy Systems **2** (2): 107–118.

Provost, F. & Fawcett, T., 1997: Analysis and visualization of classifier performance: Comparison under imprecise class and cost distributions. – Third international conference on knowledge discovery and data mining. – AAAI Press, Menlo Park, CA, USA.

Richter, R., 2011: Atmospheric/Topographic Correction for Satellite Imagery. – ATCOR-2/3 User Guide 7.1.

Smith, J.H., Stehman, S.V., Wickham, J.D. & Yang, L., 2003: Effects of landscape characteristics on land-cover class accuracy. – Remote Sensing of Environment **84** (3): 342–349.

van Rijsbergen, C.J., 1979: Information Retrieval, 2nd ed., Butterworths. – Butterworth & Co Publishers Ltd., United Kingdom.

Woodcock, C.E. & Strahler, A.H., 1987: The factor of scale in remote sensing. – Remote Sensing of Environment **21** (3): 311–332.

Yan, L. & Roy, D.P., 2014: Automated crop field extraction from multi-temporal Web Enabled Landsat Data. – Remote Sensing of Environment **144:** 42–64.

Addresses of the Authors

Dipl. Geogr. Fabian Löw & Prof. Dr. Christopher Conrad, Department of Remote Sensing, University of Würzburg, Oßwald-Külpe-Weg 86, D-97074 Würzburg, e-mail: fabian.loew@uni-wuerzburg.de

Dr. Grégory Duveiller, European Commission Joint Research Centre (JRC), Via E. Fermi, 2749, I-21027 Ispra (VA), Italy

Prof. Dr. Ulrich Michel, Department of Geography, University of Education, Czernyring 22/11-12, D-69115 Heidelberg

Manuskript eingereicht: Juni 2014
Angenommen: September 2014

PFG 1/2015, 0021 – 0032
Stuttgart, February 2015

Article

Identification of Agricultural Crop Types in Northern Israel using Multitemporal RapidEye Data

Florian Beyer, Thomas Jarmer & Bastian Siegmann, Osnabrück

Keywords: LU/LC, multitemporal classification, phenology, crops, RapidEye

Summary: Accurate land use / land cover classification (LU/LC) of agricultural crops still represents a major challenge for multispectral remote sensing. In order to obtain reliable classification accuracies on the basis of multispectral satellite data, merging crop classes in rather broad classes is often necessary. With regard to the rising availability and the improving spatial resolution of satellite data, multitemporal analyses become increasingly important for remote sensing investigations. For the separation of spectrally similar crops, multidate satellite images include different growth characteristics during the phenological period. The present study aims at investigating a way to perform highly accurate classifications with numerous agricultural classes using multitemporal RapidEye data. The Jeffries-Matusita separability (JM) was used for applying a pre-procedure in order to find the best multitemporal setting of all available images within one crop cycle, consisting of two cultivation periods P1 with 16 agricultural classes and P2 with 27 agricultural classes. Only one critical class pairing occurred for both P1 and P2 taking into account the best multitemporal dataset. The maximum likelihood (ML) classifier and the support vector machine (SVM) were compared using the most suitable multitemporal images. Both algorithms achieved very high overall accuracies (OAA) of over 90%. SVM was slightly better with a classification accuracy of P1-OAA = 96.13% and P2-OAA = 94.01%. ML provided a result of OAA = 94.83% correctly classified pixels for P1 and OAA = 93.28% for P2. The processing time of ML, however, was significantly shorter compared to SVM, in fact by a factor of five.

Zusammenfassung: *Identifikation landwirtschaftlicher Kulturen in Nordisrael mittels multitemporaler RapidEye-Daten*. Eine hochgenaue Landnutzungsklassifizierung (LU/LC) landwirtschaftlicher Kulturen auf Basis von multispektralen Fernerkundungsdaten stellt noch immer eine große Herausforderung dar. Oftmals müssen unterschiedliche landwirtschaftliche Kulturen zu Oberklassen zusammengefasst werden, damit die Klassifizierung auf Grundlage multispektraler Satellitendaten akzeptable Genauigkeiten erreichen. Mit der steigenden Verfügbarkeit und gleichzeitig verbesserten räumlichen Auflösung von Satellitendaten kommt der multitemporalen Analyse von Fernerkundungsdaten immer mehr Bedeutung zu. Dabei wird der Sachverhalt genutzt, dass verschiedene Pflanzen einen unterschiedlichen phänologischen Verlauf besitzen. Ziel der vorliegenden Studie ist eine hochgenaue Klassifizierung landwirtschaftlicher Flächen mit hoher Klassenanzahl durch die multitemporale Analyse multispektraler RapidEye-Daten. Das Trennbarkeitsmaß Jeffries-Matusita Separability (JM) wurde als Vorverarbeitungsschritt verwendet, um den besten multitemporalen Datensatz aus den verfügbaren einzelnen Aufnahmeterminen eines kompletten Fruchtwechsels, bestehend aus zwei Anbauperioden P1 mit 16 und P2 mit 27 landwirtschaftlichen Klassen, zu finden. Die spektrale Trennbarkeit der vorhandenen Klassen ergab für den ermittelten multitemporalen Datensatz für P1 und P2 nur eine kritische Klassenpaarung. Für die Klassifizierung wurden die Klassifizierungsalgorithmen Maximum Likelihood (ML) und Support Vector Machine (SVM) vergleichend gegenübergestellt. Beide Algorithmen lieferten Gesamtklassifizierungsgenauigkeiten von über 90%. Die SVM erwies sich dabei mit Klassifizierungsgenauigkeiten OAA = 96,13% für P1 und OAA = 94,01% für P2 zwar als geringfügig genauer, jedoch war die ML-Klassifizierung (P1-OAA = 94,83%; P2-OAA = 93,28%) deutlich, d.h. um den Faktor 5, schneller.

www.schweizerbart.de
DOI: 10.1127/pfg/2015/0249
1432-8364/14/0249 $ 3.00

1 Introduction

Information on land use / land cover (LU/LC) forms a crucial data basis in numerous applications for planning, resources management, and identification of environmental changes or ecological forecasting (Khan et al. 2012). Crop identification and monitoring belong to this category (Vicente-Guijalba et al. 2014, Guerschman et al. 2003, Brisco & Brown 1995). Thematic maps of crop types at agricultural field level can provide important information, e.g. to support agricultural policies, to verify the farmers' applications for public subsidies, or assist in the practice of precision agriculture (Alganci et al. 2013). Accurate and up-to-date maps also may form the basis for yield estimates or environmental and land use planning at local, regional, and national levels. Large area mapping of LU/LC from terrestrial survey is, however, very expensive as well as time-intensive. Hence, LU/LC derived from remote sensing data is of utmost importance. Cropland classification is still a major challenge, considering issues like data availability, classification accuracy, operational processing or acquisition costs (Mulla 2013, Lu & Weng 2007). Advantages of satellite images include large area coverage, mainly operational processing and availability of low cost data (Araújo et al. 2011). As a consequence, a multitude of studies on crop type identification using multispectral data have been performed in the past decades (e.g. Mariotto et al. 2013, Cruz-Ramírez et al. 2012, Mathur & Foody 2008, Brisco & Brown 1995, Buechel et al. 1989, Bauer & Cipra 1973). The main problem for detecting crop types using one single multispectral dataset has been the discrimination uncertainty which is caused by variations of many factors, e.g. different phenological stages or varying fractional vegetation cover, shapes and textures (Alganci et al. 2013, Liu et al. 2002). Different vegetation types frequently show very similar spectral behaviour and inner-field spectral variations are often higher than observed between different crop types (Thenkabail et al. 2011, Guerschman et al. 2003). Therefore, most studies used only a few classes or merged crops classes in broader categories (e.g. Guerschman et al. 2003, Brisco & Brown 1995). In order to handle the above-mentioned challenging tasks in LU/LC classifications, phenological information has been investigated by the remote sensing community as an additional dimension in crop identification. As a consequence, numerous studies combined several multispectral Landsat (Wondrade et al. 2014, Demir et al. 2013, Oetter et al. 2001, Lunetta & Balogh 1999) or SPOT datasets (Chust et al. 2004, Murakami et al. 2001) from one growing period and treated them as one single multitemporal scene. Furthermore, the synergism of SAR and multispectral optical satellite data has been evaluated (Vicente-Guijalba et al. 2014, Askne et al. 2013, Waske & van der Linden 2008, Huang et al. 2007, Brisco & Brown 1995). Oetter et al. (2001), for instance, obtained classification accuracies close to 90%, using five Landsat-5 TM images within one year. The considered classes included agricultural crops, orchards, forest and natural cover types as well as urban areas. The subclasses of agriculture finally classified in this study were aggregated to five broader classes instead of the 15 original mapped agricultural categories.

An additional objective in LU/LC classification from remote sensing data is the selection of appropriate classification algorithms. Waske & van der Linden (2008) emphasized the shift from statistical approaches to more powerful and flexible machine learning algorithms for data classification as a recent development in remote sensing. In the past few years many authors compared newly developed and widely established classifiers (Alganci et al. 2013, Mountrakis et al. 2011, Mathur & Foody 2008, Huang et al. 2002 & 2007). However, recent developments of classification algorithms are also associated with an increasing need of computational performance. Considering this assumption, the non-parametric classifier support vector machine (SVM) and the well-known parametric maximum likelihood (ML) classifier were selected and compared regarding the obtained LU/LC classification with respect to overall classification accuracy (OAA) and performance.

Most multitemporal studies classified all possible dataset combinations in order to find the best multitemporal setting/stack. Considering the enormous computational costs

of classifying large-area datasets with many classes and complex algorithms such as SVM, there is a need to perform a pre-classification approach/procedure to accelerate this selection process.

Given the above described background, the major goals of this study were:

1) to investigate the potential of multitemporal RapidEye data for large-scale identification of crops with particular emphasis on accurate spectral separability of numerous different crop types and agricultural classes and
2) to perform a pre-classification procedure in order to find the best multitemporal data setting avoiding long processing times.

2 Study Site and Data

2.1 *Study Site*

The study site (32.5° N, 35.0° E / 32.9° N, 35.3° E) is located in northern Israel and extends from the bay of Haifa to the plain of Jesreel covering an area of 2,500 km^2. The region between Haifa, Nazareth and the Sea of Galilee is one of the main agricultural production areas in Israel. The region is characterized by Mediterranean climate with hot and dry summers as well as rainy cool winters (Singer 2007). Rainfall is limited from September to May with a mean annual precipitation of 539 mm (IMS 2014). Natural conditions in the investigated area allow crop cultivation during two cultivation periods within one year. The first cultivation period (P1) considered for this research lasted from October 2012 to late March 2013. After the crops were harvested, the second cultivation period (P2) started in April and ended in August 2013. During the dry and hot months in summer (May to August) irrigation is quite common.

2.2 *Mapping Land Use / Land Cover*

For each cultivation period a field campaign was conducted. During the first field campaign in March 2013 crops of P1 for 425 agricultural fields were mapped. P1 was characterized by the pluvial period and moderate temperatures during the winter season. Dominant classes were grains (rye and oat) and chickpeas. Smaller fields were mainly cultivated with peas, tomato, different types of cabbage and salads. In total 16 different classes were identified. During the second field survey, crops of P2 were mapped in June 2013 (in total 826 fields). The beginning of P2 coincided with the end of the rainy season. Arid conditions increased during this period from April to August (IMS 2014). As a consequence, farmers have to store and provide water for irrigation. During this cultivation period cotton, watermelon, maize and sorghum were the dominant crops. Compared to P1 much more diverse crop plants were cultivated in P2, such as beetroot, leek, zucchini, pumpkin, muskmelon or different sorts of cabbages and salads. Additionally, non-cultivated fields like fallow, green fallow and grain residues were also considered. Altogether 27 different classes were mapped. After the end of August the weather conditions were not suitable for cultivation any longer except for fruit trees, e.g. avocados, oranges, peaches, or olives.

2.3 *Satellite Data*

The acquisition of RapidEye data was enabled within the RESA project (RESA 597). The data was provided in preprocessing level 3A. Level 3A data include orthorectification with radiometric, geometric and terrain correction (Weichelt et al. 2013). Subsequently, atmospheric correction was conducted with the generic processing chain CATENA developed at DLR (Krauss et al. 2013). Two individual image datasets were available for each cultivation phase (P1: Jan13, Mar13, P2: Jun13, Aug13, Tab. 1). Furthermore, two additional datasets were acquired in October 2012 and April 2013. The October dataset represented the end of the prior arid non-agricultural period and at the same time the beginning of the ongoing first cultivation phase P1. April is the transition period between P1 and P2. Each dataset was a mosaic from two RapidEye tiles (in total 1,000 km^2 per mosaic).

Tab. 1: Datasets used for separability testing.

Cultivation period	Stack names	Acquisition months	Number of datasets (bands)
P1	Oct12	Oct 2012	1 (5)
	Jan13	Jan 2013	1 (5)
	Mar13	Mar 2013	1 (5)
	P1-stack-1	Jan + Mar 2013	2 (10)
	P1-stack-2	Oct 2012 + Jan + Mar 2013	3 (15)
P2	Jun13	Jun 2013	1 (5)
	Aug13	Aug 2013	1 (5)
	P2-stack-1	Jun + Aug 2013	2 (10)
	P2-stack-2	Oct 2012 + Jun + Aug 2013	3 (15)
	P2-stack-3	Oct 2012 + Apr + Jun + Aug 2013	4 (20)

3 Methods

Four agricultural areas representing different natural settings (coastal plain, hilly terrain) in rural and sub-urban environment were selected for mapping. These areas included large scale agriculture as well as small fields with very heterogeneous crop types. A GIS vector layer was created to extract mapped agricultural fields from satellite images. All individual fields were buffered to mask boundary pixels which might represent mixed land use and hence, should be excluded from further processing. The fields mapped during both campaigns (P1 and P2) were divided into a training and a validation dataset. Fields representing in the mean about 25% of the sampled area were used for independent validation. However, depending on availability, the size of the area considered for validation varied by class (about 16% of the area in the minimum (P1: chickpea; P2: leek) and 41% in the maximum (P1: cabbage; P2: zucchini)).

A pre-classification procedure was applied to the mono- and multitemporal RapidEye data to prove which dataset provided the best class separability. In this context, Jeffries-Matusita separability (JM) was calculated for each class pair of P1 and P2. JM is based on a distance calculation between a pair of probability distributions (Thomas et al. 1987). The considered classes had to be normal distributed and hence, small classes such as napa cabbage should be interpreted carefully. Regarding two classes, JM shows a saturating behaviour asymptotically to 2.0, with 0 implying complete similarity and 2 indicating complete separability.

In order to compare each class with each other, the number of possible parings N can be calculated as

$$N = \binom{n}{2} = \frac{n!}{2!(n-2)!} \quad (1)$$

where n is the number of classes.

A well-established operationally-used algorithm ML and a modern machine-learning algorithm SVM were compared regarding their accuracy and performance classifying the crop types. ML and SVM were applied to the datasets which provided best separability results in separability analysis. ML is the most commonly classifier in practice, because of its robustness (Khan et al. 2012, Hall et al. 1995), but often produces 'noisy' results for complex landscapes (Lu & Weng 2007). SVMs are based on statistical learning theory that optimizes separating boundaries between two classes (Sesnie et al. 2010, Vapnik 1999) without requirements such as normal distribution. In the presented study, a radial basis function (with $\gamma = 0.067$ and $C = 100.00$) was selected for SVM parameterization.

In order to assess the performance of both classifiers OAA was calculated. Furthermore, the kappa coefficient κ was determined. κ ranges between 0 and 1, whereas 1 indicates 100% pixels correctly classified.

4 Results and Discussion

4.1 *Spectral Separability*

First, spectral separability was investigated on the basis of the mono- and multitemporal datasets for all classes from P1 and P2. According to (1) there are 120 pairings in P1 and 351 pairings in P2. Pairings are considered to be critical if the JM value was less than 1.9 (Richards 2005). Tab. 2 illustrates the improvement of class separability with increasing temporal and hence, spectral dimension.

The dataset from October 2012 (Oct12) provided the worst separability for P1 with 90 critical pairings of 120 pairings in total. Agricultural fields were fallow at this time, crops mainly not germinated and discrimination between the different land use types, except for different orchard species, was impossible. The second dataset Jan13 represented the mid-position of the phenological development of P1. Many crops were well developed while others were still in early growth stages. Due to the very similar spectral behaviour, the differentiation of several crops was not possible. Hence, 61 of 120 class pairings received JM values below 1.9 indicating limited separability. The third single date was from March 2013 (Mar13) when the mapping campaign was conducted. At this time root crops were already mature and grain crops were at the phenological stage of ears emergence. It was expected that this stage is most appropriate for crop differentiation. Results of the separability analysis confirmed this assumption but the results still show 41 critical pairings (Tab. 2). Tab. 3 (upper part) illustrates the ten worst parings for P1. Considering the spatial resolution of RapidEye with one pixel covering an area of 25 m^2, most of these not clearly separable classes showed a mixed signal of soil and vegetation, which is especially true for green fallow, onions, orchards, fennel and leek. These crops reach their maximum coverage at various times. Therefore, separability of these classes was not satisfying. Obviously separating the different crops just by use of monotemporal multispectral RapidEye image is hardly possible.

As a next step, multitemporal datasets were tested for P1 regarding their feasibility to separate LU/LC classes. Multi-temporal datasets allow considering different growth stages of crops and additional spectral information for class separation. Stacking of two datasets (P1-stack-1: Jan13 and Mar13) including 10 spectral bands already had a tremendous effect on the improvement of spectral separability (Tab. 2) reducing the number of critical pairings to ten. Only the worst pairing (onions and green fallow) showed a JM value of less than 1.7 (1.57, see Tab. 3). The increasing spectral information representing additional temporal information was the essential factor for the improvement.

Tab. 2: Spectral separability of training data for both cultivation period P1 (above), 16 classes, 120 pairings and P2 (below), 27 classes, 351 pairings.

Cultivation period	Stacks	Number datasets	Number classes	Number critical Pairs	Worst pairing (JM)
P1	Oct12	1	16	90	0.3
	Jan13	1	16	61	0.55
	Mar13	1	16	41	0.61
	P1-stack-1	2	16	10	1.57
	P1-stack-2	3	16	1	1.89
P2	Jun13	1	27	126	0.71
	Aug13	1	27	176	0.69
	P2-stack-1	2	27	26	0.51
	P2-stack-2	3	27	9	1.77
	P2-stack-3	4	27	1	1.89

Further on, the Oct12 RapidEye image was included which provided additional spectral information of soils and fallows. Due to strip farming or coarse seeding of many crops, the spectral reflectance was characterized by mixed pixels containing information of soil and plant spectral reflectance, even during the flowering. P1-stack-2 had 15 spectral bands and combined the spectral information of soils from Oct12 with the spectral information of developed plants from Jan13 and Mar13. The additional information on soil reflectance – not included in P1-stack-1 – improved the separability substantially. Only one critical pairing (onions and green fallow, JM = 1.884) remained with a JM value close to 1.9. The typical spectral reflectance of both classes was made up by mixed pixels containing a high portion of soil reflectance due to the onions planted in lines leaving uncovered soil in between on one hand and the successional character of green fallow resulting in a very heterogeneous soil-influenced spectral behaviour on the other hand. Tab. 3 illustrates the improvement of separability with stacking additional datasets but it is clearly visible, that only the soil information yielded JM-values over 1.9, except for onions and green fallow.

Monotemporal datasets separability analysis for P2 (Tab. 2) provided more critical pairings compared to P1. The main reason was the much higher number of classes during this cultivation period. The monotemporal dataset Jun13 represented the month in which the

Tab. 3: The ten worst parings with JM values (bad separability < 1.8 (red); 1.8 – 1.9 moderate separability (yellow); good separability > 1.9 (green), 2 complete separability) for all mono- and multitemporal datasets in P1 and P2.

		Critical pairings		Oct12	Jan13	Mar13	P1-stack-1	P1-stack-2
P1	1	Green fallow	Onion	0.304	0.551	0.614	1.575	1.887
	2	Green fallow	Chickpeas	0.546	0.634	0.775	1.789	1.935
	3	Green fallow	Orchard	0.547	0.661	1.107	1.813	1.943
	4	Chickpeas	Orchard	0.604	0.831	1.125	1.848	1.948
	5	Peas	Pastureland	0.636	0.833	1.187	1.859	1.960
	6	Chickpeas	Onion	0.684	0.867	1.198	1.860	1.969
	7	Peas	Green fallow	0.699	1.049	1.281	1.880	1.972
	8	Grain	Millet	0.715	1.074	1.338	1.890	1.974
	9	Leek	Onion	0.734	1.177	1.375	1.890	1.977
	10	Fennel	Orchard	0.738	1.229	1.474	1.894	1.982
				Jun13	Aug13	P2-stack-1	P2-stack-2	P2-stack-3
P2	1	Green fallow	Grain residues	0.705	0.690	1.514	1.773	1.890
	2	Green fallow	Orchard	0.792	0.708	1.552	1.812	1.928
	3	Pumpkin	Watermelon	0.801	0.708	1.664	1.838	1.949
	4	Fallow	Grain residues	0.883	0.748	1.700	1.844	1.951
	5	Muskmelon	Watermelon	0.925	0.791	1.709	1.847	1.975
	6	Muskmelon	Pumpkin	1.007	0.858	1.715	1.868	1.978
	7	Maize	Sorghum	1.020	0.862	1.724	1.873	1.979
	8	Muskmelon	Onion	1.115	0.868	1.725	1.875	1.982
	9	Onion	Pumpkin	1.139	0.914	1.729	1.888	1.988
	10	Tomato	Watermelon	1.142	0.968	1.732	1.919	1.989

mapping campaign was conducted. The beginning of June was very appropriate for mapping because root crops were almost mature and easy to distinguish. The number of critical pairings in Jun13 (126) was lower than for Aug13 (176). In Aug13 the crops were mostly harvested, except late crops like maize, sorghum, and cotton.

Tab. 2 indicates a substantial improvement for P2-stack-1 (June and August 2013) in comparison to monotemporal analysis. From more than 100 critical pairings for the monotemporal datasets, critical pairings dropped to 26. However, the worst pairing green fallow and grain residues had still a very low JM value (0.51). Analogous to P1, the October 2012 dataset was used in P2-stack-2 as additional spectral soil/fallow information. Separability test for P2-stack-2 provided crucial improvements. Of 351 parings only nine were critical (Tab. 3) and even the worst pairing showed a high JM value (1.77).

Tab. 3 (lower part) illustrates the ten worst pairings of all 351 in P2. It is remarkable that watermelons, muskmelons and pumpkins appeared most frequently. All those classes belong to the same botanic family (Cucurbitaceae). At the beginning of plant development the physiognomy of these crops is very similar. As a consequence, these crop types show almost identical spectral reflectance and separation was not feasible. This is well in line with Tigges et al. (2013) who confirmed for multispectral data, that only multitemporal analyses allow distinguishing plants in deeper levels of the botanical taxonomy. A similar observation applies for maize and sorghum which physiognomies are relatively homogenous except for the blossoms and the corncob. These crop types were only separable through the temporal information. Green fallow and grain residues as well as green fallow and orchards appeared as the two worst parings which can be explained by mixed pixels of soil and plant signal. These classes are characterized by very heterogeneous inner-field variations and Tab. 3 indicates that the problem was only solved by adding the soil information from October 2012 (Oct 12).

In order to separate the nine remained pairings, Apr13 was included as an additional dataset for P2. The dataset was acquired on 24th April 2013. At this time harvesting during P1 was completed and plant growth of P2 started for allowing the detection of initial spectral signals of vegetation in the satellite data. P2-stack-3 (Oct12, Apr13, Jun13 and Aug13) including 20 spectral bands provided the best separability for P2. Only green fallow and grain residual remained as a critical pairing. Nevertheless, the JM value of 1.89 still suggested a very high quality of separability.

Tab. 4: Accuracy assessment of ML and SVM for both cultivation periods (t(h) = processing time in hours (OAA = overall accuracy in %)).

Cultivation period		P1	P2
Stacks		P1-stack-2	P2-stack-3
Class No.		16	27
ML	OAA	94.83	93.28
	K	0.93	0.92
	t(h)	5	14
SVM	OAA	96.13	94.01
	K	0.95	0.93
	t(h)	27	82

4.2 *Classification*

The stacks P1-stack-2 and P2-stack-3 showed the best spectral separability for the cultivation periods. Therefore, these multitemporal datasets were selected for both classifiers ML and SVM. The training dataset was used to calibrate ML and SVM and the classifications were applied to the entire mosaics consisting of two RapidEye tiles (1,000 km^2). In order to validate the results, the validation dataset was used to determine OAA and κ. Tab. 4 illustrates the validation results for the performed classifications. OAA and κ indicated very high classification accuracies for both algorithms. 94.83% were classified correctly with ML in P1 and a κ of 0.93 indicated a very robust and highly accurate classification.

With an OAA of 96.13% and κ = 0.95 the SVM provided a slightly higher accuracy, suggesting that SVM was better suited to handle higher dimensional data than ML. The same tendency was observed for P2. Even with 27 classes, the SVM classification accuracy was

far above 90% (94.01%) with κ of 0.93 pointing at very robust classification results (ML: OAA = 93.28%; κ = 0.92). However, besides the classification accuracy, the performance of both classifiers was considered. In comparison to ML the processing time (t in hours) increased about a factor of 5 or 6 for SVM. As a consequence, SVM classification of P2 took 3.5 days for the 27 classes. At least regarding the presented study a slight increase in classification accuracy has to be weighed against a substantial increase in processing time.

According to the separability tests, the Jun13 dataset would allow the best classification result of all monotemporal datasets in P2. Consequently, ML and SVM classification were applied additionally to this dataset to allow a comparison of mono- and multitemporal datasets in the spatial domain.

Fig. 1 compares the mapping of P2 with ML and SVM classifications from Jun13 and P2-stack-3 (best multitemporal separability) for a part of the study site. The Jun13 ML classification provided an OAA of 66.94% (κ = 0.63) while the monotemporal SVM classification at least could classify the Jun13 dataset with an OAA of 77.18% (κ = 0.74). Obviously, for both classifiers a tremendous increase in classification accuracy was achieved using multi- instead of monotemporal datasets. Guerschman et al. 2003 obtained similar results, but only after merging nine agricultural classes to four broader classes.

Lu & Weng (2007) emphasized the 'noisy' results for ML classifications. This is clearly visible for the monotemporal ML classification in Fig. 1. Furthermore, a lot of additional misidentified classes appear in both monotem-

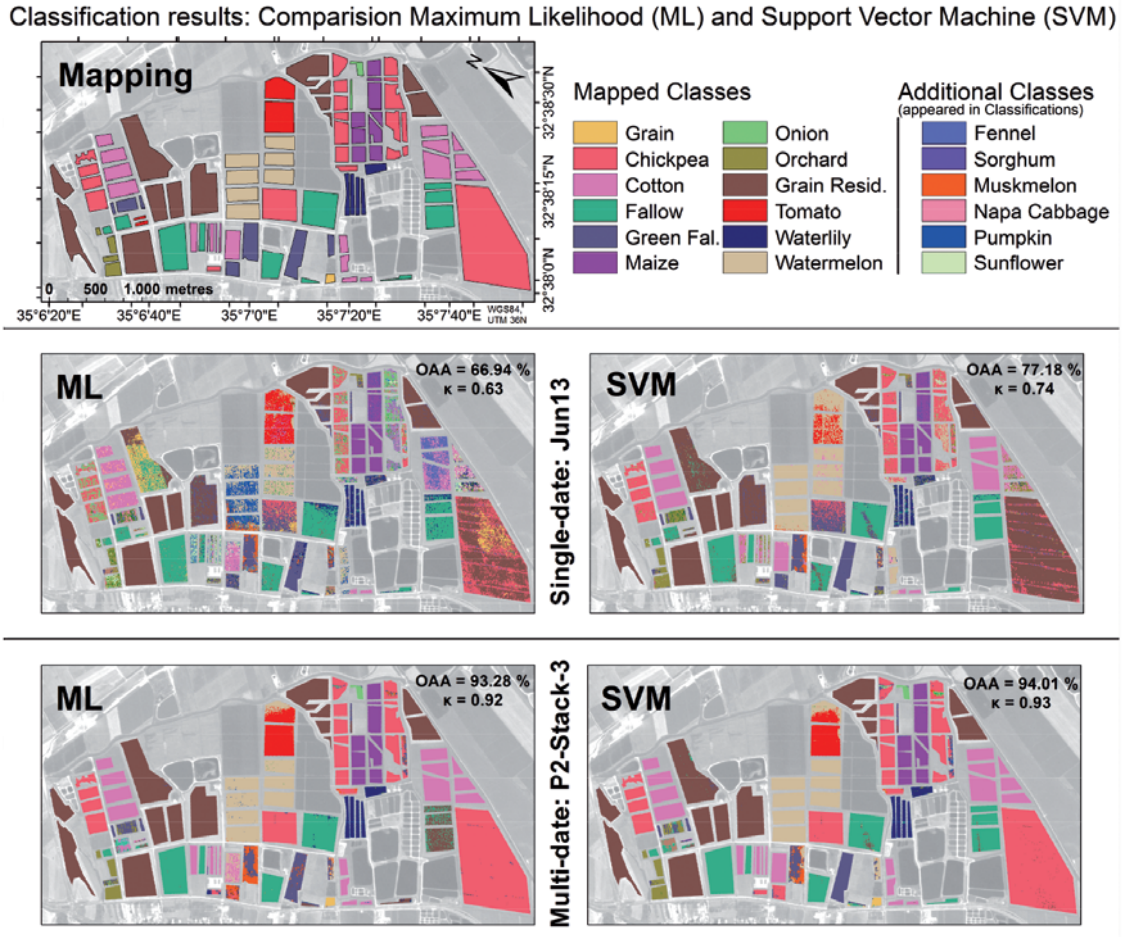

Fig. 1: Comparison of ML and SVM Classification for a monotemporal dataset of June 2013 (Jun13) and a multitemporal dataset (P2-stack-3) for a part of the study site.

poral classifications ML and SVM. These classes occurred in the classification of the entire study site but not in the presented subset in Fig. 1. Regarding the large chickpeas field (Fig. 1 rose) in the south, ML was not able to distinguish between chickpeas, grain residues or grains based on the monotemporal image. The SVM in the monotemporal image mostly identified this field as grain residues. In general, chickpeas fields have spectrally a very high inner-field variation and in June the plants were already dried out. Hence, the classifiers could not differentiate between dried grains and dried chickpeas in the single June dataset. The multitemporal classifications, in contrast, showed highly accurate classification results. This refers to additional phenological information, e.g. the signal of young plants in April and the longer lasting growing period at the end of P2, which was helpful to correctly identify chickpeas.

The same applies to the cotton fields in Fig. 1 (pink), especially in the neighbourhood of the already mentioned chickpea field. ML on monotemporal data identified fennel, waterlily, sunflower and other classes instead of cotton. Due to the dry and hot climate conditions in June (Singer 2007) cotton fields need to be irrigated. Furthermore, cotton was cultivated in stripes. Consequently a RapidEye pixel of 25 m^2 contains a mixed signal of soil (dry and irrigated) and plant (cotton). The result of the SVM in this case was slightly better, but only for the multitemporal dataset almost all pixels of the cotton fields were classified correctly. Again, the multitemporal information was the determining factor for crop differentiation. The harvested fields with crop residues (Fig. 1 brown) were classified very precisely except for one field in the north. This field was still covered by a lot of straw during field survey and hence, ML classified most pixels as grains. In general, the P2 mapping contains only a few fields with mature and dry grains. Only the temporal information allowed the separation between unharvested grains and the field with a high amount of grain residues.

Considering only the two multitemporal classifications in Fig. 1, results were very similar, except one fallow in the south of the water reservoirs. The ML of P2-stack-3 was identifying a lot of pixels of this field as grain residues. The classification of the watermelon fields (Fig. 1 crème) was slightly better using the SVM, because the ML identified some pixels as pumpkin. Pumpkins and watermelons are from the same botanic family (Cucurbitaceae) and have a similar appearance at the beginning of the growing season. Especially the ML classification for the monotemporal image showed a strong mixture between these root crops. The multitemporal classifications contain almost no misidentified classes.

5 Conclusions and Outlook

The present study confirmed the assumption that multispectral satellite data have great potential for multitemporal LU/LC mapping of numerous different agricultural classes with high accuracies. RapidEye data are not only convenient from the spatial point of view (5 m GSD, 79 km swath width), but also from radiometry the increased spectral information of multi-date stacks play an important role for crop differentiation. The JM separability was proven as a very useful pre-testing method to find the best stack combination for the spectral separation of different LU/LC classes. For the first cultivation period (P1) with 16 classes and thus 120 class pairings a multi-date stack of three datasets was used to separate almost all classes. Only one pairing remained closely under the threshold. However, the classifications provided accuracies over 90% for both selected classifiers (ML 94.83% and SVM 96.13%). The same applies to the second period (P2). The class separability was incrementally improved by stacking RapidEye tiles of different dates during the growing season. 27 classes were separated with a multi-date dataset of four stacked RapidEye images. Both classification results supported the assumption that multitemporal datasets provide higher potential in LU/LC classification with overall accuracies over 90% (ML 93.28%, SVM 94.01%). SVM showed its suitability for spectral data with higher dimension while ML provided slightly lower classification accuracies for both periods. However, considering the performance, ML classified the entire dataset with about 1,000 km^2 much faster than SVM (by a factor of 5).

The study has demonstrated that stepwise integration of datasets improved the spectral separability between different classes and hence, the classification accuracies. It is expected that additional datasets from the remaining, non-acquired months lead to even better results. The weather conditions for the region of northern Israel are very suitable for optical remote sensing considering cloud coverage. The RapidEye satellites, in addition, have convenient orbit track geometry to acquire the entire study site in one or two overpasses. Therefore, a monthly or a 14 days acquisition cycle should have additional positive effects. The missing months were November, December and February for P1. Especially a February dataset from 2013 would be helpful to consider the development of root crops. Analogous to the April dataset of P2, additional November and December images of 2012 are assumed as helpful to account for different initial phases of crop growth during P1. Covering the entire first cultivation period may allow separating extremely similar crops as well as even different grain types (oat, rye and barley).

The same applies to the missing months May, July and September of P2. A May 2013 image containing spectral information about vegetation at early growing stages would have been preferred over an April 2013 image ensuring that no reflectance of very late crops by chance is included in the classification. Moreover, July as a mid-position of the phenological period may improve the critical separation of some class pairings, such as green fallow and onions. In order to consider late mature crops, a September dataset would have been helpful.

In summary, multitemporal analyses of the complete crop cycle may be improved with a monthly availability of RapidEye or similar optical remote sensing data. In this case, the issue of the most important datasets for crop identification could be investigated allowing the development of a temporally optimized and even more operational procedure.

Acknowledgements

The authors want to thank the German Aerospace Center (DLR), RESA Science Team, Neustrelitz for the support by providing the satellite data of the RapidEye Science Archive (proposal no. 597). We also thank the staff of the DLR (Oberpfaffenhofen), namely Thomas Krauss and Peter Fischer, for the atmospheric correction using the generic processing chain CATENA. The joint research project "Inference of Aerosol and Land Use Interactions from Remote Sensing Data" (AerosolLand, ZN2725 11-76251-99-20/11) was financially supported by the State of Lower-Saxony, Hannover, Germany.

References

Alganci, U., Sertel, E., Ozdogan, M. & Ormeci, C., 2013: Parcel-level identification of crop types using different classification algorithms and multi-resolution imagery in southeastern turkey. – Photogrammetric Engineering and Remote Sensing **79** (11): 1053–1065.

Araújo, G.K.D., Rocha, J.V., Lamparelli, R.A.C. & Rocha, A.M., 2011: Mapping of summer crops in the state of Paraná, Brazil, through the 10-day spot vegetation NDVI composites. – Engenharia Agrícola **2** (4): 760–770.

Askne, J.I., Fransson, J.E., Santoro, M., Soja, M.J. & Ulander, L.M., 2013: Model-based biomass estimation of a semi-boreal forest from multitemporal tandem-x acquisitions. – Remote Sensing **5** (11): 5574–5597.

Bauer, M.E. & Cipra, J.E., 1973: Identification of agricultural crops by computer processing of ERTS MSS data. – Technical Report 030173, LARS, Perdue University, IN, USA.

Brisco, B. & Brown, R., 1995: Multidate sar/tm synergism for crop classification in Western Canada. – Photogrammetric Engineering & Remote Sensing **61** (8): 1009–1014.

Buechel, S.W., Philipson, W.R. & Philpot, W.D., 1989: The effects of a complex environment on crop separability with Landsat TM. – Remote Sensing of Environment **27** (3): 261–271.

Chust, G., Ducrot, D. & Pretus, J.L., 2004: Land cover discrimination potential of radar multitemporal series and optical multispectral images in a Mediterranean cultural landscape. – International Journal of Remote Sensing **25** (17): 3513–3528.

Cruz-Ramírez, M., Hervás-Martínez, C., Jurado-Expósito, M. & López-Granados, F., 2012: A multi-objective neural network based method for cover crop identification from remote sensed data. – Expert Systems with Applications **39** (11): 10038–10048.

Demir, B., Bovolo, F. & Bruzzone, L., 2013: Classification of time series of multispectral images with limited training data. – IEEE Transactions on Image Processing **22** (8): 3219–3233.

Guerschman, J.P., Paruelo, J.M., Bella, C.D., Giallorenzi, M.C. & Pacin, F., 2003: Land cover classification in the Argentine pampas using multi-temporal Landsat tm data. – International Journal of Remote Sensing **24** (17): 3381–3402.

Hall, F.G., Townshed, J.R. & Engman, E.T., 1995: Status of Remote Sensing Algorithms for Estimation of Land Surface State Parameters. – Remote Sensing of Environment **51** (1): 138–156.

Huang, C., Davis, L.S. & Townshend, J.R.G., 2002: An assessment of support vector machines for land cover classification. – International Journal of Remote Sensing **23** (4): 725–749.

Huang, H., Legarsky, J. & Othman, M., 2007: Land-cover classification using Radarsat and Landsat imagery for St. Louis, Missouri. – Photogrammetric Engineering and Remote Sensing **73** (1): 37–43.

IMS, 2014: Israeli Metereological Survey. – http://www.ims.gov.il (1.3.2014).

Khan, G.A., Khan, S.A., Zafar, N.A., Ahmad, F. & Islam, S., 2012: A review of different approaches of land cover mapping. – Life Sciences Journal **9** (4): 1023–1032.

Krauss, T., d'Angelo, P., Schneider, M. & Gstaiger, V., 2013: The Fully Automatic Optical Processing System CATENA at DLR. – ISPRS International Archives of Photogrammetry Remote Sensing Spatial Information Science **XL-1/W:** 177–181, Copernicus Publications, ISPRS Hannover Workshop 2013.

Liu, Q.J., Takamura, T., Takeuchi, N. & Shao, G., 2002: Mapping of boreal vegetation of a temperate mountain in China by multitemporal Landsat tm imagery. – International Journal of Remote Sensing **23** (17): 3385–3405.

Lu, D. & Weng, Q., 2007: A survey of image classification methods and techniques for improving classification performance. – International Journal of Remote Sensing **28** (5): 823–870.

Lunetta, R.S. & Balogh, M.E., 1999: Application of multi-temporal Landsat 5 tm imagery for wetland identification. – Photogrammetric Engineering and Remote Sensing **65** (11): 1303–1310.

Mariotto, I., Thenkabail, P.S., Huete, A., Slonecker, E.T. & Platonov, A., 2013: Hyperspectral versus multispectral crop-productivity modeling and type discrimination for the hyspiri mission. – Remote Sensing of Environment **139:** 291–305.

Mathur, A. & Foody, G.M., 2008: Crop classification by support vector machine with intelligently selected training data for an operational application. – International Journal of Remote Sensing **29** (8): 2227–2240.

Mountrakis, G., Im, J. & Ogole, C., 2011: Support vector machines in remote sensing: A review. – ISPRS Journal of Photogrammetry and Remote Sensing **66** (3): 247–259.

Mulla, D.J., 2013: Twenty five years of remote sensing in precision agriculture: Key advances and remaining knowledge gaps. – Biosystems Engineering **114** (4): 358–371, Special Issue: Sensing Technologies for Sustainable Agriculture.

Murakami, T., Ogawa, S., Ishitsuka, N., Kumagai, K. & Saito, G., 2001: Crop discrimination with multitemporal spot/hrv data in the Saga plains, Japan. – International Journal of Remote Sensing **22** (7): 1335–1348.

Oetter, D.R., Cohen, W.B., Berterretche, M., Maiersperger, T.K. & Kennedy, R.E., 2001: Land cover mapping in an agricultural setting using multiseasonal thematic mapper data. – Remote Sensing of Environment **76** (2): 139–155.

Richards, J., 2005: Analysis of remotely sensed data: the formative decades and the future. – IEEE Transactions on Geoscience and Remote Sensing **43** (3): 422–432.

Sesnie, S.E., Finegan, B., Gessler, P.E., Thessler, S., Bendana, Z.R. & Smith, A.M.S., 2010: The multispectral separability of costa rican rainforest types with support vector machines and random forest decision trees. – International Journal of Remote Sensing **31** (11): 2885–2909.

Singer, A., 2007: The Soils of Israel. – 306 p., Springer, Berlin, Heidelberg.

Tigges, J., Lakes, T. & Hostert, P., 2013: Urban vegetation classification: Benefits of multitemporal RapidEye satellite data. – Remote Sensing of Environment **136:** 66–75.

Thenkabail, P.S., Lyon, J.G. & Huete, A., 2010: Hyperspectral remote sensing of vegetation and agricultural crops: knowledge gain and knowledge gap after 40 years of research. Ch. 28. – Thenkabail, P.S., Lyon, J.G. & Huete, A. (eds.), 2011: Hyperspectral Remote Sensing of Vegetation. – 705 p., CRC Press, Boca Raton, FL, USA.

Thomas, I.L., Ching, N.P., Benning, V.M. & D'Aguanno, J.A., 1987: Review article a review of multi-channel indices of class separability. – International Journal of Remote Sensing **8** (3): 331–350.

Vapnik, V.N., 1999: An Overview of Statistical Learning Theory. – IEEE Transactions on neural networks **10** (5): 988–999.

Vicente-Guijalba, F., Martinez-Marin, T. & Lopez-Sanchez, J., 2014: Crop phenology estimation using a multitemporal model and a Kalman filtering strategy. – IEEE Geoscience and Remote Sensing Letters **11** (6): 1081–1085.

Waske, B. & van der Linden, S., 2008: Classifying multilevel imagery from sar and optical sensors by decision fusion. – IEEE Transactions on Geoscience and Remote Sensing **46** (5): 1457–1466.

Weichelt, H., Rosso, P., Marx, A., Reigber, S., Douglass, K. & Heynen, M., 2013: The RapidEye red edge band. – Technical report, BlackBridge, Berlin.

Wondrade, N., Ostein, B.D. & Tveite, H., 2014: Gis based mapping of land cover changes utilizing multi-temporal remotely sensed image data in lake Hawassa watershed, Ethiopia. – Environmental Monitoring and Assessment **186** (3): 1765–1780.

Address of the Authors:

Florian Beyer, Dr. Thomas Jarmer & Bastian Siegmann, Institute for Geoinformatics and Remote Sensing, Osnabrück University, Barbarastr. 22b, D-49076 Osnabrück, Tel.: +49-541-969-3930, Fax: +49-541-9693939, e-mail: {fbeyer}{tjarmer}{bsiegmann}@igf.uos.de

Manuskript eingereicht: April 2014
Angenommen: Juli 2014

PFG 2015 / 1, 0033–0043
Stuttgart, February 2015

Article

Multitemporale und kantenbasierte Analyseverfahren zur Detektion agrarischer Landnutzungsdynamiken auf Teneriffa

Sebastian Günthert, Simone Naumann & Alexander Siegmund, Heidelberg

Keywords: Veränderungsanalyse, Objektbasierte Bildanalysen, Canny-Algorithmus, Brachflächen, Kanarische Inseln

Zusammenfassung: Während bis Mitte des 20. Jahrhunderts fast ausschließlich agrarische Inwertsetzungsprozesse das Landschaftsbild Teneriffas prägten, spielen in jüngster Zeit vor allem der Tourismus und damit verbundene Wirtschaftssektoren eine maßgebliche Rolle bei der anthropogenen Umgestaltung des Raums. Der mit dieser Entwicklung einhergehende sozioökonomische Wandel von einer Agrar- zu einer Dienstleistungsgesellschaft führt letztlich zu einer verstärkten Aufgabe von landwirtschaftlichen Nutzflächen im ländlichen Raum. Die quantitative Untersuchung dieser agrarischen Landnutzungsdynamiken stellt das Hauptziel der folgenden Studie dar. Die Grundlage hierfür bildet die quantitative Auswertung objektbasierter Landnutzungsklassifizierungen von SPOT 1-Daten (1986/88), SPOT 4-Daten (1998) sowie RapidEye-Daten (2010) anhand eines modifizierten, multitemporalen Post-Klassifikations-Vergleichs. Darüber hinaus wird ein weiterer objektbasierter Klassifizierungsprozess zur Erfassung der landwirtschaftlich beeinflussten Gesamtfläche Teneriffas anhand hochauflösender RGB-Orthophotos vorgestellt. Hauptaugenmerk dieses Verfahrens liegt auf der kantenbasierten Detektion von Agrarflächen inklusive landwirtschaftlich stillgelegter Areale bzw. Sukzessionsbrachen. Die Ergebnisse zeigen auf, dass zahlreiche Ackerbauregionen insbesondere im humiden Norden der Insel durch kontinuierliche Flächenstilllegungen gekennzeichnet sind. Darüber hinaus wird deutlich, dass etwa ein Drittel der Gesamtfläche Teneriffas durch agrarische Nutzung geprägt ist. Etwa 72% dieser Fläche bestehen derzeit jedoch aus Sukzessionsbrachen.

Summary: *Multitemporal and edge-based analysis techniques for detecting agricultural land use dynamics on Tenerife*. Whereas, until the mid-20th century, mainly agricultural processes characterised the landscape structure of Tenerife, tourism and related economic sectors have had the greatest effect on the anthropogenic landscape transformation in recent times. The associated socioeconomic change from an agricultural to a service economy has led to an increased abandonment of agricultural land in rural areas. The quantitative analysis of these agricultural land use dynamics is the main objective of the following study. For this purpose a quantitative analysis of object-based land use classifications of SPOT 1-data (1986/88), SPOT 4-data (1998) as well as RapidEye-data (2010) has been done, based on a modified, multitemporal post classification comparison. Moreover, an additional object-based classification process for identifying the total agriculturally affected area of Tenerife on the basis of high-resolution RGB orthophotos is presented. This method focuses on the edge-based detection of agricultural land, including agricultural set-aside respectively successional fallow areas. The results obtained indicate, that many agricultural regions especially in the north of the island are characterised by continuous agricultural abandonment. In addition, the analysis shows that about one third of the total area of Tenerife is shaped by agricultural use. However, at present approximately 72% of this area consists of agricultural set-aside.

www.schweizerbart.de
DOI: 10.1127/pfg/2015/0244
1432-8364/15/0244 $ 3.00

1 Einleitung

Das heutige Landschaftsbild Teneriffas, der mit 2.057 km² größten Insel des Kanarischen Archipels, kann als das Ergebnis einer beständigen kulturlandschaftlichen Entwicklung angesehen werden, die hauptsächlich mit dem Beginn der europäischen Kolonialisierung im 15. Jahrhundert ihren Anfang nahm und bis heute andauert. Bis Mitte des 20. Jahrhunderts prägten dabei fast ausschließlich landwirtschaftliche Inwertsetzungsprozesse das Landschaftsbild der Insel. Das gesamte Untersuchungsgebiet unterliegt somit einer flächenintensiven landwirtschaftlichen Nutzung, die grundsätzlich in zwei Arten unterteilt werden kann: Eine exportorientierte, hochentwickelte Intensivlandwirtschaft in Form von Plantagen und Gewächshauskulturen sowie eine traditionelle Landwirtschaft für die Produktion von Waren für den lokalen Markt. Letztgenannte wird vornehmlich in Form von Terrassenfeldbau betrieben. Durch die Anlage von meist aus Basaltgestein bestehenden Mauern können steile Hänge urbar gemacht werden. Auf ebeneren Flächen dienen die Basaltmauern zum Schutz vor Bodenerosion bei Starkregenereignissen (Otto 2003, S. 59). Hauptanbauprodukte für den lokalen Markt sind vor allem Kartoffeln, Weintrauben und subtropische Früchte. Die exportorientierte Landwirtschaft umfasst hingegen den Anbau von Bananen, Tomaten und Schnittblumen (Günthert et al. 2011, Villa et al. 2003).

In jüngerer Zeit – insbesondere seit den 1990er Jahren – spielen jedoch vor allem der Tourismus und damit verbundene Wirtschaftssektoren eine maßgebliche Rolle bei der anthropogenen Umgestaltung des Raums. Der mit dem Tourismusboom einhergehende sozioökonomische Wandel von einer Agrar- zu einer Dienstleistungsgesellschaft führt zu einer zunehmenden Versiegelung der Küstenzonen infolge verstärkter Siedlungsexpansionen und dem Ausbau weiterer, überwiegend touristisch bedingter Infrastruktur (Naumann 2008). Andererseits führt die Abwanderung der Bevölkerung und die Umorientierung der Erwerbstätigen von der Landwirtschaft hin zum lukrativen Tourismus zu einer verstärkten Aufgabe von landwirtschaftlichen Nutzflächen im Hinterland (Pott et al. 2003). Diese Brachflächen bieten potenziellen Raum, auf dem sich angrenzende Ökosysteme durch sekundäre Sukzessionsprozesse wieder auf natürliche Weise ausbreiten können (Fernández-Palacios & Whittaker 2008).

Die vorliegende Studie zielt darauf ab, die räumlichen Veränderungsprozesse und -muster der landwirtschaftlichen Entwicklung der gesamten Insel im Rahmen des sozioökonomischen Wandels quantitativ zu identifizieren und insbesondere regionale Hot Spots landwirtschaftlicher Flächenveränderung zu erfassen, die durch eine kontinuierliche Agrarflächenabnahme oder -zunahme sowie eine besonders hohe Veränderungsintensität geprägt sind. Darüber hinaus soll eruiert werden, welche Areale bislang für landwirtschaftliche Zwecke inwertgesetzt wurden und wie hoch der Anteil rezent bewirtschafteter Agrarflächen bzw. landwirtschaftlich stillgelegter Areale an der landwirtschaftlich beeinflussten Gesamtfläche Teneriffas ist. Die hierdurch gewonnenen Ergebnisse stellen die Grundlage zur Analyse und Bewertung des Regenerationspotenzials, das sich durch die Entstehung von Brachflächen für die teilweise stark anthropogen überprägten Pflanzenformationen der Insel, beispielsweise des kanarischen Lorbeerwaldes, ergibt (vgl. Günthert 2014).

2 Datengrundlage und -aufbereitung

Die Grundlage zur quantitativen Erfassung der agrarischen Landnutzungsveränderungen auf Teneriffa bilden objektbasierte Landnutzungsklassifizierungen (LU-Klassifizierungen) von 1986/88 (Overall Accuracy 90,9%), 1998 (OA 89,8%) und 2010 (OA 91,8%) (vgl. Günthert 2014). Diese basieren auf folgenden Satellitenbilddaten, die im Vorfeld ein umfangreiches Pre-Processing, bestehend aus einer Orthorektifizierung (SPOT), Koregistrierung (RapidEye), Atmosphärenkorrektion (ATCOR, Atmospheric Correction), spektralen Bildschärfung mittels des High-Pass-Filter Resolution Merge (SPOT) sowie arithmetischen Pixeloperationen zur Gewinnung weiterer Trennungskriterien während der LU-Klassifizierung (Kalkulation verschiedener Vege-

tationsindizes, PCA und IHS-Transformation) durchlaufen haben:

- SPOT 1 (älteste zur Verfügung stehende, hochauflösende Daten für das Untersuchungsgebiet; Aufnahmejahre 1986, 1987 und 1988): 3 Multispektralszenen (Level 1a, räumliche Auflösung 20 m × 20 m; 3 PAN Szenen (Level 1a, räumliche Auflösung 10 m × 10 m).
- SPOT 4 (Aufnahmejahr 1998): 3 Multispektralszenen (Level 1a, räumliche Auflösung 20 m × 20 m; 3 M-Mode Szenen (Level 1a, räumliche Auflösung 10 m × 10 m).
- RapidEye (Aufnahmejahr 2010): 11 Multispektralszenen (Level 3a, räumliche Auflösung 5 m × 5 m).

Der zur Analyse der multispektralen Fernerkundungsdaten verwendete Segmentierungs- und Klassifizierungsalgorithmus berücksichtigt insgesamt vier Agrarklassen (*Ackerflächen*, *Schwarzbrache*, *Plantagen*, *Gewächshäuser*) sowie die Klasse *Wolken* (SPOT 4 und RapidEye) und *Siedlungsgebiete* (RapidEye). Letztgenannter Landnutzungstyp findet Eingang in die Analyse zur Erfassung der landwirtschaftlich beeinflussten Gesamtfläche (vgl. Kap. 5). Die Agrarklasse *Schwarzbrache* umfasst im Gegensatz zur Klasse *Ackerfläche* alle Areale, die infolge verschiedener ackerbaulicher Maßnahmen, z.B. Pflügen, Einsatz von Herbiziden, planmäßig vegetationslos sind, aber dennoch einer geregelten agrarischen Nutzung unterliegen (vgl. Brunotte et al. 2002). *Plantagen* hingegen beinhalten großflächige Monokulturen. Der Landnutzungstyp *Gewächshäuser* bezieht sich schließlich auf jene Agrarflächen, die von Plastikfolien überspannt sind.

Ein Orthophoto-Mosaik von Cartográfica de Canarias S.A. (GRAFCAN) (Aufnahmejahr 2009, 389 vorprozessierte Einzelbilder, räumliche Auflösung 40 cm × 40 cm) diente als Referenzdatensatz für die Orthorektifizierung und Koregistrierung der genannten Fernerkundungsdaten. Es bildet zudem die Grundlage zur kantenbasierten Detektion der landwirtschaftlich beeinflussten Gesamtfläche. Weitere in der Studie verwendete Daten umfassen ein digitales Geländemodell mit einer räumlichen Auflösung von 10 m × 10 m sowie eine digitale Straßenkarte des Untersuchungsgebiets von GRAFCAN.

3 Veränderungsanalyse zur Erfassung der rezenten Agrardynamik

Der klassische Post Classification Comparison (PCC) Algorithmus basiert im Allgemeinen auf dem pixel- oder objektbasierten Vergleich bi-temporaler Datensätze. Die daraus resultierende Veränderungsmatrix in Form eines thematischen Layers zeigt auf, wo klassenspezifische, räumliche Veränderungen zwischen Untersuchungszeitpunkt t_1 und t_2 zu beobachten sind (Campbell 2006). Die alleinige Berechnung solcher „from-to"-Informationen bietet jedoch nicht die Möglichkeit, räumlich unterschiedliche Veränderungsintensitäten im Untersuchungsgebiet quantitativ zu detektieren. Diese sind jedoch zur Erfassung von möglichen Hot Spots landwirtschaftlicher Flächenveränderung unabdingbar. Im Rahmen der vorliegenden Studie wird daher ein PCC-Algorithmus angewandt, der eine quantitative Erfassung räumlicher Agrardynamiken berücksichtigt und sowohl eine bi- als auch tritemporale Auswertung der Daten in z.T. hierarchisch abhängigen Analyseebenen ermöglicht.

Grundlage zur Berechnung von Veränderungsintensitäten bildet die Erzeugung eines Raster-Grids mit einer den Input-Daten übergeordneten Zellgröße von 500 m × 500 m. Innerhalb jeder erzeugten Rasterzelle kann nun zunächst die Veränderung der einzelnen Klassen während eines spezifischen Untersuchungszeitraums berechnet werden, indem die klassenspezifische Fläche $Area_{lu}$ des zeitlich älteren thematischen Datensatzes t_1 von der Fläche des aktuelleren Datensatzes t_2 subtrahiert wird: $Area_{lu}(t_2)$-$Area_{lu}(t_1)$ (vgl. Günthert 2014). Durch eine Addition der erzeugten klassenspezifischen Flächenveränderungen in einer zweiten Hierarchieebene innerhalb des PCC-Algorithmus können darüber hinaus weitere thematische Veränderungskarten erzeugt werden: die so genannte Netto-Veränderung der Landwirtschaft für 1986/88 bis 1998 sowie für 1998 bis 2010. Werden diese Informationen erneut addiert, kann die Gesamt-Nettoveränderung der Landwirtschaft von 1986/88 bis 2010 berechnet werden (vgl. Abb. 2).

Der Zwischenschritt, der zur Berechnung dieses finalen Ergebnisses führt, ermöglicht die zusätzliche Untersuchung der Veränderungshistorie. Ist eine Rasterzelle durch eine stetige Abnahme, also einen Rückgang der Agrarfläche sowohl zwischen 1986/88 und 1998 als auch zwischen 1998 und 2010, geprägt, wird sie der Klasse *Kontinuierliche Abnahme* zugeordnet. Umgekehrt verhält es sich mit der Klasse *Kontinuierliche Zunahme*. Bei allen weiteren Veränderungskombinationen, beispielsweise einer Zunahme zwischen 1986/88 und 1998 sowie einer Abnahme zwischen 1998 und 2010, wird die Rasterzelle stattdessen als *Dynamische Veränderung* charakterisiert.

Die in der vorliegenden Studie speziell für Veränderungen landwirtschaftlicher Nutzflächen auf Teneriffa entwickelte Veränderungsanalyse (Change-Detection-Analyse) verläuft nach einer Festlegung der zu untersuchenden Landnutzungsklassen automatisiert. Das Verfahren ist daher leicht auf andere klassifizierte Datensätze übertragbar. Die Rasterzellengröße kann dabei in Abhängigkeit von der räumlichen Auflösung der Daten sowie von der Größe des Untersuchungsgebietes spezifisch angepasst werden.

4 Kantenbasierte Detektion der landwirtschaftlich beeinflussten Gesamtfläche anhand hochauflösender Orthophotos

Die Untersuchungen im Rahmen der Veränderungsanalyse (Change-Detection-Analyse) beschränken sich ausschließlich auf die Erfassung rezent genutzter Agrarflächen im Untersuchungsgebiet seit 1986/88. Feldforschungen und Auswertungen alter Luftbildaufnahmen zeigen jedoch, dass neben den detektierten Gebieten zahlreiche weitere Flächen für landwirtschaftliche Zwecke genutzt worden sind, deren aktive Nutzung jedoch zum Teil schon mehrere Dekaden vor 1986/88 zurückreicht. Die für eine gesamtlandwirtschaftliche Untersuchung notwendige Detektion dieser ehemals genutzten Agrarflächen ist in den verwendeten Satellitenbilddaten nur schwerlich möglich, da natürliche Sukzessionsvorgänge je nach Dauer der Brachephase zu einer teilweisen oder vollständigen Wiederbesiedlung der Flächen durch benachbarte Pflanzenformationen geführt haben. Unter alleiniger Verwendung spektraler Informationen können sie somit nicht mehr von der natürlichen, anthropogen unbeeinflussten Vegetationsbedeckung unterschieden werden (Günthert et al. 2012).

Diese Sukzessionsbrachen (vgl. Brunotte et al. 2002) bzw. landwirtschaftlich stillgelegten Areale können oftmals nur noch durch Landschaftsrelikte, die auf ihre ehemalige agrarische Nutzung hinweisen, identifiziert werden. Hierzu zählen insbesondere die zur Terrassierung von Flächen errichteten Trockenmauern, die sich aufgrund der vorherrschenden orographischen Bedingungen über weite Teile des Untersuchungsgebiets erstrecken. Bewirtschaftete Agrarflächen weisen darüber hinaus neben Trockenmauern zahlreiche weitere lineare Elemente auf. Hierzu zählen beispielsweise Ackerfurchen, Flur- und Feldgrenzen sowie lineare Pflanzmuster. Die Erfassung der landwirtschaftlich beeinflussten Gesamtfläche, die sowohl alle rezenten landwirtschaftlich genutzten wie auch stillgelegten Areale im Untersuchungsgebiet repräsentiert, steht demnach in direkter Beziehung zur Detektion linearer landwirtschaftlicher Strukturen, sofern diese in den zur Analyse verwendeten Bilddaten erfasst werden können. Es bedarf daher eines Detektionsverfahrens, das anstatt spektraler Attribute einzig lineare Merkmale zur Erfassung von Agrarflächen berücksichtigt.

Die Grundlage zur Detektion und Extraktion von linearen Agrarstrukturen aus Fernerkundungsdaten bilden im Allgemeinen verschiedene Bildbearbeitungsverfahren wie Textur-Filter (Kantendetektoren) oder Wavelet-Transformationen (vgl. Turker & Kok 2013, Ishida et al. 2004, Rydberg & Borgefors 2001, Ji 1996). Die Berücksichtigung der daraus resultierenden Informationen dient dabei vor allem einem Ziel, nämlich der Erhöhung der Detailgenauigkeit infolge eines verbesserten räumlichen Differenzierungsgrades zwischen den jeweiligen agrarischen Landnutzungseinheiten. Die zu ermittelnden linearen Einheiten sind in der vorliegenden Studie jedoch vielmehr als so genannte Agrarproxys aufzufassen, durch deren Auftreten eine Unterscheidung zwischen landwirtschaftlich be-

einflussten und unbeeinflussten Arealen im Untersuchungsgebiet ermöglicht wird. Voraussetzung zur Erfassung vorhandener Landwirtschaftstrukturen ist eine ausreichend hohe räumliche Auflösung der zu analysierenden Fernerkundungsdaten. RGB-Orthophotos des Untersuchungsgebiets (räumliche Auflösung 40 cm × 40 cm) bieten hierfür eine sehr gute Grundlage, da sich Terrassen und Trockenmauern selbst bei einer dichten Vegetationsdecke noch sehr gut identifizieren lassen (Günthert 2014). Der speziell zur Erfassung der landwirtschaftlich beeinflussten Gesamtfläche Teneriffas entwickelte, kantenbasierte Klassifizierungsprozess dient daher der Auswertung von Orthophotos und besteht aus der Kombination von insgesamt sechs verschiedenen Teilanalysen (vgl. Abb. 1).

4.1 *Kantendetektion mittels Canny Edge Detector*

Zur Detektion von linearen landwirtschaftlichen Strukturen und deren Verwendung als Agrarproxys ist zunächst ein Pre-Processing der Orthophotos in Form einer Kantenfilterung erforderlich. Ein häufig zur Detektion von Agrarstrukturen aber auch zur Erfassung von urbanen und topographischen Mustern eingesetzter Operator ist der Canny-Algorithmus (Canny Edge Detector) (vgl. Turker & Kok 2013, Liu et al. 2010, Canny 1986). Aufgrund seiner hohen Performanz gegenüber anderen Techniken wie beispielsweise dem Prewitt's Operator, Robert's Cross Operator oder dem Laplacian of Gaussian (Juneja & Sandhu 2009) wird dieser in der vorliegenden Untersuchung zur Erfassung linearer Agrarstrukturen verwendet (vgl. Abb. 1, Bild 2).

Die Kantenfilterung durch den Canny-Algorithmus wird durch drei Faktoren determiniert: Breite des Gauß-Filters innerhalb der Glättungsphase, Festlegung eines unteren sowie oberen Schwellenwertes im Rahmen eines Hysterese-Verfahrens. Die Schwellenwerte dienen zur weiteren Reduktion der Gradientenspannweite, nachdem das geglättete Bild durch einen Sobel-Operator in x- und y-Richtung gefaltet, die Stärke sowie Orientierung der Gradientvektoren bestimmt und eine Non-Maximum Suppression durchgeführt wurde (Turker & Kok 2013, Liu et al. 2010, Juneja & Sandhu 2009, Canny 1986).

Die Canny-Kantendetektion erfolgt in den einzelnen Teilszenen mit einer Halbwertsbreite (Full Width at Half Maximum, FWHM) von 2 für die Gauß-Filterung. Dieser relativ niedrige Wert gewährleistet eine ausreichend hohe Detailgenauigkeit auch nach der Bildglättung. Für die beiden Schwellenwerte wird ebenfalls ein niedriger Wertebereich von 0,01 (Low) und 0,08 (High) definiert. Das daraus resultierende Kantenbild beinhaltet zwar eine große Anzahl an Kantenfragmenten, die tatsächlichen Agrarstrukturen wie Trockenmauern und Feldgrenzen sind jedoch durch sehr gleichmäßige, zusammenhängende Linien dargestellt.

4.2 *Segmentierung der kantengefilterten Orthophotos und Klassifizierung von linearen Agrarstrukturen*

Auf Grundlage der kantengefilterten Fernerkundungsdaten wird in einem weiteren Analyseschritt eine Bildsegmentierung und anschließende Klassifizierung von linearen Agrarstrukturen durchgeführt (vgl. Abb. 1, Bild 3). Die klassifizierten Elemente stellen die Basis für die darauffolgende Erfassung der landwirtschaftlich beeinflussten Gesamtfläche dar.

Für die Multiresolution-Segmentierung[1] wird ein niedriger Skalierungsparameter von 3 sowie Homogenitätskriterien von 0,1 sowohl für Shape als auch für Compactness verwendet. Zur anschließenden Erfassung der linearen Agrarobjekte werden weitere Eingangsdaten, d.h. das digitales Geländemodell (DTM), die Straßennetzkarte sowie die Flächen der Objektklasse *Siedlungsgebiete* aus der Landnutzungsklassifizierung 2010, in den Klassifizierungsprozess integriert. Die Klassifizierung der Kantensegmente zielt darauf

[1] Die Multiresolution Segmentierung und die darauffolgende objektbasierte Klassifizierung wurden mittels eCognition Developer durchgeführt. Nachfolgende Homogenitätskriterien und Merkmalsattribute beziehen sich auf die Software (vgl. Blaschke 2010, Benz et al. 2004).

ab, überwiegend gerade, lange und schmale Agrarobjekte zu erfassen. Das hierfür entwickelte Regelset besteht aus folgenden Merkmalsattributen: Shape-Density, Length, Length/Thickness, Main direction, Shape Index, Layer Value Mean Slope, Layer Value Mean Elevation und Layer Value Standard Deviation Elevation. Die beiden Attribute Shape-Density und Length/Thickness müssen dabei in Relation zum Auftreten des Kiefernwaldes in der jeweils zu untersuchenden Bildszene spezifisch angepasst werden. Diese Waldbestände weisen eine teilweise sehr offene und insbesondere bei Pflanzungen lineare Struktur auf, wodurch es zu erhöhten Fehlklassifizierungen kommen kann. Ist der relative Anteil der Waldflächen in der Szene sehr groß, müssen die Merkmalsbereiche der beiden Attribute enger gefasst werden. Die Berücksichtigung von Layer Value Standard Deviation Elevation gewährleistet, dass besonders in montanen Regionen nur hangparallele Seg-

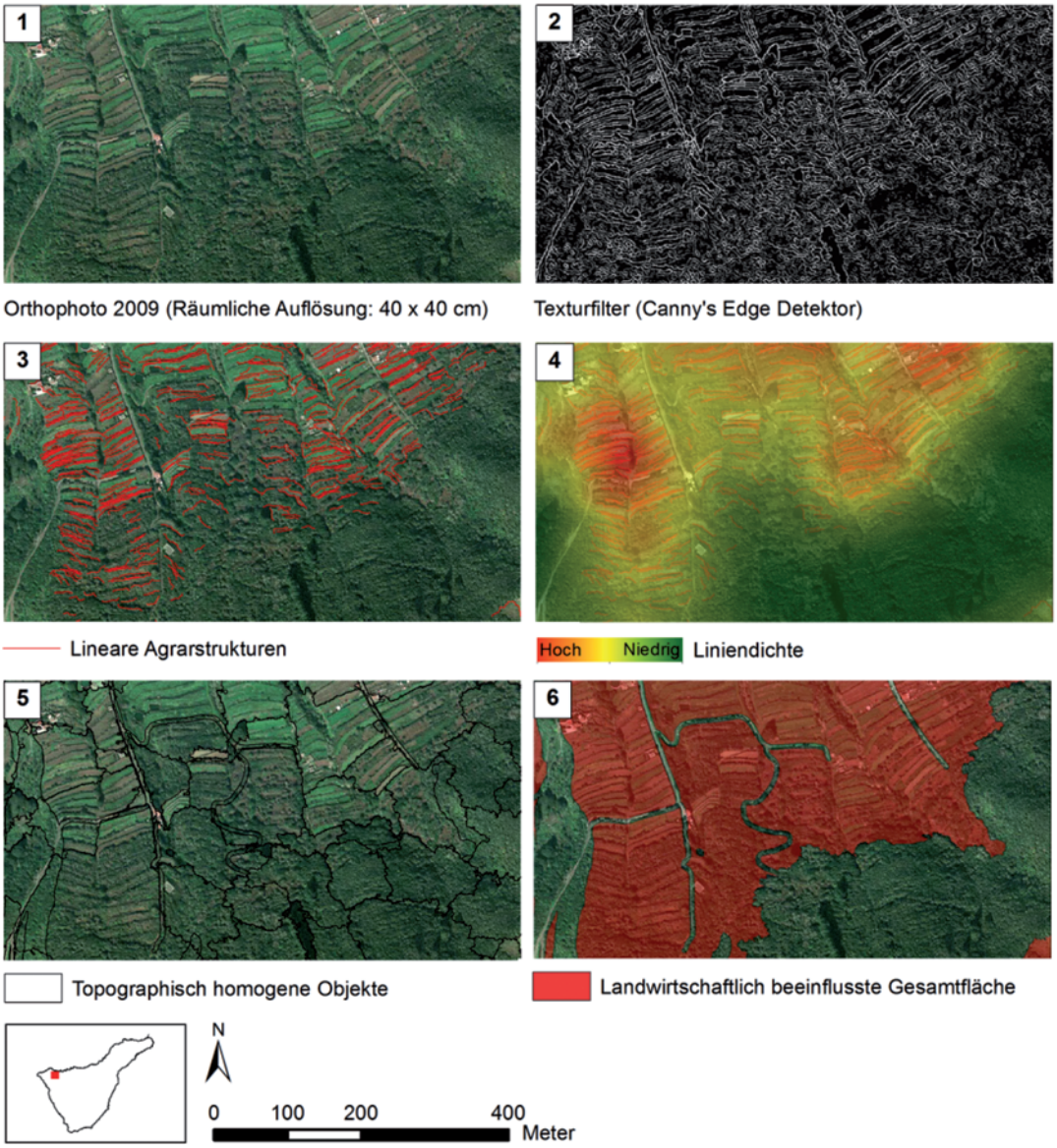

Abb. 1: Bearbeitungsschritte der kantenbasierten Erfassung der landwirtschaftlich beeinflussten Gesamtfläche anhand von Orthophotos (Quellen: Verändert nach Günthert 2014, Datengrundlage Orthophoto: Cartográfica de Canarias S.A. GRAFCAN).

mente als Agrarstrukturen identifiziert werden. Darüber hinaus wird durch eine zusätzliche Regel definiert, dass alle Segmente unberücksichtigt bleiben, die sich innerhalb von Siedlungs-, Gewerbe- oder Straßenflächen befinden. Hierdurch wird verhindert, dass weitere anthropogen bedingte Linearmuster wie Gebäudekomplexe und Verkehrswege klassifiziert werden (Günthert 2014).

4.3 *Transformation von linearer zu flächenhafter Information anhand einer Line-Density-Analyse*

Die als lineare Vektordaten extrahierten Agrarstrukturen geben Aufschluss darüber, wo eine landwirtschaftliche Beeinflussung des Untersuchungsraums vorliegt. Die Detektion von Agrarflächen ist bislang jedoch nur indirekt durch das Überlagern der Orthophotos mit den erfassten Strukturen möglich. Die linienbasierten Informationen müssen demnach so modifiziert werden, dass sie zur flächenhaften Erfassung und Abgrenzung von agrarisch beeinflussten und nicht beeinflussten Arealen verwendbar sind. Dies wird durch eine Line-Density-Analyse (verfügbar in Esri ArcGIS 10.1) ermöglicht (vgl. Abb. 1, Bild 4). Eine Density-Analyse kann als Datenglättungs-Technik bezeichnet werden, mit der Punkt- oder Liniendaten in eine kontinuierliche Oberfläche transformiert werden können (Kloog et al. 2009). Dabei wird anhand der Eingangsvektordaten ein Rasterdatensatz generiert, innerhalb dessen für jede Rasterzelle – abhängig von der räumlichen Verteilung der Eingangsdaten – ein Dichtewert erzeugt wird. Im Rahmen der Line-Density-Analyse wird die Dichte von linearen Features innerhalb eines definierten Radius jeder Ausgabe-Rasterzelle erfasst. Dies geschieht, indem die Länge des Teiles jeder Linie, die in den entsprechenden Radius fällt, addiert und durch die Fläche des so entstandenen Kreises dividiert wird. Die resultierenden Dichteeinheiten werden anschließend in die Maßeinheit „m pro m^2“ konvertiert (Esri 2013).

Die zur Erzeugung des Dichte-Rasters durchgeführte Line-Density-Analyse beruht auf einem Untersuchungsradius von 75 m und einer räumlichen Auflösung des Rasters von 5 m × 5 m. Die so entstandenen kontinuierlichen Flächeninformationen ermöglichen in den nächsten beiden Teilschritten eine Unterscheidung von landwirtschaftlich beeinflussten und unbeeinflussten Flächen (Günthert 2014).

4.4 *Erneute Segmentierung der Orthophotos und Klassifizierung der landwirtschaftlich beeinflussten Gesamtfläche (LbG)*

Der nächste Analyseschritt besteht aus einer erneuten Segmentierung der Orthophotos (vgl. Abb. 1, Bild 5). Hierdurch werden homogene Landschaftsegmente geschaffen, die zur endgültigen Klassifizierung von agrarisch beeinflussten Arealen herangezogen werden können. Die Grundlage zur Segmentierung bilden auch hier neben den RGB-Orthophotos die thematischen Daten in Form der Straßennetzkarte und der Flächen der Objektklasse *Siedlungsgebiete* aus der LU-Klassifizierung 2010. Die Einbeziehung der thematischen Informationen in diesen zweiten Segmentierungsprozess garantiert eine klare Abgrenzung zwischen infrastrukturellen und nichtinfrastrukturellen Objekten. Der zu definierende Skalierungsparameter wird hierbei auf einen hohen Wert von 100 und die Homogenitätskriterien auf einen Faktor von 0,3 für Shape und 0,9 für Compactness gesetzt.

Die erzeugten Landschaftsobjekte werden schließlich im Hinblick auf ihre landwirtschaftliche Beeinflussung klassifiziert (vgl. Abb. 1, Bild 6 und Abb. 3). Hierzu wird auf Grundlage des zuvor generierten Line-Density-Rasters ein spezifischer Wert definiert, ab dem ein Landschaftsobjekt als landwirtschaftlich beeinflusst gilt. Dieser Mindestschwellenwert, der sich auf die durchschnittliche Agrarstrukturdichte pro Objekt bezieht, kann nach einer qualitativen Analyse verschiedener Grenzwerte auf 0,025 m/m^2 beziffert werden, was bei einem Radius von 75 m um die entsprechende Ausgaberasterzelle einer Gesamtlänge von ca. 442 m entspricht. Durch die Verwendung des Schwellenwertes wird gewährleistet, dass Flächen mit sehr vereinzelt auftretenden, nichtagrarischen Linearstruktu-

ren bzw. sehr geringen Dichtewerten von der Klassifizierung der landwirtschaftlich beeinflussten Gesamtfläche ausgeschlossen werden (Günthert 2014).

4.5 *Klassifizierungsgüte*

Zur Ermittlung der Klassifizierungsgenauigkeit des vorgestellten Verfahrens wird eine Konfusionsmatrix (Confusion Matrix) erstellt und entsprechende Gütekriterien abgeleitet (vgl. Tab. 1). Grundlage zur Erfassung der notwendigen Testpixel stellt das Verfahren der geschichteten Zufallsstichprobe mit proportionaler Allokation (Stratified Random, 1000 Referenzpunkte) dar. Als Referenzdatensatz dient aufgrund fehlender bzw. nicht existenter Vergleichsdaten das hochauflösende Orthophoto von 2009. Die Objektklasse *Landwirtschaftlich beeinflusste Gesamtfläche* (LbG) wird dabei einer weiteren Objektklasse *Sonstige Flächen* gegenübergestellt. Letztgenannte Klasse umfasst all jene Gebiete des Untersuchungsgebietes, die im Rahmen des vorliegenden Klassifizierungsprozesses nicht als Agrarflächen detektiert wurden.

Darüber hinaus wurden im Oktober 2011 insgesamt 120 Testflächen innerhalb der als landwirtschaftlich beeinflusst detektierten Areale aufgenommen und mit den Klassifizierungsergebnissen abgeglichen. Auch diese qualitative Vor-Ort-Untersuchung der Klassifizierungsgüte unterstreicht die sehr hohe räumliche Detektionsgenauigkeit des Verfahrens selbst bei sehr alten und somit stark überwucherten Brachflächen.

Tab. 1: Error-Matrix und daraus abgeleitete Genauigkeits-Indizes der klassifizierten landwirtschaftlich beeinflussten Gesamtfläche (Quelle: Verändert nach Günthert 2014)

Objektklasse	**Orthophoto Mosaik 2009**	
	***Pa**	****Ua**
LbG	94,6%	84,5%
Sonstige Flächen	89,1%	96,3%
	Overall accuracy: 91,2%	

* Producer's accuracy ** User's accuracy

5 Interpretation des agrarischen Landnutzungswandels auf Teneriffa

Die Untersuchung des agrarischen Wandels auf Teneriffa zwischen 1986/88 und 2010 in Form einer Gesamt-Nettoveränderungskarte unter Berücksichtigung der Veränderungshistorie zeigt das Ausmaß der agrarischen Flächennutzungsveränderungen (vgl. Abb. 2). So sind zahlreiche großflächig zusammenhängende Areale insbesondere im humiden Norden durch kontinuierliche Flächenstilllegung seit 1986/88 gekennzeichnet. Zu diesen Hot Spots landwirtschaftlichen Flächenrückgangs zählen insbesondere die montanen Regionen im südlich von Buenavista del Norte gelegenen Teno-Massiv, die Region um Puerto de La Cruz, die südlich von Puerto de la Cruz gelegenen Berghänge des Orotava-Tals sowie das Anbaugebiet rund um La Laguna. Das touristische Ballungsgebiet im Südwesten Teneriffas zeigt im Vergleich ebenfalls kontinuierliche Arealverluste. Diese fallen jedoch absolut betrachtet deutlich geringer aus. Gründe hierfür liegen vor allem in der Intensivierung von Agrarland in Form von Gewächshauskulturen, vor allem Bananen- und Tomatenanbau unter Folie. Dem detektierten Flächenrückgang stehen vor allem im Süden des Untersuchungsraums vereinzelte Hot Spots kontinuierlicher Agrarflächenzunahme gegenüber. Während dieser Trend in den südlichen Küstengebieten auf die Neuentstehung von Gewächshäusern zurückzuführen ist, hängen die Flächenzunahmen in montanen Arealen mit der verstärkten Anlegung von Rebflächen für die Weinproduktion zusammen (Günthert 2014).

Die kantenbasierte Klassifizierung der landwirtschaftlich beeinflussten Gesamtfläche lässt erkennen, dass insgesamt 60.160 ha, also etwa ein Drittel der Gesamtfläche Teneriffas, durch eine rezente oder historische Agrarnutzung geprägt sind. Die Überlagerung dieses Areales mit der landwirtschaftlichen Anbaufläche 2010 erlaubt darüber hinaus eine eindeutige Differenzierung zwischen rezent agrarisch genutzten und landwirtschaftlich stillgelegten Flächen (vgl. Abb. 3). Der Anteil rezent genutzter Areale an der ermittelten Gesamtfläche beträgt dabei nur etwa 28%. Die restlichen 72% bestehen demnach aus stillge-

legten Flächen bzw. Sukzessionsbrachen, die sich vornehmlich in den topographisch und/oder klimatisch benachteiligten Regionen der Insel befinden.

Erste Analysen verdeutlichen, dass diese stillgelegten Areale ein sehr hohes ökologisches Potenzial hinsichtlich der natürlichen Regeneration ökologisch wertvoller Vegetationsgesellschaften wie dem Lorbeerwald aufweisen. So zeigt ein Vergleich von aktuellen Verbreitungskarten spezifischer Pflanzenformationen mit der detektierten landwirtschaftlich beeinflussten Gesamtfläche, dass derzeit etwa 930 ha des Lorbeerwaldes auf ehemals landwirtschaftlich genutzten Arealen zu verorten sind und diese somit als Regenerationsflächen bezeichnet werden können. Beim Sukkulentenbusch, einer Pflanzenformation, die sich inmitten des traditionellen landwirtschaftlichen Kerngebiets befindet, beläuft sich der Anteil der Regenerationsflächen auf ca. 20.740 ha (vgl. Günthert 2014).

Die im Rahmen der Change-Detection-Analyse erfasste räumliche Agrarentwicklung mit einem Rückgang von Nutzflächen vor allem im Norden Teneriffas kann somit zumindest aus ökologischer Sicht positiv bewertet werden. Hält diese Entwicklung weiter an, könnte dies zu einer weiteren räumlichen Ausdehnung der genannten naturnahen Pflanzenformationen führen. Zukünftige Studien sollten die als Regenerationsflächen ausgewiesenen Areale jedoch eingehender hinsichtlich ihres Sukzessionsgrades untersuchen. In diesem Zusammenhang wäre es sinnvoll, eine Kategorisierung der erfassten Sukzessionsflächen, beispielsweise auf Grundlage von Hyperspektraldaten hinsichtlich potenziell notwendiger Aufforstungsmaßnahmen zur Förderung der Biodiversität vorzunehmen.

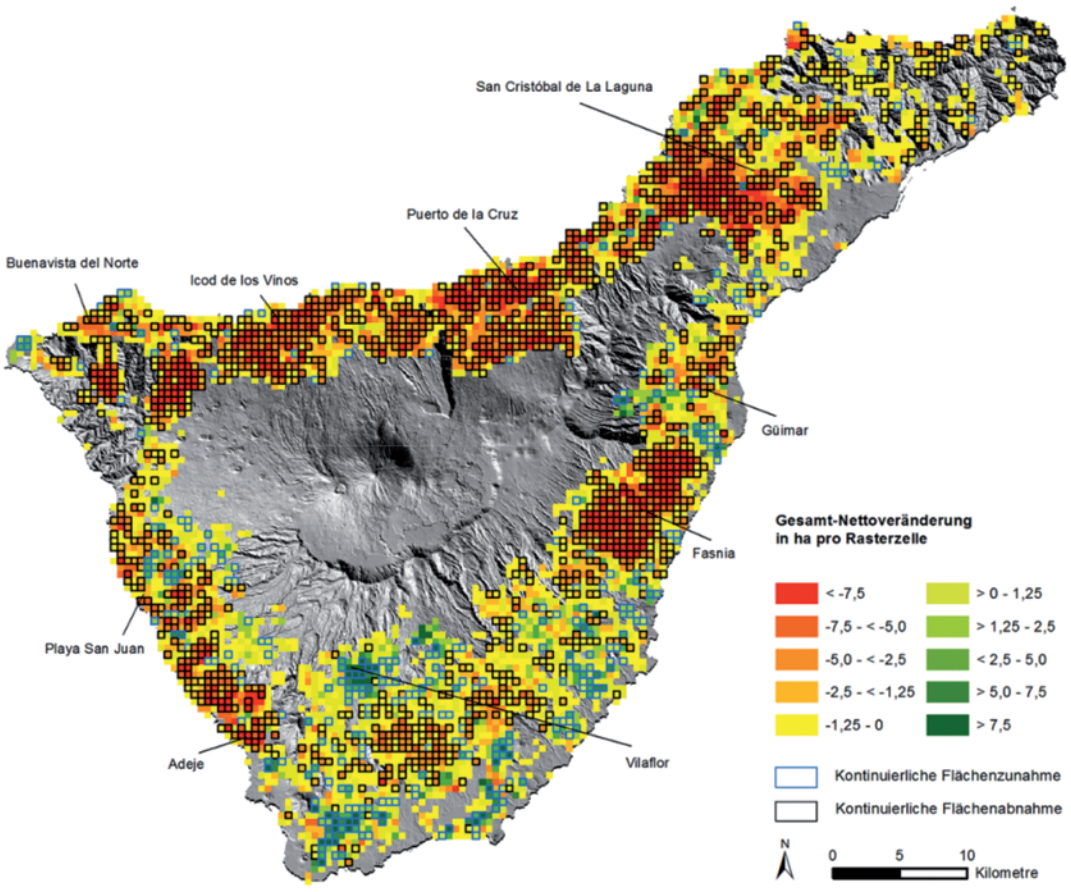

Abb. 2: Gesamt-Nettoveränderung der Landwirtschaft unter Berücksichtigung von Flächen kontinuierlicher Veränderung zwischen 1986/88 und 2010 (Quellen: Günthert 2014, Datengrundlage DTM: Cartográfica de Canarias S.A. GRAFCAN).

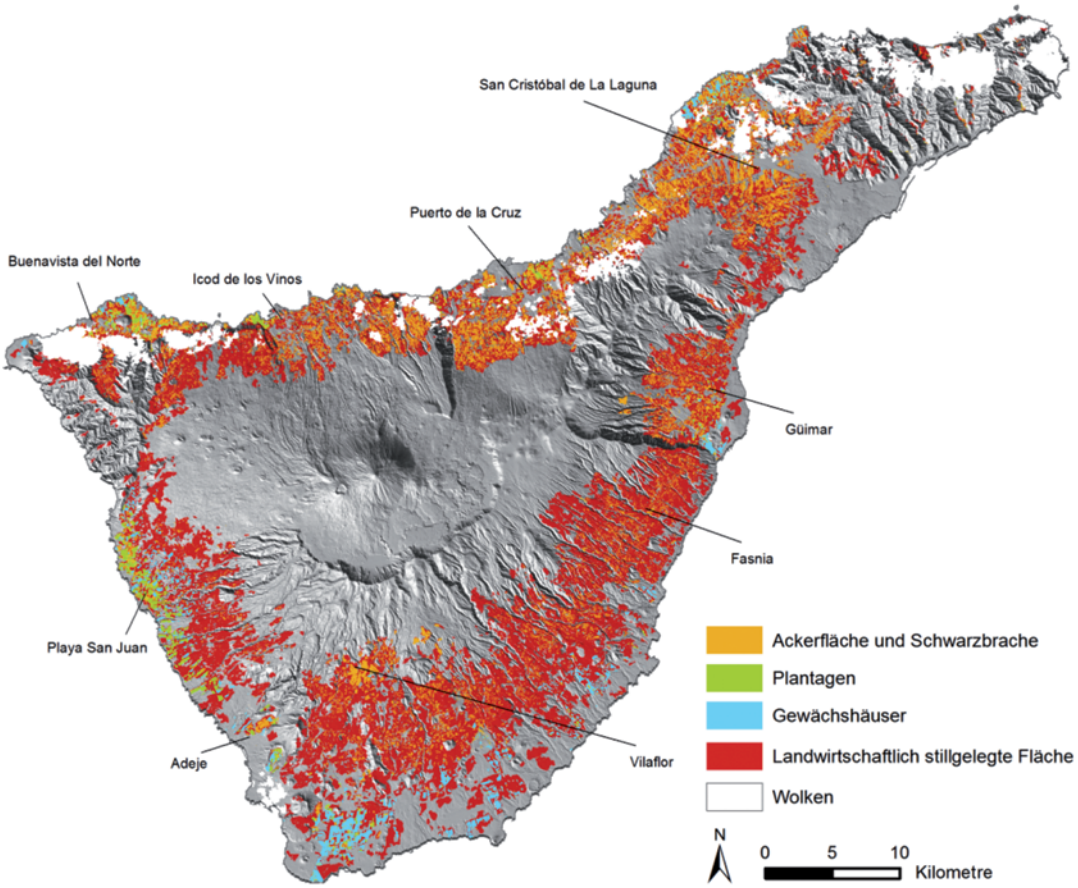

Abb. 3: Agrarisch genutzte und landwirtschaftlich stillgelegte Areale auf Teneriffa im Jahr 2010 (Datengrundlage DTM: Cartográfica de Canarias S.A. GRAFCAN).

Danksagung

Wir danken dem Deutschen Zentrum für Luft- und Raumfahrt e.V. (DLR) für die Bereitstellung von Daten aus dem RapidEye Science Archiv (RESA) sowie dem Centre National d'Études Spatiales (CNES) und SPOT Image S. A. für die Bereitstellung von Daten im Rahmen der Planet Action Initiative.

Literatur

Benz, U.C., Hofmann, P., Willhauck, G., Lingenfelder, I. & Heynen, M., 2004: Multi-resolution, object-oriented fuzzy analysis of remote sensing data for GIS-ready information. – ISPRS Journal of Photogrammetry and Remote Sensing **58** (3–4): 239–258.

Blaschke, T., 2010: Object based image analysis for remote sensing. – ISPRS Journal of Photogrammetry and Remote Sensing **65** (1): 2–16.

Brunotte, E., Gebhardt, H., Meurer, M., Meusburger, P. & Nipper, J., 2002: Lexikon der Geographie. – Spektrum Akademischer Verlag, CD-ROM. Heidelberg, Berlin.

Campbell, J.B., 2006: Introduction to remote sensing. – 4. Auflage, Taylor & Francis, London, UK.

Canny, J., 1986: Computational approach to edge detection. – IEEE Transactions on Pattern Analysis and Machine Intelligence PAMI **8** (6): 679–698.

Esri, 2013: ArcGIS 10.2 – Line Density (Spatial Analyst). –http://resources.arcgis.com/en/help/main/10.2/index.html#//009z0000000t000000 (2.4.2014).

Fernández-Palacios, J.M. & Whittaker, R.J., 2008: The Canaries: an important biogeographical meeting place. – Journal of Biogeography **35** (3): 379–387.

Günthert, S., Siegmund, A., Thunig, H. & Michel, U., 2011: Object-based detection of LUCC with special regard to agricultural abandonment on Tenerife (Canary Islands). – Proceedings of SPIE **8181:** 81811-1–81811-7.

Günthert, S., Naumann, S. & Siegmund, A., 2012: Detection and assessment of land use dynamics on Tenerife (Canary Islands): the agricultural development between 1986 and 2010. – SPIE **8538:** 853804-1–853804-7.

Günthert, S., 2014: Landnutzungsdynamiken und deren ökologische Auswirkungen auf Teneriffa (Kanarische Inseln). Analyse und Bewertung landwirtschaftlicher Entwicklungsprozesse mit Methoden der Fernerkundung und Landnutzungsmodellierung. – Dissertation, Ruprecht-Karls-Universität Heidelberg, Geographisches Institut.

Ishida, T., Itagaki, S., Sasaki, Y. & Ando, H., 2004: Application of wavelet transform for extracting edges of paddy fields from remotely sensed images. – International Journal of Remote Sensing **25** (2): 347–357.

Ji, C.Y., 1996: Delineating agricultural field boundaries from TM imagery using dyadic wavelet transforms. – ISPRS Journal of Photogrammetry and Remote Sensing **51** (6): 268–283.

Juneja, M. & Sandhu, P., 2009: Performance evaluation of edge detection techniques for images in spatial domain. – International Journal of Computer Theory and Engineering **1** (5): 614–621.

Kloog, I., Haim, A. & Portnov, B.A., 2009: Using kernel density function as an urban analysis tool: Investigating the association between nightlight exposure and the incidence of breast cancer in Haifa, Israel. – Computers, Environment and Urban Systems **33** (1): 55–63.

Liu, Z., Gong, P., Shi, P., Chen, H., Zhu, L. & Sasagawa, T., 2010: Automated building change detection using UltraCamD images and existing CAD data. – International Journal of Remote Sensing **31** (6): 1505–1517.

Naumann, S., 2008: Modellierung der Siedlungsentwicklung auf Tenerife (Kanarische Inseln). Eine fernerkundungsgestützte Analyse zur Bewertung des touristisch induzierten Landnutzungswandels. – Heidelberger Geographische Arbeiten 125, Geographisches Institut.

Otto, R., 2003: Räumliche und zeitliche Variabilität des Sukkulentenbuschs auf Tenerife und ihre ökologische Interpretation. – Dissertation. Universität Zürich, Mathematisch-Naturwissenschaftliche Fakultät, Schweiz.

Pott, R., Hüppe, J. & Wildpret de la Torre, W., 2003: Die Kanarischen Inseln. – Natur- und Kulturlandschaften. – Ulmer, Stuttgart.

Rydberg, A. & Borgefors, G., 2001: Integrated method for boundary delineation of agricultural fields in multispectral satellite images. – IEEE Transactions on Geoscience and Remote Sensing **39** (11): 2514–2520.

Turker, M. & Kok, E.H., 2013: Field-based sub-boundary extraction from remote sensing imagery using perceptual grouping. – ISPRS Journal of Photogrammetry and Remote Sensing **79:** 106–121.

Villa, S., Finizio, A., Diaz Diaz, R. & Vighi, M., 2003: Distribution of Organochlorine Pesticides in Pine Needles of an Oceanic Island: The Case of Tenerife (Canary Islands, Spain). – Water, Air, and Soil Pollution **146** (1/4): 335–349.

Adresse der Autoren:

Dr. Sebastian Günthert, Dr. Simone Naumann & Prof. Dr. Alexander Siegmund, Pädagogische Hochschule & Universität Heidelberg, Abteilung Geographie, Research Group for Earth Observation ([r]geo), D-69115 Heidelberg, Tel.: +49-6221-477-792, -797, -771, Fax: +49-6221-477-769, e-mail: {guenthert}, {naumann}, {siegmund}@ph-heidelberg.de

Manuskript eingereicht: Januar 2014
Angenommen: Juli 2014

PFG 2015 / 1, 0045–0054
Stuttgart, February 2015

Article

Estimate Leaf Chlorophyll of Rice Using Reflectance Indices and Partial Least Squares

Kang Yu, Martin Leon Gnyp, Cologne, Lei Gao, Yuxin Miao, Xinping Chen, Beijing, China & Georg Bareth, Cologne

Keywords: Hyperspectral reflectance indices, leaf chlorophyll, rice, Sanjiang Plain, lambda-by-lambda band optimization, partial least squares (PLS)

Summary: In this study field experiments were conducted to test the ability of optimized spectral indices and partial least squares (PLS) to estimate leaf chlorophyll (Chl) content of rice from non-destructive canopy reflectance measurements. We integrated techniques involving the optimization of narrow band spectral indices and the detection of red edge position to optimize one type of spectral indices, the *ratio of reflectance difference index* (RRDI), for the estimation of leaf Chl content. The optimized RRDI in the *red-edge* (RRDIre = $(R_{745}–R_{740})/(R_{740}–R_{700})$) accounted for 62% – 72% of the variation in leaf Chl content with an RMSE of 4.59 µg/cm² – 4.89 µg/cm². Compared to spectral indices, PLS improved the estimation of leaf Chl content, yielding R^2 and RMSE of 0.85 µg/cm² and 3.22 µg/cm², respectively. Finally, the model based on RRDI and the PLS model were further validated by an independent dataset collected in farmer fields. RRDI and PLS models yielded acceptable accuracy with R^2 of 0.49 and 0.55, respectively, and an RMSE of 5.47 µg/cm² and 5.13 µg/cm². Our results suggest the potential to optimize spectral indices and also the significance of PLS technique for mapping canopy biochemical variations.

Zusammenfassung: *Abschätzung von Blatt-Chlorophyllgehalten von Reis mit Hilfe von Spektralindizes und Partial Least Squares Analysen.* In dieser Studie wurden Feldversuche durchgeführt, um optimierte Spektralindizes und Partial Least Squares (PLS) Analysen für die Abschätzung von Blatt-Chlorophyllgehalten von Reis mittels nicht destruktiven Reflexionsmessungen zu evaluieren. Es wurden unterschiedliche Analysemethoden von hyperspektralen Daten integriert. Ziel der Untersuchung ist die Optimierung eines bestimmten Typs von spektralen Indizes, den *Ratio of Reflectance Difference Index* (RRDI). Letzterer wurde für die Abschätzung von Blatt-Chlorophyllgehalten entwickelt. Der optimierte RRDI im *red-edge* (RRDIre = $(R_{745}–R_{740})/(R_{740}–R_{700})$) erklärte 62% – 72% von der Variabilität des Blatt-Chlorophyllgehalts mit einem RMSE von 4.59 µg/cm² – 4.89 µg/cm². Im Vergleich zu etablierten Spektralindizes kann mittels der PLS Analyse die Abschätzung von Blatt-Chlorophyllgehalten signifikant verbessert werden (R^2 = 0.85, RMSE = 3.22 µg/cm²). Schließlich wurden die RRDI- und PLS-basierten Modelle anhand eines unabhängigen Datensatzes, der auf landwirtschaftlich genutzten Feldern erhoben wurde, zusätzlich validiert. Die RRDI- und PLS-Modelle erzielten eine akzeptable Genauigkeit mit jeweils einem R^2 von 0.49 und 0.55 und einem RMSE von 5.47 µg/cm² und 5.13 µg/cm². Unsere Ergebnisse unterstreichen das Potential für die Optimierung von Spektralindizes sowie die Bedeutung von PLS Analysen für die Bestandskartierung von biochemischen Variationen.

1 Introduction

Rice is one of the main agricultural crops in Northeast China. The Sanjiang Plain is well known for large scale farming in China and is becoming more and more important in supplying the food market with commercial rice of high quality (Yao et al. 2012). For a high-yield and environment-friendly agricultur-

www.schweizerbart.de
DOI: 10.1127/pfg/2015/0253 1432-8364/15/0253 $ 2.50

al development, real-time monitoring of the growth status of rice is crucial to this region.

Remote sensing is increasingly being used in agricultural applications owing to its potential for the noninvasively gathering of information over larger areas (Atzberger 2013, Mulla 2013). Hyperspectral remote sensing of crop nutrient status is mainly based on the estimation of leaf chlorophyll (Chl), which absorbs and converts solar light to biochemical energy and thus often serves as an indicator of plant stresses (Filella & Peñuelas 1994). Recent studies have shown great potential of hyperspectral remote sensing for the estimation of leaf chlorophyll (Zarco-Tejada et al. 2001), plant nitrogen (N) (Yu et al. 2013), leaf area index (LAI) (Darvishzadeh et al. 2009), biomass (Gnyp et al. 2013, Gnyp et al. 2014, Koppe et al. 2012) and for disease detection (Delalieux et al. 2009, Laudien et al. 2006, Laudien & Bareth 2006).

The red edge (ca. 680 nm – 750 nm) of spectra is of particular interest for estimating leaf chlorophyll content (Filella & Peñuelas 1994, Main et al. 2011). The red edge position (λ_{RE}) is defined as the wavelength of the peak (local maximum) on the first derivative reflectance spectra (Horler et al. 1983). Generally, λ_{RE} shifts to longer wavelengths with the increase of Chl content (Filella & Peñuelas 1994). Several studies have found that two or more peaks in red edge can be derived from the derivative spectra (Horler et al. 1983, Zarco-Tejada et al. 2002). Horler et al. (1983) suggested that the first peak at around 700 nm is determined mainly by chlorophyll content while the second peak at around 725 nm is governed more by scattering effects.

Recent studies have shown that optimized narrow band spectral indices perform better than broad band indices for the estimation of Chl and LAI (Darvishzadeh et al. 2008, Darvishzadeh et al. 2009). In most of these studies narrow band indices take the forms of simple ratio (SR) and normalized difference vegetation index (NDVI) to find the best band combinations. Yu et al. (2012) found that the optimized SR- and NDVI-like indices have similar sensitive bands and provide equal ability to estimate Chl.

The objective of this study is to test the ability of new spectral indices and the partial least squares (PLS) method to estimate the leaf Chl content of rice.

2 Material and Methods

2.1 *Study Area, Experimental and Farmer Fields*

The study area is located in the Sanjiang Plain, Heilongjiang Province, China. The Sanjiang Plain was originally dominated by marshes and it was converted to agricultural production six decades ago (Yao et al. 2012). The climate in this region is cool-temperate subhumid continental monsoon, with very cold winters and warm summers. The climatic characteristics of Sanjiang Plain are suitable for rice, soybeans, wheat, and corn crops. Rice farming has become the dominant land use in this region in the last two decades. More information about the Sanjiang Plain has been provided elsewhere (Gnyp et al. 2013, Yao et al. 2012, Yu et al. 2013). In this study, two field experiments (Exp. 1 and Exp. 2) were conducted, and 14 farmer fields were selected for data collection.

Exp. 1: The N rate experiment was conducted at two sites: Qixing and Keyansuo experimental stations with a same experimental design in 2008. A randomized complete block design with four replications including five N rates (0, 35, 70, 105 and 140 kg N ha^{-1} as urea, $CO(NH_2)_2$) was applied at both stations, where a local rice cultivar *Kongyu131* was planted. 60 kg ha^{-1} P_2O_5 (as triple super-phosphate) and 75 kg ha^{-1} K_2O (as potassium sulfate) were applied to ensure the supply of other nutrients. All plots had the same size of 100 m^2 (10 m by 10 m).

Exp. 2: Similar design with Exp. 1, Exp. 2 was conducted under five N levels that used 70% of each of the five rates of Exp. 1, which was 0, 24.5, 49, 73.5 and 98 kg N ha^{-1}, respectively. The same cultivar *Kongyu131* and same amount of P- and K-fertilizers were used.

Farmer fields: In addition to the experimental fields, 14 farmer fields managed by two farmers were selected for data collection, which is to be used as the validation dataset. Farmers applied fertilizers according to their own experiences and local practices. The

same cultivar *Kongyu131* was planted in those farmer fields.

2.2 *Spectral Measurement*

Hyperspectral reflectance data was measured from a height of 30 cm above the rice canopy under clear sky conditions within 2 hours of solar noon, using the FieldSpec 3 spectroradiometer (Analytical Spectral Devices, Inc., Boulder, CO, USA) connected to a fiber foreoptic that has a 25 degree field-of-view. The FieldSpec 3 spectroradiometer operates in the 350 nm – 2500 nm spectral region and has a spectral resolution of 3 nm at 700 nm, 10 nm at 1400 nm and 2100 nm. The detailed description of FieldSpec 3 can be found in Gnyp et al. (2013). Hyperspectral reflectance data in 1 nm steps were automatically output by the spectroradiometer. We used the reflectance data of 350 nm – 900 nm in this study due to the specific interest in Chl.

2.3 *Leaf Chlorophyll Measurement*

On the same day of spectral measurements, leaf chlorophyll was measured using a SPAD-502 (Konica Minolta, Inc.) chlorophyll meter. In those spectroradiometer-scanned plants, a total of 10 – 15 newly, fully expanded leaves were selected for recording SPAD values. For each leaf, 3 replicates were recorded in the middle position of the leaf base to tip and then averaged. Finally, SPAD values were transformed to area-based leaf chlorophyll content (Chl, μg/cm^2) using an empirically calibrated function commonly used in remote sensing studies (Atzberger et al. 2003, Darvishzadeh et al. 2008, Markwell et al. 1995).

2.4 *Reflectance Indices*

An NDVI-like index, the normalized reflectance difference index (NRDI, (1)), was optimized using a lambda-by-lambda band optimization (LLBO) method, which has been widely used in recent studies (Darvishzadeh et al. 2008, Darvishzadeh et al. 2009, Yu et al. 2013).

$$NRDI = \frac{R_{\lambda 1} - R_{\lambda 2}}{R_{\lambda 1} + R_{\lambda 2}} \quad (1)$$

where R_λ is the reflectance at the wavelength λ. The LLBO method thoroughly examines all the possible pairs of the bands λ1 and λ2 for NRDI for the correlation with the response variable of interest, chlorophyll in this study.

To test whether we can further improve the robustness of optimized indices, we made a hypothesis, which assumes that R_c is the reflectance in response primarily to chlorophyll and is a function of the wavelength λ, i.e., $R_c = f(\lambda)$. However, due to effects of soil, water background and phenological development, the measured canopy reflectance (R) can be further assumed as a function of R_c and the constants, a and b, that have multiplicative and additive factors respectively, across wavelengths (2),

$$R = a \cdot f(\lambda) + b\,. \quad (2)$$

Although such a linear hypothesis is rare in nature, we expect that it allows for the removal of the adverse effects added to the canopy reflectance (R). R_c could be then calculated by eliminating the factors a and b from the measured reflectance R, following (3),

$$R_c = (R - b)/a\,. \quad (3)$$

However, since a and b are difficult to determine, an alternative approach to eliminate a and b is to use the ratio of reflectance difference as shown in (4),

$$\frac{R_{c,\lambda 1} - R_{c,\lambda 2}}{R_{c,\lambda 3} - R_{c,\lambda 4}} = \frac{R_{\lambda 1} - R_{\lambda 2}}{R_{\lambda 3} - R_{\lambda 4}}\,. \quad (4)$$

Finally, we define the ratio of reflectance difference index (RRDI, (5)) as:

$$RRDI = \frac{R_{\lambda 1} - R_{\lambda 2}}{R_{\lambda 3} - R_{\lambda 4}}\,, \quad (5)$$

for which λ1 – λ4 are random wavelengths to be optimized for the estimation of Chl. The RRDI optimization is achieved through two steps. First step, all possible 2-band combinations of λ1 and λ2 within the range of 350 nm

– 900 nm are examined for the correlation with Chl, for which the best correlation (highest R^2) produces the best NRDI. The best λ1 and λ2 determined in this step will be used as the numerator in RRDI. Second step, all possible band combinations of λ3 and λ4 are examined for the correlation with Chl, for which the best correlation produces the best RRDI.

2.5 *PLS Model*

The PLS method is an efficient tool for multivariate modeling and is increasingly used for handling high dimensional hyperspectral data (Richter et al. 2012). The PLS regression reduces the data dimension by extracting the latent variables (factors) as new predictors and regress the response variables on these factors. Compared to multiple linear regression, the PLS regression has the desirable property that solves the problem of strong co-linearity (Atzberger et al. 2010). Therefore, PLS was also used to estimate Chl in this study. PLS has the advantage that the precision of the model improves with the increasing number of variables and observations (Wold et al. 2001). To optimize the number of factors (latent variables), leave-one-out cross validation was used to test the significance of the increase in the predicted residual sum of squares (PRESS) (van der Voet 1994).

3 Results

3.1 *NRDI Optimization*

Fig. 1A shows the lambda-by-lambda R^2 plot for the correlations between NRDIs and Chl. The highest R^2 values were obtained by the red edge bands paired with NIR bands.

Fig. 1B shows the best NRDI (highest R^2) with λ1 and λ2 at 745 nm and 740 nm, respectively. This NRDI accounted for 70% of the variation in Chl with an RMSE of 4.8 µg/cm² (Fig. 1B).

3.2 *Red Edge Position*

The red edge position (λ_{RE}) was determined as the maximum of the first derivative of the reflectance. Fig. 2 shows that λ_{RE} ranged from 700 nm to 740 nm and yielded significant difference only when N rate was higher than 105 kg/ha.

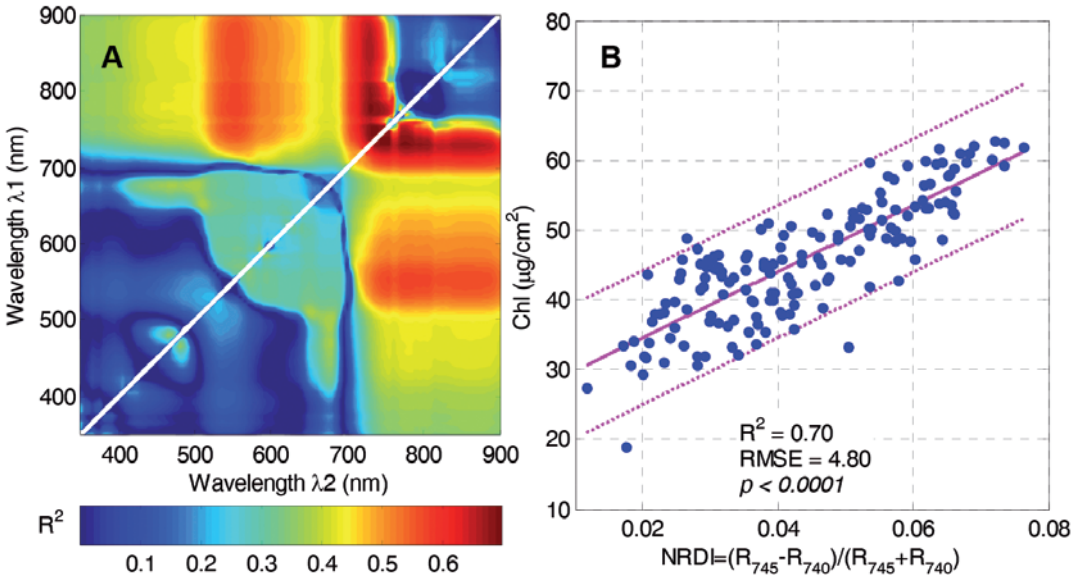

Fig. 1: A: Lambda-by-lambda R^2 plot showing the performance of different band combinations of λ1 and λ2 for the optimization of NRDI. B: Scatter plot showing the relationship between Chl and the best 2-band combination of λ1 and λ2 derived from Fig. 1A.

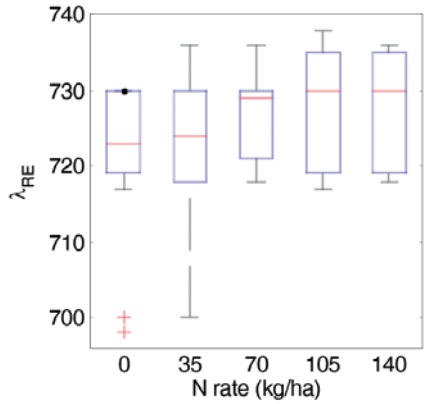

Fig. 2: Boxplot showing the changes in red edge position (λ_{RE}) between different N rates.

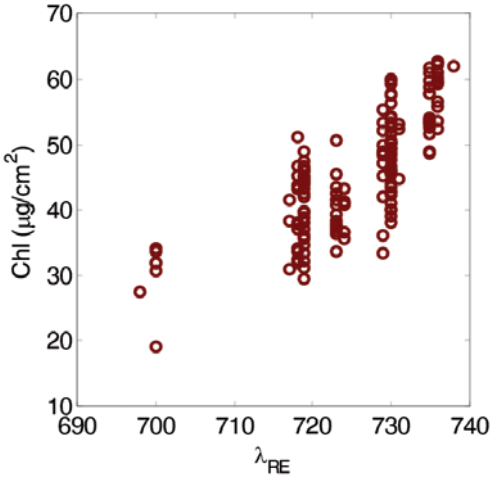

Fig. 3: Leaf chlorophyll content (Chl, µg/cm^2) plotted as a function of the red edge position (λ_{RE}).

The N rates of 105 kg/ha and 140 kg/ha produced a λ_{RE} shift to longer wavelengths and yielded higher values of λ_{RE} compared to the low-N rates.

To investigate the response of λ_{RE} to Chl variations, Chl was plotted as a function of λ_{RE}. Fig. 3 shows that λ_{RE} was positively related to Chl. The highest value of λ_{RE}, ca. 740 nm, corresponded to the highest Chl content that was 65 µg/cm^2 approximately.

3.3 *RRDI Optimization*

Fig. 4 shows the lambda-by-lambda R^2 plot for the correlations between RRDIs and Chl. Results indicate that RRDI greatly increased the sensitivity to Chl across the whole wavelength range compared to NRDI (Fig. 1A).

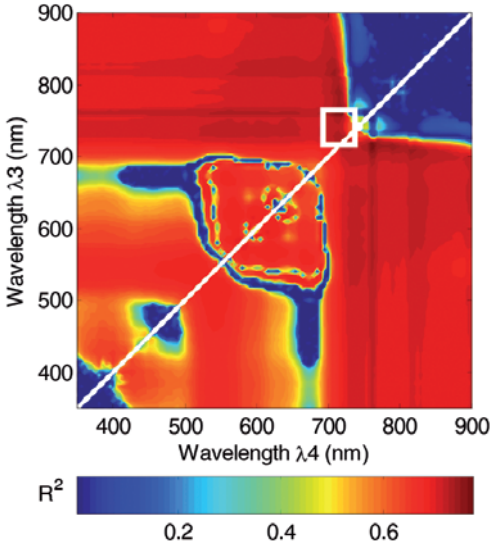

Fig. 4: Lambda-by-lambda R^2 plot showing the performance of different band combinations of λ3 vs. λ4 for the RRDI. White rectangle highlights the red edge range of 700 nm – 740 nm.

One of the significantly hot zones for λ3 vs. λ4 locates in the wavelengths of 700 nm – 740 nm, which agrees well with the range of λ_{RE} (Figs. 2 and 3). Therefore, the λ3 vs. λ4 were optimized within the range of 700 nm – 740 nm and, they were finally determined as 740 nm and 700 nm based on the highest R^2, respectively, for the best RRDI.

The best RRDI = $(R_{745} - R_{740})/(R_{740} - R_{700})$ accounted for 72% of the variation in Chl with an RMSE of 4.59 µg/cm^2 (Tab. 1).

Exp. 2 dataset was used to test the reliability of the best NRDI and RRDI for the estimation of Chl. Results show that NRDI and RRDI accounted for 60% and 62% of the variation in Chl, respectively, with an RMSE of 4.77 µg/cm^2 and 4.63 µg/cm^2 (Tab. 1: Results of R2 and RMSE (µg/cm2) for different datasets using NRDI = (R745 – R740)/(R745 + R740), RRDI = (R745 – R740)/(R740 – R700) and the PLS model).

3.4 *Chl Estimation for Farmer Fields*

Regression models based on RRDI and NRDI were calibrated using the pooled data of the

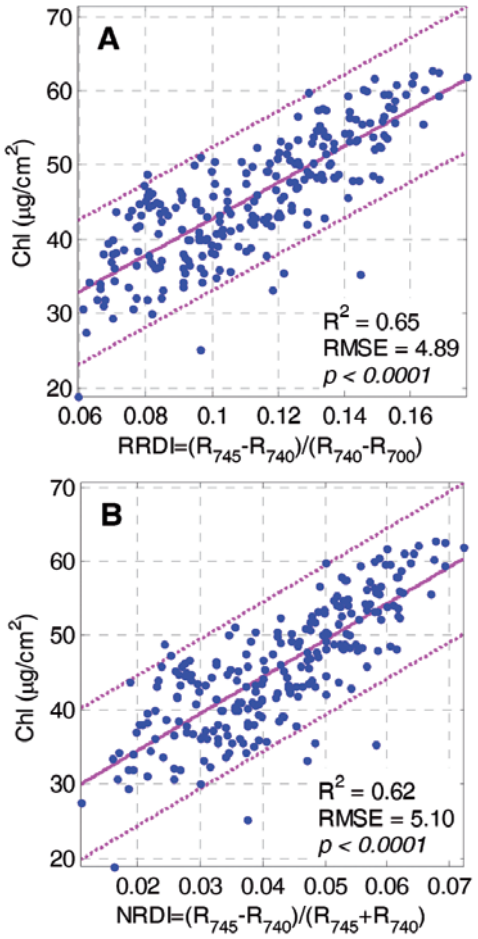

Fig. 5: (A) RRDI model based on the pooled experimental data (Exp. 1 + 2). (B) NRDI model based on the pooled data.

two experiments and were applied to farmer fields for the estimation of Chl.

Fig. 5 shows the calibration results for RRDI and NRDI. RRDI and NRDI accounted for 65% and 62% of the variation in Chl of pooled data (Exp.1 + 2), respectively.

Tab. 1 summarizes both the calibration and validation results for farmer fields. The R^2 for the predicted Chl by RRDI and NRDI against the measured Chl were 0.49 and 0.45, respectively, with an RMSE of 5.47 µg/cm² and 5.68 µg/cm² (Fig. 6A–B and Tab. 1).

3.5 *Chl Estimation for Farmer Fields Using PLS model*

The PLS model was also calibrated using the pooled data of two experiments. Results showed that PLS model accounted for 85% of the variation in Chl (Tab. 1) with an RMSE of 3.22 µg/cm².

The calibrated PLS model was further used to estimate the Chl of farmer fields. Fig. 6C shows that R^2 for the predicted Chl by PLS against the measured Chl was 0.55 with an RMSE of 5.13 µg/cm².

The PLS model accounted for a larger portion of the variation in Chl of both experimental and farmer fields and yielded a lower RMSE compared to the univariate regression models based on NRDI and RRDI (Tab. 1 and Fig. 6).

Tab. 1: Results of R^2 and RMSE (µg/cm²) for different datasets using NRDI = $(R_{745} - R_{740})/(R_{745} + R_{740})$, RRDI = $(R_{745} - R_{740})/(R_{740} - R_{700})$ and the PLS model.

Dataset	Description	*n*	NRDI		RRDI		PLS	
			R^2	RMSE	R^2	RMSE	R^2	RMSE
Exp. 1	Optimize Indices	160	0.70	4.80	0.72	4.59		
Exp. 2	Test Indices	80	0.60	4.77	0.62	4.63		
Exp. 1 + 2	Model Calibration	240	0.62	5.10	0.65	4.89	0.85	3.22
Farmer fields	Model Validation	70	0.45	5.68	0.49	5.47	0.55	5.13

n, number of observations

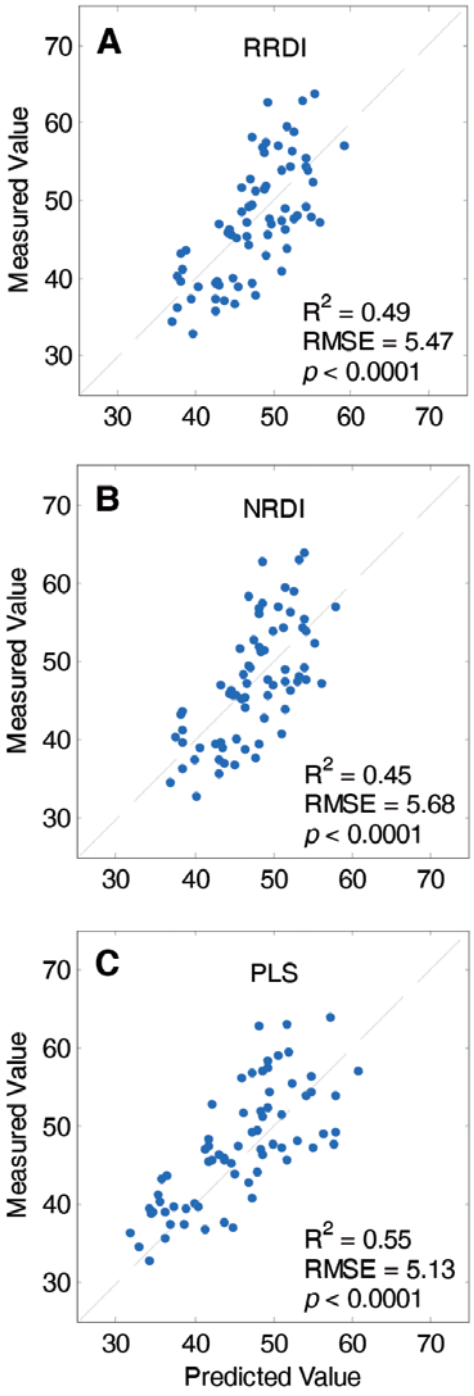

Fig. 6: Scatter plots showing the measured by predicted values of Chl using (A) RRDI, (B) NRDI and (C) PLS models calibrated on the pooled data of two experiments (Exp. 1 + 2). Dashed line is the 1:1 line.

4 Discussion

The lambda-by-lambda band optimization method has been used to optimize NDVI- and SR-like indices for the estimation of canopy characteristics in different species (Darvishzadeh et al. 2008, Darvishzadeh et al. 2009, Yu et al. 2012, Yu et al. 2013). However, the potential of linking red edge characteristics to the optimization of NDVI- or SR-like indices have not been fully explored. As shown in the lambda-by-lambda R^2 plots, the RRDI optimization increases the sensitivity over the entire wavelengths compared to NRDI (Figs. 1 and 4). In addition to the significant zone at red edge range, the range for NIR vs. red edge, e.g. 760 nm – 820 nm vs. 720 nm) also showed the best performance. However, the NIR range is governed primarily by LAI (Darvishzadeh et al. 2008), thus the red edge might be more appropriate for Chl estimation.

The best RRDI= $(R_{745} - R_{740})/(R_{740} - R_{700})$ could be considered as the ratio of derivative of reflectance at 740 nm, i.e. $d\lambda_{740} = (\lambda_{745} - \lambda_{740})/5)$ and the relative change in the red edge positions. Similarly, Lee et al. (2008) found that the derivative of reflectance at 735 nm could be used to estimate rice N. Soil background is one of the main factors that affect the hyperspectral remote sensing of leaf chlorophyll. Darvishzadeh et al. (2008) optimized the SAVI2 type indices to estimate Chl and found that it yielded equivalent accuracy in terms of RMSE compared to narrow band NDVI, i.e., NRDI in this study. However, the optimization of SAVI2 type indices requires the soil-line coefficients, which are difficult to determine for this study due to the flooding environment of rice field. Our results suggest that RRDI seems to be able to reduce to some extent the effects of soil, water background and phenological development compared to NRDI.

Spectral indices are not able to represent all spectral variability because they often employ a limiting number of bands. Also, the simple regression models based on spectral indices are easy to be over-fitted to the limiting observations. In contrast, PLS takes into account how the response variables co-vary with the explanatory variables, and it is particularly relevant in the situation where modeling data

consist of many predictors, i.e., hyperspectral narrow bands, relative to the number of observations (Wold et al. 2001, Yu et al. 2014). As expected, PLS outperformed both the optimized NRDI and RRDI and resulted in lower RMSE. Both NRDI and RRDI showed an underestimation of high Chl values compared to the PLS model (Fig. 6). This corroborates the suggestion to use PLS for the full spectrum analysis (Atzberger et al. 2003). However, the determination of sensitive bands and optimization of spectral indices might be useful as an early indicator of plant physiological status and potential stresses before a more precisely quantitative approach made by full spectrum analysis.

Considering that spectral indices are characterized by simplicity and are compatible for different sensors with different resolutions or bands, the optimization of spectral indices still has practical value for applications of remote sensing in agriculture. Robust spectral indices will also contribute to the development of end-user-friendly crop sensors. Better development and validation of more complex, but more reliable, indices could be also achieved by integrating more rigorous cross-validation or bootstrap techniques (Richter et al. 2012).

5 Conclusions

The red edge plays a crucial role in estimating chlorophyll (Chl). This stresses the high potential of the red edge bands for the optimization of spectral indices. Two indices based on red edge: the normalized reflectance difference index (NRDI = $(R_{745} - R_{740})/(R_{745} + R_{700})$) and the ratio of reflectance difference index (RRDI = $(R_{745} - R_{740})/(R_{740} - R_{700})$) are robust indicators of leaf Chl content of rice ($R^2 = 0.60 - 0.72$, RMSE = 4.59 µg/cm² – 5.1 µg/cm²) according to experimental data. They showed acceptable performance for mapping the Chl variation in agricultural fields, yielding an RMSE of 5.68 µg/cm² and 5.47 µg/cm², respectively, although the partial least squares (PLS) model delivered higher accuracy (RMSE = 5.13 µg/cm²). The results show the potential of mapping canopy biochemical traits through the optimization of spectral indices and other feature reduction techniques such as PLS.

Acknowledgements

This study was supported by the China 973 Program (Grant No. 2009CB118606), the innovative group grant of the Natural Science Foundation of China (NSFC Grant No. 31121062), German Federal Ministry of Education & Research (BMBF, Grant No. CHN 08/051), the China Scholarship Council (CSC, No. 2009635098) and the GSGS grant (No. GSGS-2014-F01) of the Graduate School of Geosciences (University of Cologne). We thank Y. Yao, S. Huang, X. Li, E. Dornauf, and J. Weskamm for data collection, colleagues of Qixing and Keyansuo experimental stations for field management, and X. Yu and J. Ma for allowing the measurement in their fields.

References

Atzberger, C., Jarmer, T., Schlerf, M., Kötz, B. & Werner, W., 2003: Spectroradiometric determination of wheat bio-physical variables. Comparison of different empirical-statistical approaches. – Goossens, R. (ed.): Remote Sensing in Transitions. – 23rd EARSeL Symposium 2003: 463–470, Belgium.

Atzberger, C., Guérif, M., Baret, F. & Werner, W., 2010: Comparative analysis of three chemometric techniques for the spectroradiometric assessment of canopy chlorophyll content in winter wheat. – Computers and Electronics in Agriculture **73** (2): 165–173, DOI: 10.1016/j.compag.2010.05.006.

Atzberger, C., 2013: Advances in Remote Sensing of Agriculture: Context Description, Existing Operational Monitoring Systems and Major Information Needs. – Remote Sensing **5** (2): 949–981, DOI: 10.3390/rs5020949.

Darvishzadeh, R., Skidmore, A., Schlerf, M., Atzberger, C., Corsi, F. & Cho, M., 2008: LAI and chlorophyll estimation for a heterogeneous grassland using hyperspectral measurements. – ISPRS Journal of Photogrammetry and Remote Sensing **63** (4): 409–426, DOI: 10.1016/j.isprsjprs.2008.01.001.

Darvishzadeh, R., Atzberger, C., Skidmore, A.K. & Abkar, A.A., 2009: Leaf Area Index deriva-

tion from hyperspectral vegetation indices and the red edge position. – International Journal of Remote Sensing **30** (23): 6199–6218, DOI: 10.1080/01431160902842342.

Delalieux, S., Auwerkerken, A., Verstraeten, W., Somers, B., Valcke, R., Lhermitte, S., Keulemans, J. & Coppin, P., 2009: Hyperspectral reflectance and fluorescence imaging to detect scab induced stress in apple leaves. – Remote Sensing **1** (4): 858–874, DOI: 10.3390/rs1040858.

Filella, I. & Peñuelas, J., 1994: The red edge position and shape as indicators of plant chlorophyll content, biomass and hydric status. – International Journal of Remote Sensing **15** (7): 1459–1470, DOI: 10.1080/01431169408954177.

Gnyp, M.L., Yu, K., Aasen, H., Yao, Y., Huang, S., Miao, Y. & Bareth, G., 2013: Analysis of Crop Reflectance for Estimating Biomass in Rice Canopies at Different Phenological Stages. – PFG – Photogrammetrie, Fernerkundung, Geoinformation **2013** (4): 351–365, DOI: 10.1127/1432-8364/2013/0182.

Gnyp, M.L., Miao, Y., Yuan, F., Ustin, S.L., Yu, K., Yao, Y., Huang, S. & Bareth, G., 2014: Hyperspectral canopy sensing of paddy rice aboveground biomass at different growth stages. – Field Crops Research **155:** 42–55, DOI: 10.1016/j.fcr.2013.09.023.

Horler, D.N.H., Dockray, M. & Barber, J., 1983: The red edge of plant leaf reflectance. – International Journal of Remote Sensing **4** (2): 273–288, DOI: 10.1080/01431168308948546.

Koppe, W., Gnyp, M.L., Hennig, S.D., Li, F., Miao, Y., Chen, X., Jia, L. & Bareth, G., 2012: Multi-Temporal Hyperspectral and Radar Remote Sensing for Estimating Winter Wheat Biomass in the North China Plain. – PFG – Photogrammetrie, Fernerkundung, Geoinformation **2012** (3): 281–298, DOI: 10.1127/1432-8364/2012/0117.

Laudien, R., Buercky, K., Doluschitz, R. & Bareth, G., 2006: Establishment of a Web-based spectral database for the analysis of hyperspectral data from *Rhizoctonia solani*-inoculated sugarbeets. – Zuckerindustrie **131** (3): 164–170.

Laudien, R. & Bareth, G., 2006: Multitemporal hyperspectral data analysis for regional detection of plant diseases by using a tractor-and an airborne-based spectrometer. – PFG – Photogrammetrie, Fernerkundung, Geoinformation **2006** (3): 217–227.

Lee, Y., Yang, C., Chang, K. & Shen, Y., 2008: A simple spectral index using reflectance of 735 nm to assess nitrogen status of rice canopy. – Agronomy Journal **100** (1): 205–212, DOI: 10.2134/agronj2007.0018.

Main, R., Cho, M.A., Mathieu, R., O'Kennedy, M.M., Ramoelo, A. & Koch, S., 2011: An investigation into robust spectral indices for leaf chlorophyll estimation. – ISPRS Journal of Photogrammetry and Remote Sensing **66** (6): 751–761, DOI: 10.1016/j.isprsjprs.2011.08.001.

Markwell, J., Osterman, J.C. & Mitchell, J.L., 1995: Calibration of the Minolta SPAD-502 leaf chlorophyll meter. – Photosynthesis Research **46** (3): 467–472, DOI: 10.1007/BF00032301.

Mulla, D.J., 2013: Twenty five years of remote sensing in precision agriculture: Key advances and remaining knowledge gaps. – Biosystems Engineering **114** (4): 358–371, DOI: 10.1016/j.biosystemseng.2012.08.009.

Richter, K., Atzberger, C., Hank, T.B. & Mauser, W., 2012: Derivation of biophysical variables from Earth observation data: validation and statistical measures. – Journal of Applied Remote Sensing **6** (1): 063557-1–063557-23, DOI: 10.1117/1.JRS.6.063557.

van der Voet, H., 1994: Comparing the predictive accuracy of models using a simple randomization test. – Chemometrics and Intelligent Laboratory Systems **25** (2): 313–323, DOI: 10.1016/0169-7439(94)85050-X.

Wold, S., Sjöström, M. & Eriksson, L., 2001: PLS-regression: a basic tool of chemometrics. – Chemometrics and Intelligent Laboratory Systems **58** (2): 109–130, DOI: 10.1016/S0169-7439(01)00155-1.

Yao, Y., Miao, Y., Huang, S., Gao, L., Ma, X., Zhao, G., Jiang, R., Chen, X., Zhang, F., Yu, K., Gnyp, M., Bareth, G., Liu, C., Zhao, L., Yang, W. & Zhu, H., 2012: Active canopy sensor-based precision N management strategy for rice. – Agronomy for Sustainable Development **32** (4): 925–933, DOI: 10.1007/s13593-012-0094-9.

Yu, K., Lenz-Wiedemann, V., Leufen, G., Hunsche, M., Noga, G., Chen, X. & Bareth, G., 2012: Assessing hyperspectral vegetation indices for estimating leaf chlorophyll concentration of summer barley. – ISPRS Annals of the Photogrammetry, Remote Sensing and Spatial Information Sciences **I-7:** 89–94, DOI: 10.5194/isprsannals-I-7-89-2012.

Yu, K., Li, F., Gnyp, M.L., Miao, Y., Bareth, G. & Chen, X., 2013: Remotely detecting canopy nitrogen concentration and uptake of paddy rice in the Northeast China Plain. – ISPRS Journal of Photogrammetry and Remote Sensing **78:** 102-115, DOI: 10.1016/j.isprsjprs.2013.01.008.

Yu, K., Leufen, G., Hunsche, M., Noga, G., Chen, X. & Bareth, G., 2014: Investigation of leaf diseases and estimation of chlorophyll concentration in seven barley varieties using fluorescence and hyperspectral indices. Remote Sensing **6** (1): 64–86, DOI: 10.3390/rs6010064.

Zarco-Tejada, P.J., Miller, J.R., Noland, T.L., Mohammed, G.H. & Sampson, P.H., 2001: Scaling-up and model inversion methods with narrowband optical indices for chlorophyll content estimation in closed forest canopies with hyperspectral data. – IEEE Transactions on Geoscience and Remote Sensing **39** (7): 1491–1507, DOI: 10.1109/36.934080.

Zarco-Tejada, P.J., Miller, J.R., Mohammed, G.H., Noland, T.L. & Sampson, P.H., 2002: Vegetation stress detection through chlorophyll a+b estimation and fluorescence effects on hyperspectral imagery. – Journal of environmental Quality **31** (5): 1433–1441, DOI: 10.2134/jeq2002.1433.

Addresses of the Authors:

Kang Yu, Martin Leon Gnyp, Prof. Dr. Georg Bareth, International Center for Agro-Informatics & Sustainable Development (www.icasd.org), Institute of Geography, GIS & RS Group, University of Cologne, D-50923 Köln, Tel.: +49-221-470-6551, Fax: +49-221-470-1638, e-mails: {kyu}{mgnyp1}{g.bareth}@uni-koeln.de

Lei Gao, Prof. Dr. Yuxin Miao, Prof. Dr. Xinping Chen, International Center for Agro-Informatics & Sustainable Development, Center for Resources, Environment & Food Security, College of Resources and Environmental Sciences, China Agricultural University, 100094 Beijing, Tel.: +86-10-62732865, Fax: +86-10-62731016, e-mails: jaypin@gmail.com, {ymiao}{chenxp}@cau.edu.cn

Manuskript eingereicht: November 2013
Angenommen: Juli 2014

PFG 2015 / 1, 0055–0067
Stuttgart, February 2015

Article

Comparison of two Statistical Methods for the Derivation of the Fraction of Absorbed Photosynthetic Active Radiation for Cotton

Sylvia Lex, Sarah Asam, Fabian Löw & Christopher Conrad, Würzburg

Keywords: FAPAR, agriculture, RapidEye, NDVI, empirical regression, percentile approach

Summary: The fraction of absorbed photosynthetic active radiation (FAPAR) is an important input for modelling biomass increase and agricultural yield and can be calculated based on optical remote sensing data. In this study two remote sensing based approaches to derive the FAPAR for irrigated cotton in Fergana valley, Uzbekistan, are tested and compared: (i) FAPAR rescale from the normalized difference vegetation index (NDVI) ("percentile approach"), and (ii) an empirical regression approach based on NDVI. In the rescaling approach FAPAR was derived by relating upper and lower percentiles derived from the NDVI distribution of cotton fields from the entire study area to fixed FAPAR minima (bare soil) and maxima. NDVI was derived from multi-temporal 6.5 m RapidEye data acquired throughout 2011. For the regression approach FAPAR data was collected *in situ* from cotton fields during the vegetation season. The percentile approach delivered an RMSE of 0.10 whilst regression was only slightly better with an RMSE of 0.07. Hence, the percentile approach could be concluded as being a fast and easy alternative to field data demanding empirical regressions for the derivation of FAPAR on cotton fields.

Zusammenfassung: *Vergleich zweier statistischer Methoden zur Ableitung des Anteils absorbierter Photosynthese wirksamer Strahlung (FAPAR) für Baumwolle.* Der Anteil absorbierter photosynthesewirksamer Strahlung (FAPAR), welcher ein wichtiger Inputparameter für die Modellierung von Biomassezuwachs und Ernteerträgen ist, kann aus optischen Fernerkundungsdaten abgeleitet werden. In dieser Studie werden zwei verschiedene, fernerkundungsbasierte Verfahren zur Ableitung von FAPAR für Baumwollfelder miteinander verglichen: (i) die direkte Ableitung von FAPAR durch Umskalierung des Normalized Difference Vegetation Index (NDVI) („Perzentil-Ansatz") und (ii) eine empirische Regression von FAPAR-Feldmessungen mit dem NDVI. Bei der Umskalierung werden obere und untere Grenzwerte der NDVI-Verteilung (Perzentile) in Beziehung zu FAPAR Minimum und Maximum-Werten gesetzt. Die erforderlichen Geländedaten wurden während der Vegetationsperiode 2011 im Ferghanatal in Usbekistan aufgenommen. Der NDVI wurde aus multi-temporalen RapidEye-Daten desselben Jahres berechnet. Die direkte Ableitung von FAPAR resultiert in einem RMSE von 0.10, während mit der empirischen Regression nur ein leicht besseres Ergebnis (RMSE = 0.07) erzielt werden kann. Die Ergebnisse lassen auf eine gute Eignung des vergleichsweise einfachen Perzentil-Ansatzes als Alternative zu messdatenintensiven Methoden zur Bestimmung von FAPAR auf Baumwollfeldern schließen.

1 Introduction

Biophysical parameters like the fraction of absorbed photosynthetic active radiation (FAPAR) are important vegetation parameters for environmental monitoring. The FAPAR characterizes the potential of vegetation to absorb energy (Myneni et al. 1997) and is defined as the fraction of radiation that is absorbed by the vegetation canopy in the visible

 www.schweizerbart.de
DOI: 10.1127/pfg/2015/0250 1432-8364/15/0250 $ 3.50

light (400 nm – 700 nm) for photosynthesis (Monteith 1972). Due to these properties, multi-temporal FAPAR can be used for modelling biomass accumulation and yield in agriculture (Delécolle et al. 1992).

Radiative transfer models (RTM) can achieve very high accuracies when modelling FAPAR but require numerous sensor- and site-specific input data such as illumination and viewing geometries, leaf structure, chlorophyll content or dry matter content (Jacquemoud et al. 2009). On the basis of RTM, a near-linear relationship between FAPAR and remotely sensed vegetation indices (VIs) was found (Choudhury 1987, Goward & Huemmrich 1992) which was the fundament for statistical FAPAR modelling.

The relation between VIs and FAPAR has been investigated for different biomes from in situ measurements to the scale of moderate resolution sensors. Linear regressions of in situ FAPAR and normalized difference VI (NDVI) measurements were found for grassland and agriculture in West Africa by Fensholt et al. (2004). Cristiano et al. (2010) systematically compared numerous VIs with FAPAR measurements of two different grass types in Argentina within the vegetation season and found green NDVI, NDVI and the optimized soil adjusted VI to be the best statistical estimators for FAPAR. Logarithmic correlations modestly outperformed linear correlations. Differences in plant architecture of the grass types or plant stress situations influenced the slope of the statistical relation between the VIs and FAPAR only negligibly. Increasing stress in turn negatively affected the strength of the correlation results. Investigations of the statistical relation between FAPAR and VIs derived from satellite data revealed a significant influence of vegetation cover fractions on FAPAR (Asrar et al. 1992). Others pointed at the necessity to carefully select the appropriate VI in order to avoid impact of the soil background colour, or to minimize errors for different vegetation classes (e.g. Choudhury 1987, Sellers et al. 1994, 1996).

In the light of the almost linear relationship between FAPAR and VIs, Sellers et al. (1994, 1996) proposed a straight forward method for global FAPAR retrieval independent from in situ data, based on Advanced Very High Resolution Radiometer (AVHRR) data. Percentiles from occurring NDVI values indicate the range of possible FAPAR values, e.g. in case of numerous vegetation classes, 98% and 5% NDVI refer to FAPAR values of 0.95 and 0.001, respectively (Sellers et al. 1996). NDVI-percentiles were calculated for each class separately. In this global approach, the NDVI percentiles were extracted from all available AVHRR pixel values of one vegetation class after correcting for varying illumination angles caused by different geographical latitudes (Sellers et al. 1994, 1996). As Sellers et al. (1992) empirically found a near-linearity between the FAPAR and simple ratio (SR: ratio between near infrared and red reflectance), Sellers et al. (1994) used SR for calculating FAPAR between the extreme values (percentiles) in the original formulation of their approach. However, the authors were aware that other VIs may better suit for some vegetation classes and soil types, as for instance shown by Choudhury (1987) who selected the NDVI for deriving FAPAR of crops on bright soils. Examples for the implementation of NDVI instead of SR in a percentile approach are given by Olofsson & Eklundh (2007) and Olofsson et al. (2007). The authors utilized Moderate Resolution Imaging Spectroradiometer (MODIS) NDVI for FAPAR modelling on forested sites in Sweden and Denmark.

Only few studies transferred the approach of Sellers et al. (1996) to high resolution data. Lobell et al. (2003) compared several combinations of VIs for wheat in agricultural areas of Mexico based on multi-temporal 30 m Landsat data (TM and ETM+). They tested (i) SR and (ii) NDVI using the percentile approach. With the resulting FAPAR from (i) and (ii) they calculated the mean FAPAR of both approaches (iii). Yield was calculated and the best results, i.e. mostly matching regional yield statistics, were obtained by averaging the estimates of the FAPAR from SR and NDVI.

This study targets at the application of the approach of Sellers et al. (1994, 1996) to multi-temporal high spatial resolution RapidEye data of 2011 for deriving the FAPAR in cotton ecosystems of Fergana Valley in Uzbekistan. In this region, area-wide approaches for mapping vegetation parameters without or using minimum field data appear to be useful

for land and water management, because information on crop growth and crop yields is rare. The percentile approach was employed in three different experiments using literature values and satellite data derived soil background values for calculating the FAPAR range for the VI percentiles (NDVI and SR). The results were compared with simple linear regression results between field measurements of the FAPAR and NDVI. The NDVI was selected because it was identified as the best performing VI for the FAPAR derivation via linear regression in a pre-study conducted in the same study region (Lex et al. 2013). The testplots were located on two farms with different cotton cultivation practises.

2 Study Area

The study area Fergana valley is located in the eastern part of Uzbekistan in the upstream part of the Syr Darja River. The climate is dry with a mean precipitation ranging from 100 mm to 500 mm and a mean temperature of 13.1 °C (Abdullaev et al. 2009). It is one of the largest and most intensively used agricultural areas in Uzbekistan where one third of the country's population lives (Reddy et al. 2012). Main crops in this region are winter-wheat, cotton, rice, and orchards. Vegetables like water-melons and tomatoes are also planted (Conrad et al. 2013). As the evaporation rate is about 1,200 mm per year, which exceeds precipitation by far, irrigation of the agricultural fields is necessary (Reddy et al. 2013).

Two locations in the Fergana valley were selected as study sites: The Water User Association (WUA) "Akbarabad" and the WUA "Azizbek" (see Fig. 1). In Akbarabad, cotton is sown at a row distance of 60 cm while in Azizbek farmers planted in 90 cm distance. Sowing date for cotton in both study sites was in the first half of April in 2011. Harvesting took place between the end of September and middle of October. All fields are characterized by similar soils which are loamy with an average content of sand between 40 and 50%, a silt content of 50 to 60% and a small clay fraction between 0 and 20% (Kenjabaev et al. 2013).

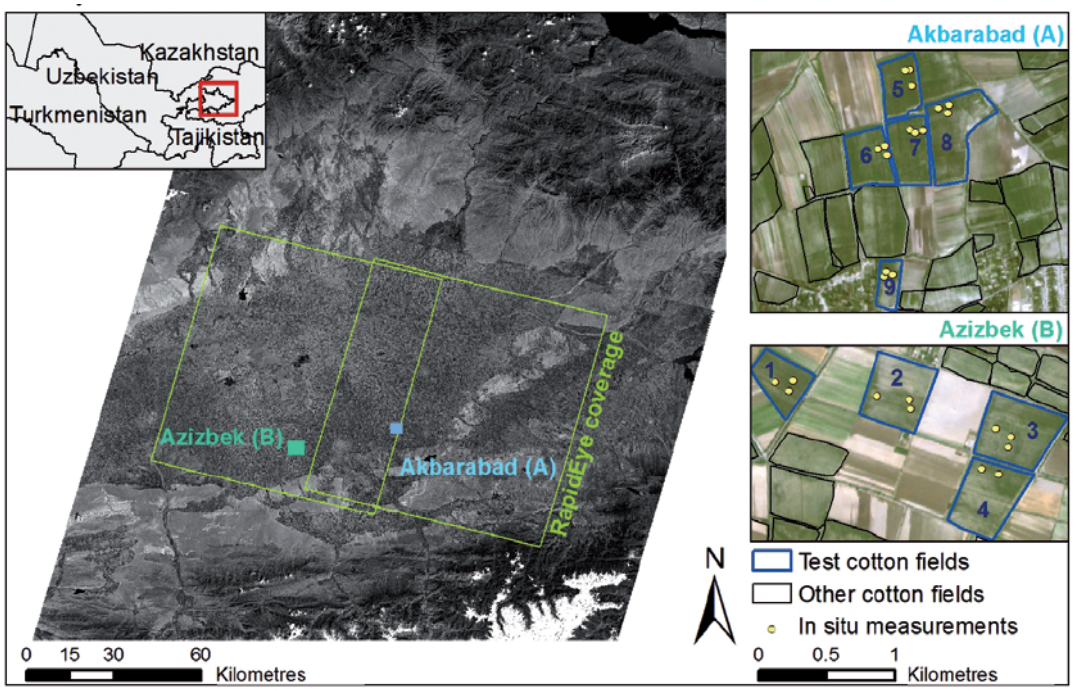

Fig. 1: The two study sites are located in the Fergana valley, Uzbekistan: Akbarabad (A) and Azizbek (B). RapidEye data, shown in the maps on the right, is from 29.7.2011 and displayed as true colour composite. Blue lines indicate the boundaries of test cotton fields and the *in situ* measurements are presented with yellow dots. The background map consists of two Landsat – TM images (only red band) from 3.6.2011 (southern part) and 22.8.2011 (northern part).

3 Data and Methods

3.1 *Field Campaign*

In total, nine cotton fields were selected within the two study sites in the south-eastern part of the valley (see Fig. 1). Four fields were located in the WUA "Azizbek" (study site B: Fields 1, 2, 3, 4) and five in the WUA "Akbarabad" (Study site A: Fields 5, 6, 7, 8, 9). The FAPAR ground truth data was collected between the beginning of June and the end of September 2011. On each field three environmental sampling units (ESUs) were established with each ESU consisting of twelve field points. Only on field 4 two ESUs were measured. An ESU describes a comparatively homogeneous area with a size of 20 m × 20 m. The twelve field points should integrate the within ESU variability of the field measurements. It has to be noted that in the later analysis, segments of RapidEye data were analysed, which completely covered the ESU. The total number of field points was 312 (26 ESUs with twelve field points each). Each field point was visited six times during the season (Tab. 1).

At each field point the FAPAR was measured using the Ceptometer AccuPAR LP-80 (Decagon Devices 2013). It is equipped with an 80 cm long bar with 80 equally distributed sensors enabling measurements of the photosynthetic active radiation (PAR) above and beneath the canopy. The average plant height was measured with a folding metre stick.

3.2 *Pre-Processing of Satellite Data*

RapidEye data (Tyc et al. 2005) was acquired throughout the measurement campaign (Tab. 1). In order to cover both study sites, two different RapidEye paths were analysed (Fig. 1). Each scene was atmospherically corrected using ATCOR2 (Richter & Schlaepfer 2012) within the processing chain CATENA that was developed at the German Aerospace Center (DLR) (DLR 2014). Geometric correction was done with the software ERDAS Autosync-Module (ERDAS 2010) with a resulting RMSE of below 2.2 m as described in Lex et al. (2013).

In situ data was not compared to pixel values but to a homogeneous surrounding of the field points. This step should account for both, uncertainties between the geolocation of in situ and satellite data, which may lead for incorrect sample pairs of in situ FAPAR and RapidEye NDVI, and the scale difference between 6.5 m RapidEye pixels and the ESUs. To cope with the prescribed uncertainty the data was segmented using the software eCognition (Trimble Germany GmbH 2010) as proposed by Fritsch et al. (2012). Therefore, a relatively small scale parameter (10) and the parameters shape and compactness (set to 0.9 each) were used. By doing so, a sub-segmentation of the cotton fields was achieved. For every available RapidEye acquisition, NDVI was calculated and spatially averaged within these sub-segments of the cotton fields.

Tab. 1: Acquisition timing of RapidEye data and corresponding field sampling campaigns (adapted from Lex et al. 2013)

Site A (Akbarabad)			Site B (Azizbek)		
RapidEye Acquisition	Beginning of fieldwork	End of fieldwork	RapidEye acquisition	Beginning of fieldwork	End of fieldwork
07.06.2011	08.06.2011	15.06.2011	15.06.2011	14.06.2011	16.06.2011
24.06.2011	24.06.2011	28.06.2011	23.06.2011	25.06.2011	29.06.2011
23.07.2011	15.07.2011	23.07.2011	07.07.2011	11.07.2011	13.07.2011
29.07.2011	30.07.2011	01.08.2011	29.07.2011	21.07.2011	29.07.2011
07.08.2011	10.08.2011	16.08.2011	07.08.2011	12.08.2011	15.08.2011
31.08.2011	26.08.2011	05.09.2011	23.08.2011	24.08.2011	25.08.2011

3.3 *Percentile Approach*

For the derivation of the FAPAR the formula proposed by Sellers et al. (1996) was utilized in this study (1):

$$FAPAR = \frac{(VI_i - VI_{98}) * (FAPAR_{max} - FAPAR_{min})}{VI_{98} - VI_5} + FAPAR_{min} \quad (1)$$

where $FAPAR_{max}$ ($FAPAR_{min}$) refers to the maximum (minimum) possible FAPAR value of one class within the entire study area, VI_{98} (VI_5) corresponds with VI-values of the 98% (5%) percentile and VI_i is the actual VI-value at pixel i. In their global approach Sellers et al. (1996) suggested for vegetation classes that the FAPAR values of 0.950 ($FAPAR_{max}$) and 0.001 ($FAPAR_{min}$) denote the VI_{98} and VI_5, respectively.

For the RapidEye data in the Fergana Valley four variants of the original percentile approach were implemented using two different VIs and one alternative for the VI_5 percentile. First, the VIs were varied and (1) was implemented for cotton with the aforementioned propositions for the FAPAR extremes and VI percentiles. Here, simple ratio (SR, (2)) and the NDVI (3) were selected for implementing the FAPAR retrieval (SR: SEL-1, NDVI: SEL-2).

$$SR = \frac{NIR}{RED} \quad (2)$$

$$NDVI = \frac{NIR - RED}{NIR + RED} \quad (3)$$

Second, VI_5 was substituted with the VI value of bare soil. This step was based on the assumption that taking into account only satellite measurements during the vegetation period within a comparatively small geographic region will underestimate FAPAR in early crop stages. In such cases, when all satellite data show crop cover, the 5% percentile of VI data could already reflect vegetation activity and in consequence FAPAR higher than 0.001, which was set in SEL-1 and SEL-2. Therefore, one additional RapidEye acquisition from 8.4.2011 was analysed. Accordingly, SEL-3 (SEL-4) is based on SR (NDVI) from pre-season bare soil situation.

VI analysis was conducted on a segment level. The percentiles (VI_{98} and VI_5) were calculated over all scenes of the RapidEye time series between the beginning of June and the end of September. This VI-value for bare soil in SEL-3 and SEL-4 is the mean value of all pixels within all sub-segments on cotton fields (section 3.2).

3.4 *Empirical Regression Approach*

Based on the in situ FAPAR data and the NDVI mean values of the sample segments, paired for corresponding acquisition dates (see Tab. 1), a simple linear regression equation including all observations aggregated at ESU level was established (REG). NDVI was selected as VI because according to Lex et al. (2013) best empirical regression results were obtained with SAVI and NDVI. As the NDVI is used in the percentile approach of Sellers et al. (1996), in this study NDVI was chosen. To account for the fact that study sites A and B varied in their management practices (section 2) and for a better assessment of the stability of the regression parameters (slope and offset) over the area, the regression approach was also separately applied to the two study sites (REG-A, REG-B).

A regression equation can only be established if the residuals of the model fit are normally distributed (Bahrenberg et al. 2010). The Lilliefors-Test is also valid for few observations (Lilliefors 1967) and was selected in this study to test the normal distribution of the residuals.

3.5 *Validation and Comparison*

Three quantitative assessment measures were applied for validating and comparing the quality of all experiments. This comparison between the results in turn enabled the identification of the most accurate approach and the evaluation of the quality difference when using the simplified percentile approach instead of a field work intensive regression.

The root-mean-square error (RMSE, (4)) returns an average absolute deviation:

$$RMSE = \sqrt{\frac{1}{n}\sum_{i=1}^{n}\in_i^2} \quad (4),$$

where n is the number of FAPAR measurements and $\in$ is the deviation between model result and the respective *in situ* data. The mean direction of deviation is given by the BIAS (5):

$$BIAS = \frac{1}{n}\sum_{i=1}^{n}\in_i \quad (5).$$

The coefficient of determination (R^2) was employed for estimating the strength of the statistical correlation between the model output and the field measurements.

4 Results and Discussion

4.1 *Analyses of in situ Data*

The temporal development of the FAPAR varied between all cotton fields during the entire vegetation period. However, the most remarkable discrimination was found between the temporal development of the fields in the study sites A and B (Akbarabad, Azizbek). Already in time step 2 (Site A: 23.6.2011, Site B: 24.6.2011) FAPAR increases more slowly in study site B than in study site A (Akbarabad) (Fig. 2a). Later, in time steps 3 to 6 (7.7.2011/23.7.2011, 29.7.2011, 7.8.2011, and 23.8.2011/31.8.2011), the boxplots of the fields in Azizbek (B) remained on a significant lower FAPAR level than in Akbarabad (A).

Plant heights developed similar to the FAPAR within the season (Fig. 2b). Plants on the study site A were permanently higher (average of 76 cm) than those on the study site B (average of 63 cm). Both, FAPAR and plant height indicate a comparatively high vegetation cover in site A. The latter can be substantiated by taking into account the differences in cotton cultivation practises. Farmers in the study site B grow cotton with a row distance of 90 cm, whilst fields in the study site A were organized in rows with distances of 60 cm (section 2).

Varying vegetation heights within neighboured observations indicate a more heterogeneous structure of the vegetation canopy. The latter is influencing the scattering of light as described by Myneni & Williams (1994). Accordingly, the distribution of FAPAR corresponded with the deviation of plant height measurements on both observation sites. For most field observation periods, FAPAR and plant height boxes show narrow distribution between the upper and lower box boundaries in study site B. In contrast, variability of both variables was closer to the observed mean values in the study site A.

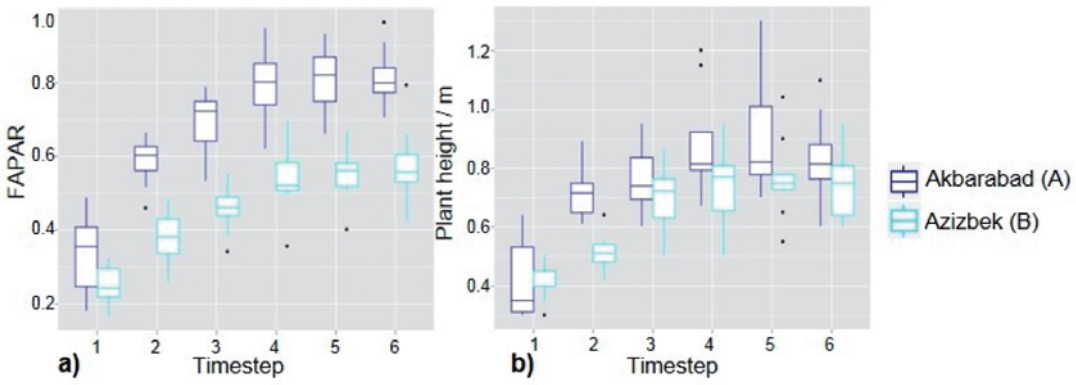

Fig. 2: a) Seasonal development of FAPAR b) development of plant heights for study sites A (Akbarabad, in blue colour) and B (Azizbek, in cyan colour); the box plots show the distribution of FAPAR and plant height values for each time step for both study sites A and B. The bar within the box is the median, the edges of the box show the interquartile range and the edges of the whiskers represent the minimum and maximum values. All values that are higher than 1.5 interquartile range are plotted as dots (FAPAR = fraction of absorbed photosynthetic active radiation).

4.2 *Percentile Approach*

Fig. 3a compares the in situ measured FAPAR with the results from the percentile approach experiments SEL-1 and SEL-2. For VI_{98} a NDVI value of 0.84 was received and VI_5 was found to be 0.14.

The FAPAR values, calculated based on SR (SEL-1), were lowest and fit the in situ data with a RMSE of 0.281 (R^2 = 0.72, BIAS = -39%, Tab. 2). SR was less sensitive to low FAPAR ranges, which led to an underestimation of in situ measurements (see blue dots in Fig. 4). The result queries the presumption of a linear relation between the SR and the FAPAR for cotton ecosystems in the study region.

The scatterplot between the FAPAR measured in situ and the FAPAR derived from the NDVI (SEL-2) shows a clear linear relation. The validation measures of SEL-2 (RMSE: 0.1, R^2: 0.87) exceeded that of SEL-1. However, the BIAS of 4.29% indicates a small overestimation of the model SEL-2 which can be assigned to high FAPAR levels (Fig. 3, red dots). These overestimations could be corrected by adjustment of the NDVI-percentiles, e.g. utilizing maximal field measurements of the FAPAR could be envisaged. The latter would go beyond the scope of this study, in which the percentile approach was tested as a variant for the FAPAR derivation without field measurements. The results of SEL-2 comply with observations of Olofsson & Eklundh (2007) who observed RMSE values between 0.03 and 0.67 using the percentile approach with NDVI for the FAPAR estimations for Scandinavian forest classes.

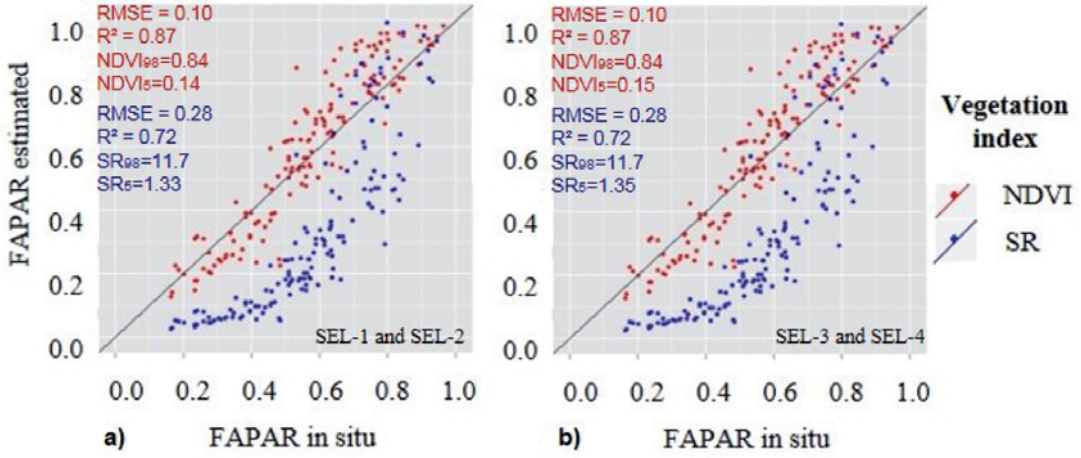

Fig. 3: a) Results of the percentile approach in contrast to the field measurements: with the SR (SEL-1, blue dots) and the NDVI (SEL-2, red dots); b) Results of the percentile approach in contrast to the field measurements: with the SR (SEL-3, blue dots) and NDVI (SEL-4, red dots).

Tab. 2: Assessment of the percentile approach (SEL-1 to SEL-4) based on BIAS, RMSE, and R^2.

Method	BIAS (in %)	RMSE	R^2	Number of observations
SEL-1	-39.646	0.281	0.7227219	148
SEL-2	4.293	0.098	0.8741476	148
SEL-3	-39.865	0.283	0.7227219	148
SEL-4	3.612	0.099	0.8741476	148
SEL-2-A*	7.954	0.116	0.8001162	86
SEL-2-B*	-3.125	0.064	0.8903632	62

*A and B refer to the respective study sites.

The experiments SEL-3 and SEL-4 returned validation measures which are almost the same as those of SEL-1 and SEL-2, respectively (Fig. 3b, Tab. 2). The lower percentile boundary (VI_5) used in SEL-1 and SEL-2 was with a NDVI value of 0.14 (SR value of 1.33) very similar to the soil VI approach (SEL-3 and SEL-4), which revealed a NDVI value of 0.15 (SR-value of 1.35) for VI_5. The VI values composing VI_5 in SEL-1 and SEL-2 originated all from the RapidEye observations in June (7.6.2011). Distinguishing between NDVI acquired in June and April (8.4.2011) led to negligible differences, which could be confirmed by visual inspection. The results show that the percentile approach can be easily applied to multi-temporal remote sensing data if sufficient NDVI values represent soil conditions. In this study, despite including only data after sowing, soil representing NDVI values were suffered due to the presence of one time step in initial growing phases. However, SEL-4 presented a feasible variant for the FAPAR derivation in case of absent early season data characterized by a very low vegetation cover.

The performance of the percentile approach was further analyzed separately for the study sites A and B. Only SEL-2 is presented as this analysis revealed the lowest absolute numerical deviation between model results and in situ measurements expressed by the RMSE (Tab. 2). SEL-4, which delivered nearly the same results as SEL-2, due to the similar value of VI_5 for SEL-2 and SEL-4, is not presented here as the resulting FAPAR was very close to that from SEL-2. The scatterplots between the FAPAR, derived by the NDVI-percentiles, and field measurements (Fig. 4) show a higher deviation from the theoretically perfect result (diagonal line) for the study site A than for the study site B. Accordingly, the RMSEs of 0.06 and 0.12 approve a slightly higher performance of the SEL-2 model in Azizbek (study site B) than in Akbarabad (study site A). These differences might be explained by the growing conditions differing between the study sites as described in section 4.1. In the study site A the cotton plants are higher than those in the study site B. A taller plant drops more shadow than a smaller plant, especially during hours that are deviating from noon, when lower sun elevation occurs. Additionally, the plant heights observed in study site A within one time step show higher variability than in study site B. As a result shadow lengths are not constant. In case of small row distances as recorded in the study site A, the shadow dropping of one cotton row might fall into the next row. Accordingly, uncertainties of the FAPAR measurements in situ, as well as the satellite derived NDVI are higher than in the study site B, which in total confirms findings of Tewolde et al. (2005). However, the high precision level of both study sites indicate the stability of the percentile approach to derive the FAPAR of cotton under different cultivation practices.

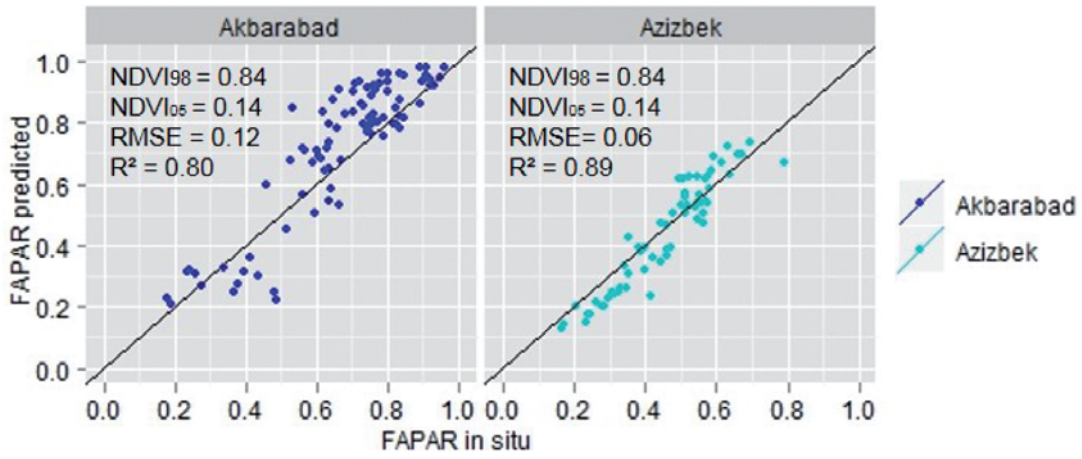

Fig. 4: Percentile approach with NDVI (SEL-2) in the study sites Akbarabad (left) and Azizbek (right).

4.3 *Simple Linear Regression*

The Lilliefors test for normal distribution of the residuals, which is the precondition for empirical regressions, delivered a p-value of 0.8753 for the regression approach applied to the entire set of field samples and NDVI values (REG). Accordingly, the hypothesis of normal distribution cannot be rejected as the p-value exceeded 0.05. Also for the separate analysis of the two study sites, the Lilliefors test showed a normal distribution of the residuals ($p = 0.5796$ for REG-A and $p = 0.2006$ for REG-B).

The statistical analysis of the entire dataset (REG) achieved an RMSE of 0.07 and R^2 of 0.87 (Tab. 3). According to the statistical nature of high correlation coefficients BIAS was negligible (<< 0.01%). Previous studies achieved similar RMSE values for FAPAR derivation using linear regression, e.g. 0.086 in an agricultural landscape in Spain based on Landsat NDVI (Ridao et al. 1998), or R^2 of 0.61 in a steppe landscape in South America modelled with MODIS NDVI (Cristiano et al. 2010) and 0.86 – 0.96 in the savannah in Senegal, also based on MODIS NDVI (Fensholt et al. 2004).

Similar statistical relations were found for the two study sites, however, the results varied slightly. The coefficient of determination for study site B (REG-B) was with a value of 0.89 higher than for study site A (REG-A), where R^2 was 0.80. Also RMSE (0.05) of REG-B, i.e. the total deviation between statistically derived FAPAR and in situ measurements was lower than of REG-A (0.08).

The same reasons as stated for the percentile approach, i.e. high variability of plant heights and a resulting inhomogeneity in site A, can explain these differences between the results among the study sites. The scattering of the value pairs from the FAPAR in situ data and the NDVI around the regression line for each study site is given in Fig. 5. The same patterns as for the percentile approach can be discovered.

In Azizbek (study site B) the FAPAR in situ data ranged from 0.17 to 0.79 while in Akbarabad (study site A) the data range was between 0.18 and 0.96. During the entire season the FAPAR-values of study site B- remained

Tab. 3: Assessment of the simple linear regression (REG, REG-A, REG-B) based on BIAS, RMSE, and R^2.

Method	BIAS (in %)	RMSE	R^2	Number of observations
REG	0.0001	0.07	0.87	148
REG-A[1)]	-0.0006	0.08	0.80	86
REG-B[1)]	-0.0001	0.05	0.89	62

1) A and B refer to the respective study sites.

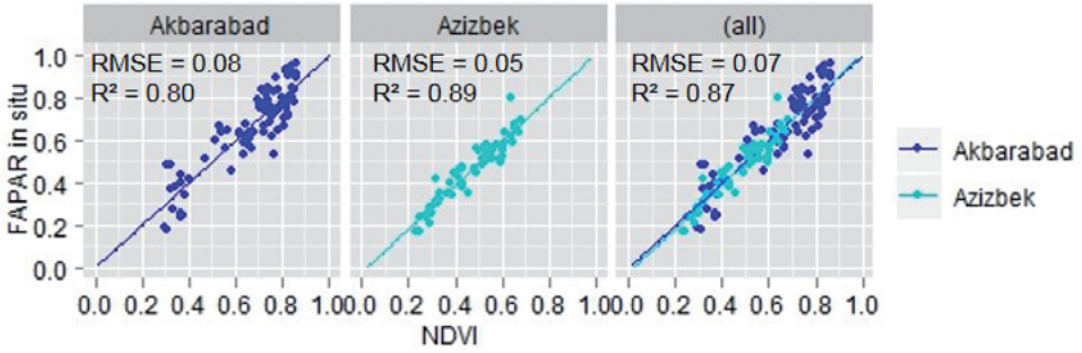

Fig. 5: Scatter plots of the in situ FAPAR and the NDVI, as well as regression lines for the study sites (Akbarabad, REG-A and Azizbek, REG-B) and both sites (REG).

Tab. 4: Regression equations (simple linear regression).

Method	Regression equations
REG	FAPAR = -0.01300 + 1.00965 * NDVI[1)]
REG-A[2)]	FAPAR = -0.00026 + 0.99297 * NDVI
REG-B[2)]	FAPAR = -0.02145 + 1.02324 * NDVI

1) Adopted from Lex et al. (2013)
2) A and B refer to the respective study sites.

below the FAPAR-level of study site A (see Fig. 2a). Even though value ranges differed between the two study sites, similar regression equations were derived for all datasets (Tab. 4 and Fig. 5). As stated above, the management can have an influence on the crop growth. However, the similarity of the slopes received from the regression demonstrate a negligible influence of the two cultivation practices (cotton row distances) observed in this study on the quality of the linear relationship between NDVI and FAPAR.

4.4 *Comparison of the Approaches*

A comparison of RMSE and BIAS indicates only minor quantitative deviations between the optimal percentile approach SEL-2 (and SEL-4) and the simple empirical regression (REG). Of course, REG matches the dataset exactly to field data, but it is noteworthy that no field data has been used for the derivation of FAPAR in the percentile approaches. Even in SEL-4 (inclusion of a period when fields are completely free of vegetation) only satellite datasets were utilized.

Multi-temporal FAPAR maps received from SEL-2 and REG within study site B are shown in Fig. 6. In the first periods (15.6.2011 and 6.7.2011) no differences in the colour levels occurred. Moderately higher values for FAPAR derived from the percentile approach are visible in the late season situation (right part of Fig. 6, 23.8.2011), which can be attributed to the aforementioned overestimations of FAPAR in case of high vegetation cover (section 4.1). However, the comparison of the maps shows the same spatial patterns of

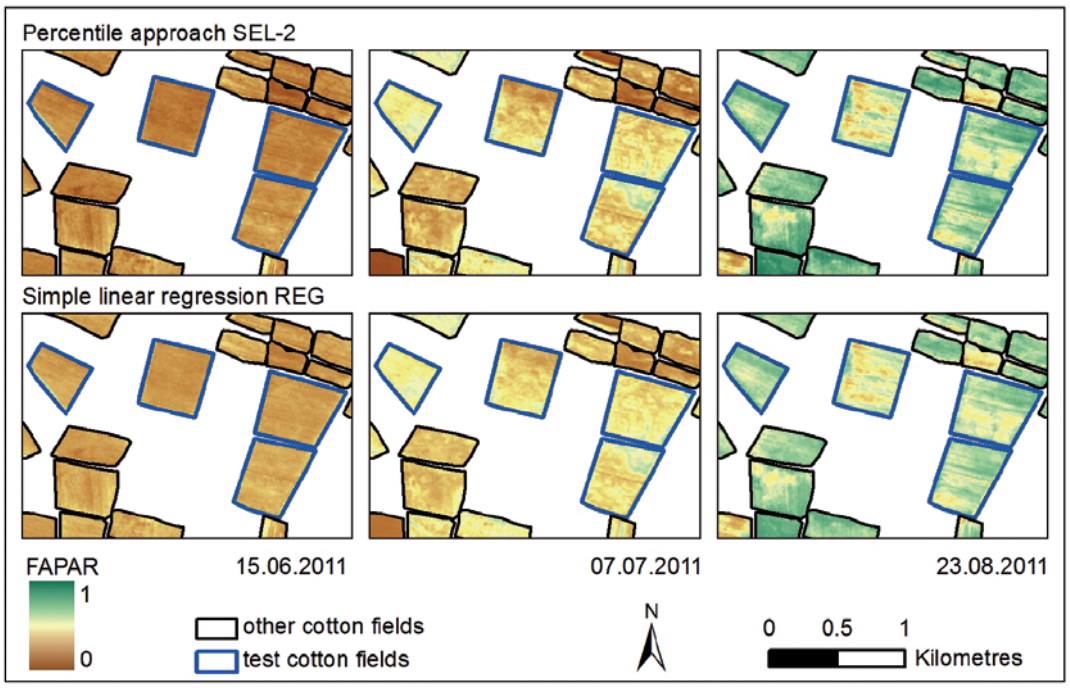

Fig. 6: FAPAR of cotton fields received from the experiments SEL-2 (upper part) and REG (lower part) in study site B, Azizbek, for the time steps 15.06.2011, 7.7.2011 and 23.8.2011, representing the early, mid, and late season situations of the vegetation period. On the fields with a blue outline *in situ* data were collected.

FAPAR variations throughout the vegetation period and underlines the similarity of the approaches.

5 Conclusions

In this study two methods for deriving the FAPAR from multi-temporal RapidEye data for cotton were compared. The study was implemented in two irrigated agricultural study sites in the Fergana Valley, Uzbekistan. As base line, an empirical regression that relates in situ FAPAR measurements to NDVI, computed from RapidEye data at six satellite image acquisitions over the growing season, was established. Furthermore, the FAPAR was calculated by linearly scaling the NDVI percentiles to maxima and minima of class-specific FAPAR values, following the approach of Sellers et al. (1996). The performances of the two methods were compared by opposing RMSE, BIAS, and the coefficient of determination revealed from correlation between the in situ FAPAR and modelled data. The maxima and minima of FAPAR, which were in the originally formulation assigned to the 98% and 5% percentile of the NDVI distribution, i.e. 0.95 and 0.001, were transferred to the cotton class at the local scale. The application of the percentile approach, which is without field measurements, resulted in accuracies comparable to that of the linear regression, also on a similar accuracy level received from empirical experiments in other agro-ecosystems: The percentile approach delivered an RMSE of 0.10 whilst regression was only slightly better with an RMSE of 0.07. This demonstrated that the FAPAR of cotton fields could be derived independently from field measurements by applying the percentile approach. Differences in canopy diversity introduced by variable plant heights within the field or distances between the rows did not show a significant impact, neither on the empirical regression nor on the percentile approach.

However, generalized statements about the usefulness of the percentile approach for FAPAR estimations of cotton ecosystems are not easy to conclude. A wide range of NDVI values was available, because the entire vegetation period was covered by satellite data. RapidEye scenes were acquired in both the initial and the main vegetative phase of the vegetation period, when quasi non-vegetated soil cover and most dense vegetation cover was measured by the NDVI, respectively. Another issue to be considered is that this study was conducted in the Fergana Valley, hence conclusions from this study might not necessarily apply to other cotton ecosystems e.g. with other climatic conditions or environmental or management settings (soils, field sizes, cultivation practises). Thus, the presented study has a more explorative character in terms of transferability but it can be concluded as an encouraging approach for accurate FAPAR modelling without in situ data, which can be subsequently used for crop yield estimations of cotton.

Acknowledgements

The authors thank the foundation “fiat panis” for financing the field campaign and the German Aerospace Center (DLR) for providing data from the RapidEye Science Archive in RESA project 461. This study was partly conducted within the project CAWa (“Water for Central Asia”, FKZ AA7090002), financed by the German Foreign Office, and the project Techs4TimeS (FKZ 50EE1353), funded by the German Federal Ministry for Economic Affairs and Energy. The authors are grateful for the support of the Scientific Information Center of the Interstate Coordination Water Commission of the Central Asia (SIC ICWC) in Tashkent, Uzbekistan during the field campaign.

References

Abdullaev, I., Kazbekov, J., Manthritilake, H. & Jumaboev, K., 2009: Participatory water management at the main canal: A case from South Ferghana canal in Uzbekistan. – Agricultural Water Management **96** (2): 317–329.

Asrar, G., Myneni, R.B. & Choudhury, B.J., 1992: Spatial Heterogeneity in Vegetation Canopies and Remote Sensing of Absorbed Photosynthetically Active Radiation: A Modeling Study. – Remote Sensing of Environment **41** (2–3): 85–103.

Bahrenberg, G., Giese, E., Mevenkamp, N. & Nipper, J. (eds.), 2010: Statistische Methoden in der Geographie. – Univariate und bivariate Statistik. – 282 pp., Borntrager, Stuttgart.

Choudhury, B.J., 1987: Relationships Between Vegetation Indices, Radiation Absorption, and Net Photosynthesis Evaluated by a Sensitivity Analysis. – Remote Sensing of Environment **22** (2): 209–233.

Conrad, C., Rahmann, M., Machwitz, M., Stulina, G., Paeth, H. & Dech, S., 2013: Satellite based calculation of spatially distributed crop water requirements for cotton and wheat cultivation in Fergana Valley, Uzbekistan. – Global and Planetary Change **110:** 88–98.

Cristiano, P.M., Posse, G., Di Bella, C.M. & Jaimes, F.R., 2010: Uncertainties in FPAR estimation of grass canopies under different stress situations and differences in architecture. – International Journal of Remote Sensing **31** (15): 4095–4109.

Decagon Devices, 2013: AccuPAR PAR/LAI Ceptometer. – Model LP-80, 82, Decagon Devices Inc., Pullman, Washington DC, USA.

Delécolle, R., Maas, S.J., Guérif, M. & Baret, F., 1992: Remote sensing and crop production models: present trends. – ISPRS Journal of Photogrammetry and Remote Sensing **47** (2–3): 145–161.

DLR, 2014: http://www.dlr.de/eoc/desktopdefault.aspx/tabid-5444/9113_read-17838/ (21.3.2014).

ERDAS, 2010: IMAGINE AutoSync. – ERDAS Inc., Atlanta, GA, USA.

Fensholt, R., Sandholt, I. & Rasmussen, M.S., 2004: Evaluation of MODIS LAI, fAPAR and the relation between fAPAR and NDVI in a semi-arid environment using *in situ* measurements. – Remote Sensing of Environment **91** (3–4): 490–507.

Fritsch, S., Machwitz, M., Ehammer, A., Conrad, C. & Dech, S., 2012: Validation of the collection 5 MODIS FPAR product in a heterogeneous agricultural landscape in arid Uzbekistan using multitemporal RapidEye imagery. – International Journal of Remote Sensing **33** (21): 6818–6837.

Goward, S.N. & Huemmrich, K.F., 1992: Vegetation Canopy PAR Absorptance and the Normalized Difference Vegetation Index: An Assessment Using the SAIL Model. – Remote Sensing of Environment **39** (2): 119–140.

Jacquemoud, S., Verhoef, W., Baret, F., Bacour, C., Zarco-Tejada, P.J., Asner, G.P., François, C. & Ustin, S.L., 2009: PROSPECT+SAIL models: A review of use for vegetation characterization. – Remote Sensing of Environment **113:** 56.

Kenjabaev, S., Forkutsa, I., Bach, M. & Frede, H.G., 2013: Performance evaluation of the BUDGET model in simulating cotton and wheat yield and soil moisture in Fergana valley. – Ahmed, M.N. & Pawlowski, I. (eds.): International Conference and Young Researchers' Forum: 'Natural resource use in Central Asia: institutional challenges and the contribution of capacity building', Giessen.

Lex, S., Conrad, C. & Schorcht, G., 2013: Analyzing the seasonal relations between in situ fPAR / LAI of cotton and spectral information of RapidEye. – Borg, E., Daedelow, H. & Johnson, R. (eds.): From the Basics to the Service. – GITO, Berlin.

Lilliefors, H.W., 1967: On the Kolmogorov-Smirnov Test for Normality with Mean and Variance Unknown. – Journal of the American Statistical Association **62** (318): 399–402.

Lobell, D.B., Asner, G.P., Ortiz-Monasterio, J. & Benning, T.L., 2003: Remote sensing of regional crop production in the Yaqui Valley, Mexico: estimates and uncertainties. – Agriculture, Ecosystems & Environment **94** (2): 205–220.

Monteith, J.L., 1972: Solar Radiation and Productivity in Tropical Ecosystems. – Journal of Applied Ecology **9** (3): 747–766.

Myneni, R.B. & Williams, D.L., 1994: On the relationship between FAPAR and NDVI. – Remote Sensing of Environment **49** (3): 200–211.

Myneni, R.B., Nemani, R., Ramakrishna, R. & Running, S.W., 1997: Estimation of Global Leaf Area Index and Absorbed Par Using Radiative Transfer Models. – IEEE Transactions on Geoscience and Remote Sensing **35** (6): 1380–1393.

Olofsson, P. & Eklundh, L., 2007: Estimation of absorbed PAR across Scandinavia from satellite measurements. Part II: Modeling and evaluating the fractional absorption. – Remote Sensing of Environment **110** (2): 240–251.

Olofsson, P., Eklundh, L., Lagergren, F., Jönsson, P. & Lindroth, A., 2007: Estimating net primary production for Scandinavian forests using data from Terra/MODIS. – Advances in Space Research. **39** (1): 125–130.

Reddy, J.M., Muhammedjanov, S., Jumaboev, K. & Eshmuratov, D., 2012: Analysis of cotton water productivity in Fergana Valley of Central Asia. – Agricultural Sciences **3** (6): 822–834.

Reddy, J.M., Jumaboev, K., Matyakubov, B. & Eshmuratov, D., 2013: Evaluation of furrow irrigation practices in Fergana Valley of Uzbekistan. – Agricultural Water Management **117:** 133–144.

Richter, R. & Schlaepfer, D., 2012: Atmospheric / Topographic Correction for Satellite Image-

ry. – ATCOR-2/3 User Guide, Version 8.2 BETA, February 2012.

Ridao, E., Conde, J.R. & Mínguez, M., 1998: Estimating fAPAR from Nine Vegetation Indices for Irrigated and Nonirrigated Faba Bean and Semileafless Pea Canopies. – Remote Sensing of Environment **66** (1): 87–100.

Sellers, P.J., Berry, J.A., Collatz, G.J., Field, C.B. & Hall, F.G., 1992: Canopy Reflectance, Photosynthesis, and Transpiration. III. A Reanalysis Using Improved Leaf Models and a New Canopy Integration Scheme. – Remote Sensing of Environment **42** (3): 187–216.

Sellers, P.J., Tucker, C.J., Collatz, G.J., Los, S.O., Justice, C.O., Dazlich, D.A. & Randall, D., 1994: A global 1° by 1° NDVI data set for climate studies. Part 2: The generation of global fields of terrestrial biophysical parameters from the NDVI. – International Journal of Remote Sensing **15** (17): 3519–3545.

Sellers, P.J., Los, S.O., Tucker, C.J., Justice, C.O., Dazlich, D.A., Collatz, G.J. & Randall, D., 1996: A Revised Land Surface Parameterization (SiB2) for Atmospheric GCMs. Part II: The Generation of Global Fields of Terrestrial Biophysical Parameters from Satellite Data. – Journal of Climate **9:** 706–737.

Tewolde, H., Sistani, K.R., Rowe, D.E., Adelli, A. & Tsegaye, T., 2005: Estimating cotton leaf area index nondestructively with a light sensor. – Agronomy Journal **97:** 1158–1163.

Trimble Germany GmbH, 2010: eCognition® Developer 8.64.0. – User Guide, 250, Trimble Germany GmbH, München.

Tyc, G., Tulip, J., Schulten, D., Krischke, M. & Oxfort, M., 2005: The RapidEye mission design. – Acta Astronautica **56** (1–2): 213–219.

Addresses of the Authors:

Sylvia Lex, Sarah Asam, Fabian Löw & Christopher Conrad, Department of Remote Sensing, Department of Geography and Geology, Julius-Maximilians-Universität Würzburg, Oswald-Külpe-Weg 86, D-97074 Würzburg, Germany, Tel. +49-931-31-84140, e-mail: {sylvia.lex}{sarah.asam}{fabian.loew}{christopher.conrad}@uni-wuerzburg.de, web: http://www.fernerkundung.geographie.uni-wuerzburg.de

Manuskript eingereicht: Juni 2014
Angenommen: September 2014

PFG 2015 / 1, 0069–0079
Stuttgart, February 2015

Article

Low-weight and UAV-based Hyperspectral Full-frame Cameras for Monitoring Crops: Spectral Comparison with Portable Spectroradiometer Measurements

Georg Bareth, Helge Aasen, Juliane Bendig, Köln, Martin Leon Gnyp, Dülmen, Andreas Bolten, Köln, András Jung, Leipzig, René Michels, Ulm & Jussi Soukkamäki, Oulu, Finland

Keywords: UAV, sensors, hyperspectral, change detection, agriculture, CSM, plant height, 3D, vegetation index, crops

Summary: The non-destructive monitoring of crop growth status with field-based or tractor-based multi- or hyperspectral sensors is a common practice in precision agriculture. The demand is given for flexible, easy to use, and field scale systems with super-high resolution (< 20 cm) or on single plant scale to provide knowledge on in-field variability of crop status for management purposes. Satellite- and airborne systems are usually not able to provide the spatial and temporal resolution for such purposes within a low-cost approach. The developments in the area of Unmanned Aerial Vehicles (UAV) equipped with hyperspectral sensor systems may be suited to fill that niche. In this contribution, we introduce two hyperspectral full-frame cameras weighing less than 1 kg which can be mounted to low-weight UAVs (< 3 kg). The first results of a campaign in June/July 2013 are presented and the derived spectra from the hyperspectral images are compared to related spectra collected with a portable spectroradiometer. The first results are promising.

Zusammenfassung: *Leichte und UAV-getragene hyperspektrale, bildgebende Kameras zur Beobachtung von landwirtschaftlichen Pflanzenbeständen: spektraler Vergleich mit einem tragbaren Feldspektrometer.* Die nicht-destruktive Beobachtung von Pflanzenwachstum mit feldbasierten oder traktorbasierten multi- oder hyperspektralen Sensoren ist eine gängige Praxis in der Präzisionslandwirtschaft. Um Wissen über die Variabilität des Pflanzenzustands im Feld für Managementzwecke bereitzustellen, werden flexible, multitemporal einsetzbare und einfach zu bedienende Systeme zur Erfassung ganzer Felder mit extrem hoher Auflösung (< 20 cm) oder für Einzelpflanzen benötigt. Satelliten- und flugzeuggetragene Systeme sind in der Regel nicht in der Lage, diese räumliche und zeitliche Auflösung für solche Anwendungen bereitzustellen, bzw. dies wäre mit einem nicht vertretbaren finanziellen Aufwand verbunden. Die Entwicklungen im Bereich der Unmanned Aerial Vehicles (UAV) sowie der hyperspektralen Sensortechnik scheinen genau diese Nische zu füllen. In diesem Beitrag stellen wir zwei hyperspektrale Kameras mit einem Gewicht von weniger als 1 kg vor, die mit leichten UAVs (< 3 kg) geflogen werden können. Wir präsentieren die ersten Ergebnisse einer Kampagne im Juni/Juli 2013 und vergleichen die aus den hyperspektralen Bildern abgeleiteten Spektren mit entsprechenden Spektren eines tragbaren Feldspektrometers. Die ersten Ergebnisse sind vielversprechend.

www.schweizerbart.de
DOI: 10.1127/pfg/2015/0256 1432-8364/15/0256 $ 3.00

1 Introduction

In Precision Agriculture (PreAg), sensor-based monitoring of crops to derive plant growth parameters and yield are in the focus of research to support proper crop management (Mulla 2013). Therefore, the applications of remote and proximal sensing methods are key technologies in PreAg (Oerke et al. 2010). Besides monitoring crops, sensing technologies are also widely used for measuring soil and environmental parameters (Whelan & Taylor 2013). Hyperspectral remote and proximal sensing is intensively investigated for the detection of crop nitrogen (N) content, biomass, yield and crop stress (Koppe et al. 2012, Li et al. 2010, Oerke et al. 2010, Thenkabail et al. 2000, Yu et al. 2013). In general, the remote sensing approaches described in the literature are satellite- or airborne (manned airplanes). For proximal sensing approaches, portable field spectrometer are used for canopy or leaf-level sensing (Gnyp et al. 2014, Yu et al. 2013). In the last years, efforts have been undertaken to make hyperspectral data more frequently available and sensing methods for a specific crop growth stage were investigated (Aasen et al. 2014, Gnyp et al. 2013). The latter is a precondition for monitoring plant growth behaviour by multi-temporal campaigns during phenology which enables the detection of abiotic and biotic stresses (Laudien & Bareth 2006, Laudien et al. 2006).

For the consideration of specific phenological stages in non-destructive sensing approaches, a very flexible platform is needed. Usually, satellite- or airborne sensors cannot provide such multitemporal data within a fixed time slot of a few days (Zhang & Kovacs 2012). Besides the demand for high temporal resolution in crop monitoring approaches, a high spatial resolution is in the focus of PreAg resulting in increased knowledge on within-field variability of crop growth. Unmanned aerial vehicles (UAVs) also known as unmanned aerial systems (UAS) or remotely-piloted aerial systems (RPAS) are remote sensing platforms combining very high flexibility in temporal scale and very high resolution in spatial scale (Zhang & Kovacs 2012). The potential of UAV-based imaging in agricultural applications is already well described by Zhang & Kovacs (2012), Calderón et al. (2013), Zarco-Tejada et al. (2012) and others.

The fast technological progress and developments are not only found for UAV platforms, but also for sensor development (Bareth et al. 2011, Bendig & Bareth 2014). Electronic devices were continuously minimized in the last years which resulted in low-weight sensors being very capable for the integration in small remote sensing platforms (Colomina & Molina 2014). Hence, in 2013 two new hyperspectral, full-frame imaging spectrometers were introduced, the Cubert UHD185 "Firefly" (www.cubert-gmbh.de) and the Rikola hyperspectral camera (www.rikola.fi), and in 2014 the BaySpec OCI-1000 (www.bayspec.com). All three low-weight (< 1 kg) cameras cover the spectral VIS/NIR domain but use different technologies. The Rikola and the Cubert sensors were flown in a first campaign in June/July 2013. The objectives of this contribution are (i) to introduce the two hyperspectral frame cameras, which document a new milestone in hyperspectral imaging spectroscopy, and (ii) to compare spectra from the images acquired by UAV-campaigns on barley field experiments with spectra measured with the fieldspectroradiometer FieldSpec3 by ASDI (www.asdi.com).

2 Study Area, UAV, and Sensors

The field experiment is located on the research farm of Bonn University, called Campus Klein-Altendorf, which is outside of the city of Bonn in Rheinbach. The field campaigns were carried out within the Crop.Sense.net project's activity, coordinated by the Institute of Crop Science and Resource Conservation of Bonn University (www.cropsense.de). Crop.Sense.net is one of the BMBF Networks of Excellence in Agricultural and Nutrition Research, which are funded by the German Ministry for Education and Research (BMBF) and by the European Union Funds for regional development. In Klein-Altendorf, the central field experiments of Crop.Sense.net for barley and sugar beet have been conducted. For this study, multi-temporal UAV campaigns were flown over barley in 2013. The experiment covers 36 plots (each 3 by 7 m) with 18 barley

varieties and two nitrogen treatments (40 and 80 kg/ha). For this first spectral comparison and evaluation, only selected plots (plot numbers 41, 42, and 43) are investigated.

For the UAV campaigns, a HiSystems MK Oktokopter was flown which is a low-cost (< 2000 €) and low-weight UAV (< 1.5 kg). The latter is an important fact due to the aviation regulations in Germany which allow commercial and non-commercial imaging campaigns with UAVs weighing less than 5 kg. The MK Oktokopter has a payload of up to 1 kg and a flight endurance of approximately 15 min. It can be auto-piloted by using waypoints. The UAV platform is described in detail by Bendig et al. (2013). Two hyperspectral full-frame cameras were mounted to the UAV and were flown separately after each other over the same experimental fields. In Fig. 1 (top), the MK Oktokopter is shown before take-off with the mounted Rikola hyperspectral camera (RHC), which is based on Piezo-Actuated Fabry-Perot Interferometer (FPI) (Mäkeläinen et al. 2013). FPI enables tuneable wavelength settings resulting in a time lag for each wavelength (Mäkeläinen et al. 2013). The wavelength is produced by a tuneable air gap (vacuum) between two optical layers (Honkavaara et al. 2013). Therefore, the spectral wavelength is a function of the size of the air gap. The tuning of the air gap results in an individual image acquisition for each spectral band with a CMOSIS CMOS image sensor recording 1 megapixel (Mäkeläinen et al. 2013). The RHC covers the spectral region between 400 nm to 950 nm. Before take-off, the RHC can be calibrated against a white reference panel. The images are saved onboard on a SD card.

Fig. 1: Top: MK Oktokopter is prepared for a flight campaign with the Rikola hyperspectral camera, middle: Cubert UHD185 Firefly is calibrated against a white panel before take-off, bottom: UHD185 in the air mounted on a MK Oktokopter.

The Cubert UHD185 Firefly is designed and developed by the Institute of Laser Technologies in Medicine and Metrology at the University of Ulm and the Cubert GmbH, Germany. The camera records hyperspectral full-frames with 137 bands in a spectral range of 450 nm – 950 nm. A silicon CCD chip captures an image with 1000 by 970 grayscale pixels as well as 50 by 50 hyperspectral pixels. At a flying altitude of 30 m the grayscale image has a ground resolution of about 1 cm and a pure hyperspectral ground resolution of about 20 cm. However, the latter may be pan-sharpened by the software of the manufacturer to the resolution of the grayscale image. The footprint of each scene at 30 m sensor to canopy distance is about 10.3 m. In Fig. 1 (bottom), the UAV-mounted UHD185 is shown. As the RHC, the UHD185 may be calibrated against a white reference panel (Fig. 1, middle). The typical integration time to capture a full hyperspectral data cube is 1 ms (clear sky). The UHD185

has to be flown with a mini-computer (MC) which records the data. Additionally, the MC runs the server application by which the camera can be remotely controlled via WiFi.

The two cameras are differently remote controlled during flight with an UAV. While the measurement of the RHD is controlled by an initialization file which has to be created before the flight, the UHD185 is controlled by the mini-pc with a server application, which may be configured and controlled through WiFi. Depending on the user's needs one of the systems might be beneficial. Additionally, both interfaces are currently still under development and thus, will not be further presented here.

For ground truth data collection, destructive samplings of biomass, plant N- and chlorophyll content, and non-destructive samplings of plant height, hyperspectral, and fluorescence data were performed. Those samplings were continuously carried out during phenology. Canopy reflectance was measured in the barley experiment in 2013 with an ASDI FieldSpec3 Pro (Analytical Spectral Devices, Inc., Boulder, CO, USA). The FieldSpec3 (FS3) measures the reflectance between 350 nm and 2500 nm with a sampling interval of 1.4 nm in the visible near infrared (VNIR) domain and with 2 nm in the shortwave infrared (SWIR) spectral region. The reflectance was measured at a height of 0.5 m above canopy without a fore optic resulting in a 25° field of view to minimize the background signals of soil (Fig. 2). FieldSpec3 campaigns were conducted between 11 am and 2 pm local mean time around solar noon. A condition for the measurements is a mostly cloudless sky. A white spectralon panel was used for continuous calibrations. The same reference panel was also used for the RHC and UHD185 calibration (compare Fig. 1, middle). For each plot, a total of six to eight FieldSpec3 spectra were randomly taken to represent a mean plot reflectance.

Fig. 2: Sampling hyperspectral ground truth with an ASD FieldSpec3.

3 Spectral Comparisons

The first UAV campaigns with the UHD185 and the RHC were carried out on June 14th, 2013 (Fig. 3). Both hyperspectral frame imagers operated successfully in the air after mounting them to the MK Oktokopter. To compare the spectral results for both camera systems with the FS3 spectra, images were taken at 30 m above ground level covering a maximum of three plots per image. The spatial resolution is as stated above.

Directly after the UAV-based image acquisition the hyperspectral field measurements were taken. For each plot, ten measurements of the FS3 were averaged at six to eight positions (Fig. 4). The measurements were taken from the core of the plots to exclude border effects. The spectra were than averaged to represent the plot's mean reflectance. In Fig. 3, a false colour image of the UHD185 data is dis-

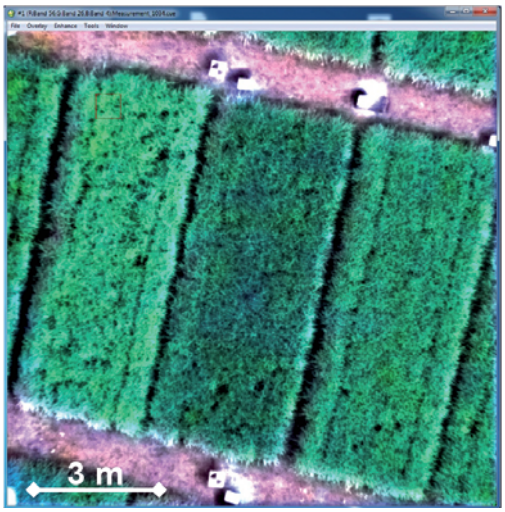

Fig. 3: RGB image with the UHD185 covering three barley plots (3 by 7 m each), June 14th, 2013.

played. The potential locations of the six FS3 measurements are shown in Fig. 4.

For retrieving the mean plot spectra of the hyperspectral images, polygons with an inner buffer of 0.3 m were digitized to reduce border effects. Spatial statistics were computed for all pixels within a plot polygon to derive mean spectra. In Fig. 5, the polygons are visualized for the three plots, each covering approximately 130,000 pixels of the UHD185 hyperspectral image.

While the polygons in Fig. 5 represent the true area for calculating the spatial statistics, the circles of the single hyperspectral field measurements shown in Fig. 4 do not represent the true location. The latter were captured as shown in Fig. 2 but the locations were randomly selected excluding areas of destructive biomass sampling.

The mean spectra from the UHD185 image shown in Fig. 5 and the corresponding mean spectra from FS3 are plotted in Fig. 6. The

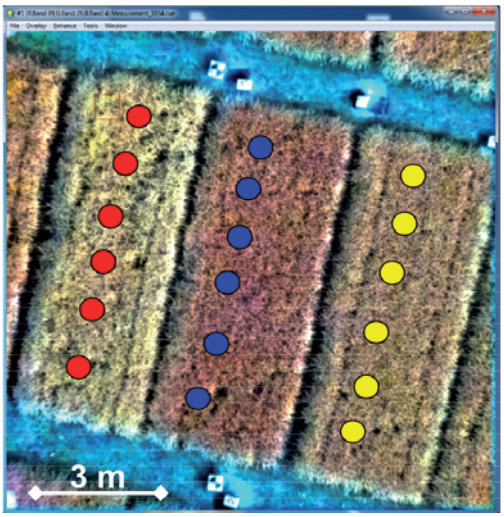

Fig. 4: Six randomized FieldSpec3 spectra were taken for each plot on June 14th, 2013.

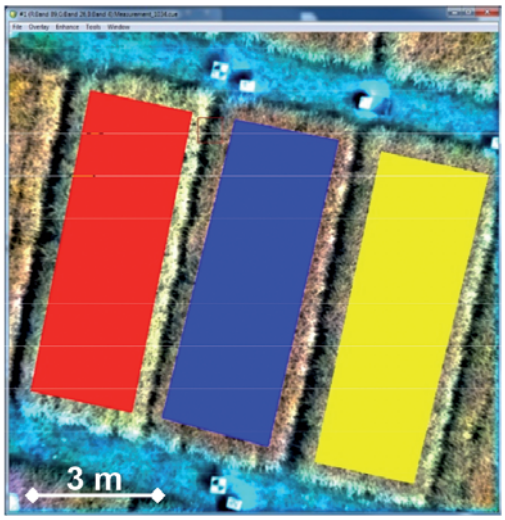

Fig. 5: Digitized polygons to calculate spatial statistics for each plot from UHD185 hyperspectral image for June 14th, 2013.

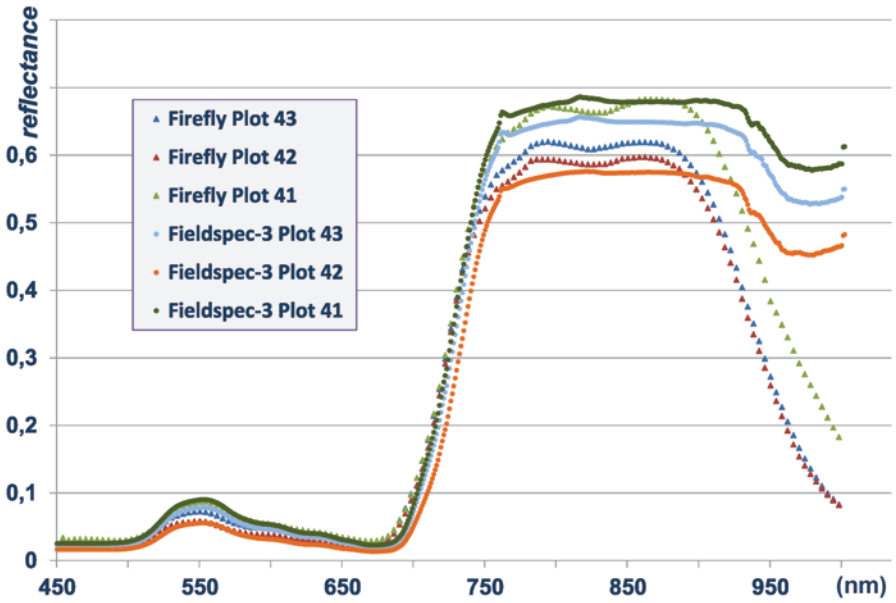

Fig. 6: FieldSpec3 spectra vs UHD185 spectra for plots 41, 42, and 43 on June 14th 2013.

lines with the denser dotted points represent the FS3 data with higher spectral resolution compared to the UHD185 data with a lower spectral resolution. The magnitude of reflectance is similar and corresponds well. However, in the NIR, differences in the shape of the spectra are visible. Additionally, a decline of reflection in the UHD185 spectra is obvious for wavelengths longer than 900 nm.

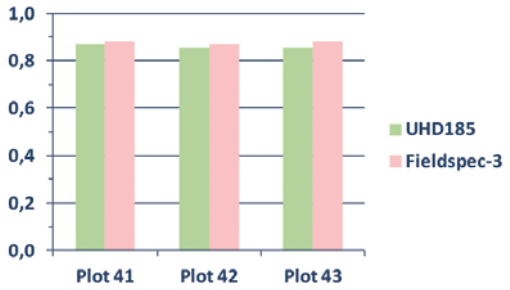

Fig. 7: OSAVI for the investigated plots from FieldSpec3 and UHD185 spectra for June 14th, 2013.

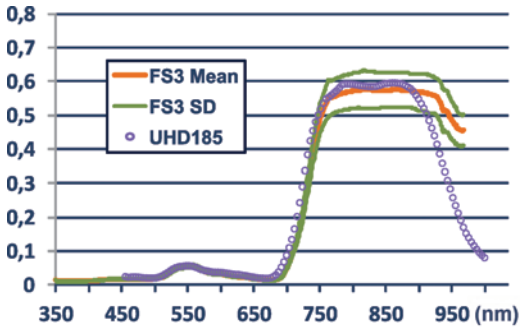

Fig. 8: Mean FieldSpec3 spectrum for plot 42 with standard deviation (SD) and mean UHD185 spectrum for June 14th, 2013.

To get an impression of the usability of the sensors for vegetation indices (VIs) two common vegetation indices, the optimized soil-adjusted vegetation index (OSAVI) and the normalized difference vegetation index (NDVI), were calculated for the FS3 and UHD185. NDVI is widely used in remote sensing while OSAVI reduces the soil background signals (Rondeaux et al. 1996) The first impression of similar spectral pattern and magnitude are confirmed for NDVI-like VIs. The OSAVI from FS3 data and UHD185 spectra are shown in Fig. 7 for the investigated plots. They do not show a significant difference having UHD185/FS3 OSAVI values of 0.87/0.88, 0.86/0.87, and 0.85/0.88 for plots 41, 42, and 42, respectively. Similar results were produced for NDVI calculations (Fig. 11).

Additionally, the differences in the spectra between the two sensors are partly within the standard deviation (SD) of the FS3 measurements. As an example, the FS3 spectrum with the SD for plot 42 is displayed in Fig. 8. When compared to the UHD185 spectra, it is visible that in the NIR region the instruments are within SD. The latter is not true for the red

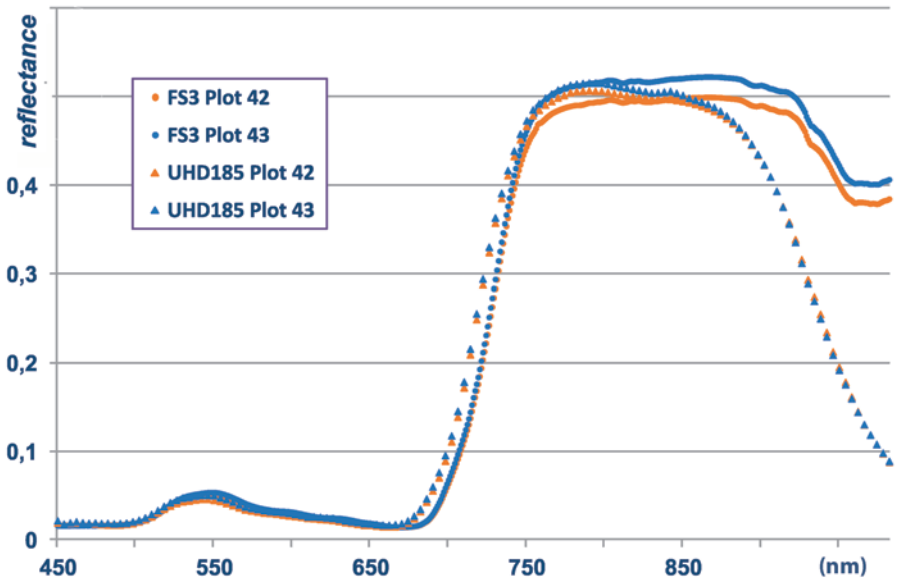

Fig. 9: FieldSpec3 and UHD185 spectra for plots 42 and 43 on June 19th, 2013.

edge domain and the wavelengths longer than 900 nm. A small spectral shift to the shorter wavelength is observable resulting in large differences when calculating simple ratio VIs from bands in the VIS spectral region.

Similar spectral properties can be described for the UAV campaign with the UHD185 on June 19th, 2013 (Fig. 9). In general, lower spectral magnitudes can be observed for plots 42 and 43 in the NIR domain with both sensors while magnitude and overall pattern of the UHD185 fit to the FieldSpec3 measurements. Plot 41 was not investigated due to insufficient coverage. Additionally, the aforementioned shift of the UHD185 occurs again in the red edge domain towards shorter wavelength and the performance from 900 nm onwards is poor.

Finally, very different spectral patterns occur on July 8th, 2013 (Fig. 10). It is clearly visible that the FS3 spectra show a very different NIR pattern due to beginning of senescence. This decrease in reflectance between 750 nm and 800 nm is not captured by the UHD185. Additionally, the spectra show higher differences in the VIS domain while the overall magnitudes are still comparable but much weaker than before. The spectral shift towards shorter wavelength is again a characteristic for the red edge spectral regions and for the poor performance above 900 nm.

The Rikola hyperspectral camera (RHC) operates on a different technology, using a Piezo-Actuated Fabry-Perot interferometer (FPI). In moving sensor platforms, a spatial shift of each spectral band might be the consequence and must be solved by image matching techniques. As described above, the RHC enables imaging of selected wavelengths. According to well described VIs (Gnyp et al. 2013, Laudien et al. 2006, Li et al. 2010, Yu et al. 2013), we chose eight wavelengths for the UAV campaign on June 14th, 2013: 505 nm, 552 nm, 604 nm, 674 nm, 741 nm, 745 nm, 770 nm, and 803 nm. To calculate VIs from the RHC image we used the same polygon as for the image of the UHD185 (Fig. 5).

The NDVI values calculated from the RHC (Fig. 11) are lower than for the UHD185 and

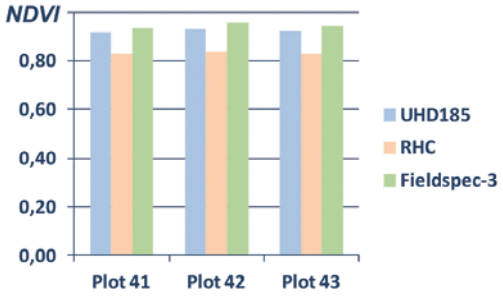

Fig. 11: Calculated NDVI for the investigated plots for June 14th, 2013.

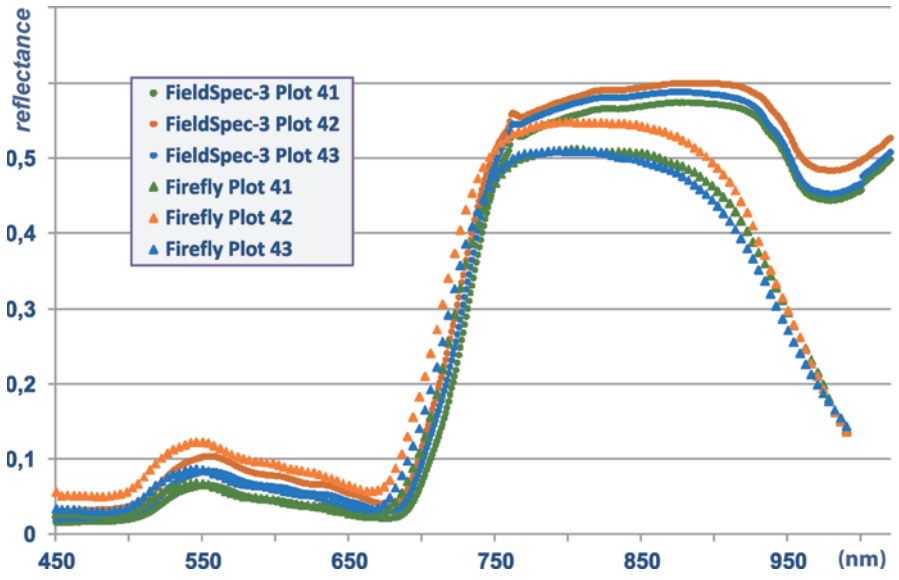

Fig. 10: FieldSpec3 spectra vs. UHD185 spectra for plots 41, 42, and 43 on July 8th, 2013.

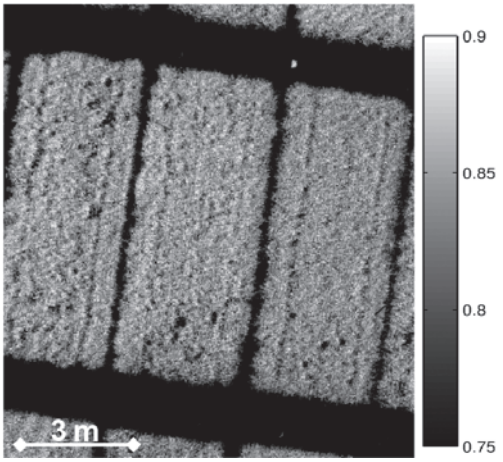

Fig. 12: Calculated NDVI for the RHC image taken on June 14th, 2013.

the FS3. The reason for this is not clear at this stage, because the RHC was calibrated against the reference panel, too. But the NDVI values are in an order and pattern as expected and the UHD185 showed weaker performances against the FieldSpec3 measurements on other dates. The higher spatial resolution of the RHC's hyperspectral sensor is documented in the calculated NDVI image shown in Fig.12.

4 Discussion and Conclusions

In this study, we flew the Rikola hyperspectral camera (RHC) and the Cubert UHD185 Firefly with a low-weight and low-cost UAV. Both cameras worked well, had some minor handling problems in the field, and the flight campaigns successfully delivered hyperspectral data. The spectral calibration in the field against a white reference panel was possible for both sensors. While the UHD185 was strong in capturing the whole spectrum within one image, the RHC had a higher spatial resolution in the selected hyperspectral wavelength resulting in a lower spectral resolution. While the RHC was only flown once together with the Rikola company, the UHD185 was flown in multiple campaigns.

For both cameras the spectral calibration is still an issue. While the spectral pattern and magnitudes are in the order of the field measurements, the first comparison with field spectra show clearly a lack of understanding in the spectral calibration of the sensors. Additionally, the UHD185 and the RHC were flown in different image acquisition modes. Future research of using the two cameras must focus on the hyperspectral image properties in terms of BDRF and calibration. Because of the latter the results stated in this paper should be seen as a first indicator of the suitability of hyperspectral full-frame cameras for precision agriculture applications. Despite the differences between the FS3 measurements and the hyperspectral full-frame sensors in some of the measurements the results show the potential of this new technology. Similar comparison approach between ASD Hand-held 2 and UAV-based sensors, such as Mini MCA6 (Tetracam) and STS spectrometer (Ocean Optics), were performed by von Bueren et al. (2014), but only in the spectral domain of 350 nm – 850 nm. The spectra from the different sensors showed similar magnitudes and patterns. However, further research needs to investigate a best practice for full-frame UAV hyperspectral sensors to generate robust and reproducible data. Both sensors operated well in the air and recorded the data as configured. Due to the small field of view of both sensors capturing the right footprint was a challenge. The latter may be solved with improved knowledge of the sensor and optimized flying trajectories.

The new technological designs of both hyperspectral sensors result in a low weight and enable hyperspectral imaging campaigns with UAV at a take-off weight below 5 kg. In Germany, this is important due to aviation regulations, since the application procedure for permissions are easier than for heavier UAVs. Apart from the mentioned critical points, both sensors open a new era of hyperspectral imaging. The flexibility of low-weight UAVs enable a temporal resolution which could not been realized in the past by (manned) aerial- or satelliteborne imaging. The same is true for the spatial resolution. Super-high resolutions of < 2 cm are possible on field scale and up to a few square kilometres, even in 3D (Bendig et al. 2013). Using stereophotogrammetric or structure for motion image analysis techniques with precise RTK measured ground control points, DEMs or in general surface models can be obtained in a resolution and precision of less than 2 cm. In Fig. 13, such a

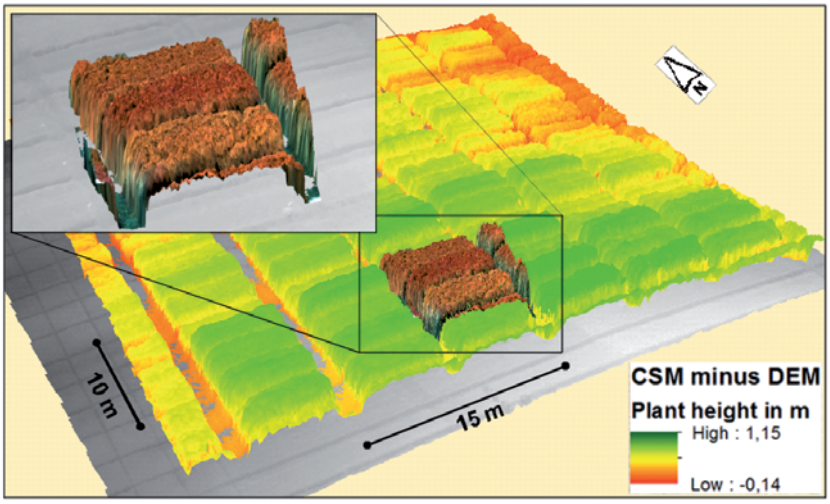

Fig. 13: 3D hyperspectral surface with a spatial resolution of 2 cm.

3D hyperspectral surface is shown for June 14th, 2013.

The combination of 3D imaging techniques and hyperspectral imaging enables the precise and accurate monitoring of crop growth during phenology. The analysis of multi-temporal crop surface models (CSM) (Bendig et al. 2013, Tilly et al. 2014) enables the precise monitoring of plant height and plant growth while hyperspectral analysis derive physiological plant parameters like chlorophyll or nitrogen content and others. Exactly this is needed for PreAg in terms of monitoring crop growth behaviour, crop vitality, and crop stress. The first data analyses are very promising and can be regarded as a new technological statement of sensor development, which will be a multiplier for applications not only in the field of crop monitoring.

Acknowledgements

The authors acknowledge the funding of the CROP.SENSe.net project in the context of Ziel 2-Programms NRW 2007–2013 "Regionale Wettbewerbsfähigkeit und Beschäftigung (EFRE)" by the Ministry for Innovation, Science and Research (MIWF) of the state North Rhine Westphalia (NRW) and European Union Funds for regional development (EFRE) (005-1103-0018).

References

Aasen, H., Gnyp, M.L., Miao, Y. & Bareth, G., 2014: Automated hyperspectral vegetation index retrieval from multiple correlation matrices with HyperCor. – Photogrammetric Engineerung & Remotre Sensing **80** (8): 785–795.

Bareth, G., Bendig, J. & Bolten, A., 2011: Potentials of low-cost Mini-UAVs. – Lenz-Wiedemann, V.I.S. & Bareth, G. (eds.): Workshop on Remote Sensing Methods for Change Detection and Process Modelling. – Kölner Geographische Arbeiten **92:** 1–8.

Bendig, J., Bolten, A. & Bareth, G., 2013: UAV-based Imaging for Multi-Temporal, very high Resolution Crop Surface Models to monitor Crop Growth Variability. – PFG – Photogrammetrie, Fernerkundung, Geoinformation **2013** (6): 551–562.

Bendig, J. & Bareth, G., 2014: Preface. – Bendig, J. & Bareth, G. (eds.): Workshop on UAV-based Remote Sensing Methods for Monitoring Vegetation. – Kölner Geographische Arbeiten **94:** 1–2.

Calderón, R, Navas-Cortés, J.A., Lucena, C. & Zarco-Tejada, P.J., 2013: High-resolution airborne hyperspectral and thermal imagery for early detection of Verticilliumwilt of olive using fluorescence, temperature and narrow-band spectral indices. – Remote Sensing of Environment **139:** 231–245.

Colomina, I. & Molina, P., 2014: Unmanned aerial systems for photogrammetry and remote sensing: A review. – ISPRS Journal of Photogrammetry and Remote Sensing **95:** 79–97.

Gnyp, M.L., Yu, K., Aasen, H., Yao, Y., Huang, S., Miao, Y. & Bareth, G., 2013: Analysis of crop reflectance for estimating biomass in rice canopies at different phenological stages. – PFG – Photogrammetrie, Fernerkundung, Geoinformation **2013** (4): 351–365.

Gnyp, M.L., Miao, Y., Yuan, F., Ustin, S.L., Yu, K., Yao, Y., Huang, S. & Bareth, G., 2014: Hyperspectral canopy sensing of paddy rice aboveground biomass at different growth stages. – Field Crops Research **155:** 42–55.

Honkavaara, E., Saari, H., Kaivosoja, J., Pölönen, I., Hakala, T., Litkey, P., Mäkynen, J. & Pesonen, L., 2013: Processing and Assessment of Spectrometric, Stereoscopic Imagery Collected Using a Lightweight UAV Spectral Camera for Precision Agriculture. – Remote Sensing **5:** 5006–5039.

Koppe, W., Gnyp, M.L., Hennig, S., Li, F., Miao, Y., Chen, X., Jia, L. & Bareth, G., 2012: Multi-temporal hyperspectral and radar remote sensing for estimating winter wheat biomass in the North China Plain. – PFG – Photogrammetrie, Fernerkundung, Geoinformation **2012** (3): 281–298.

Laudien, R. & Bareth, G., 2006: Multitemporal hyperspectral data analysis for regional detection of plant diseases by using a tractor- and an airborne-based spectrometer. – PFG – Photogrammetrie, Fernerkundung, Geoinformation **2006** (3): 217–227.

Laudien, R., Bürcky, K., Doluschitz, R. & Bareth, G., 2006: Aufbau einer webgestützten Spektralbibliothek zur Analyse hyperspektraler Daten von mit Rhizoctonia solani inokulierten Zuckerrüben (Establishment of a web-based spectral database for the analysis of hyperspectral data from Rhizoctonia solani-inoculated sugar beet). – Sugar Industry (Zuckerindustrie) **131** (56): 164–170.

Li, F., Miao, Y., Chen, X., Zhang, F., Jia, L. & Bareth, G., 2010: Estimating winter wheat biomass and nitrogen status using an active crop sensor. – Intelligent Automation and Soft Computing **16** (6): 1219–1228.

Mäkeläinen, A., Saari, H., Hippi, I., Sarkeala, J. & Soukkamäki, J., 2013: 2D Hyperspectral frame imager camera data in photogrammetric mosaicking. – International Archives of the Photogrammetry, Remote Sensing and Spatial Information Sciences **XL-1/W2:** 263–267.

Mulla, D.J., 2013: Twenty five years of remote sensing in precision agriculture: Key advances and remaining knowledge gaps. – Biosystems Engineering **114:** 358–371.

Oerke, E.C., Gerhards, R., Menz, G. & Sikora, R.A. (eds.), 2010: Precision crop protection – the challenge and use of heterogeneity. – 441 pp., Springer, Dordrecht, The Netherlands.

Rondeaux, G., Steven, M. & Baret, F., 1996: Optimization of soil-adjusted vegetation indices. – Remote Sensing of Environment **55:** 95–107.

Tilly, N., Hoffmeister, D., Ciao, Q., Huang, S., Miao, Y., Lenz-Wiedemann, V. & Bareth, G., 2014: Multi-temporal Crop Surface Models: Accurate plant height measurement and biomass estimation with terrestrial laser scanning in paddy rice. – Journal of Applied Remote Sensing **8** (1): 083671.

Thenkabail, P.S., Lyon, J.G. & Huete, A., 2011: Hyperspectral Remote Sensing of Vegetation. – 705 pp., CRC Press, FL, USA.

Thenkabail, P.S., Smith, R.B. & Pauw, E.D., 2000: Hyperspectral vegetation indices and their relationship with agricultural crop characteristics. – Remote Sensing of Environment **71** (2): 152–182.

von Bueren, S., Burkart, A., Hue Ni, A., Rascher, U., Tuohy, M. & Yule, I., 2014: Comparative validation of UAV based sensors for the use in vegetation monitoring. – Biogeosciences Discussions **11:** 3837–3864.

Whelan, B. & Taylor, J., 2013: Precision agriculture for grain production systems. – 208 pp., CSIRO Publishing.

Yu, K., Li, F., Gnyp, M.L., Miao, Y., Bareth, G. & Chen, X., 2013: Remotely detecting canopy nitrogen concentration and uptake of paddy rice in the Northeast China Plain. – ISPRS Journal of Photogrammetry and Remote Sensing **78:** 102–115.

Zarco-Tejada, P.J., Gonzáles-Dugo, V. & Berni, J.A.J., 2012: Fluorescence, temperature and narrow-band indices acquired from a UAV platform for water stress detection using a micro-hyperspectral imager and a thermal camera. – Remote Sensing Environment **117:** 322–337.

Zhang, C. & Kovacs, J.M., 2012: The application of small unmanned aerial systems for precision agriculture: a review. – Precision Agriculture **13:** 693–712.

Address of the Authors:

Prof. Dr. Georg Bareth, Helge Aasen, Juliane Bendig & Dr. Andreas Bolten, University of Cologne, Institute of Geography, GIS & RS Group, Albertus-Magnus-Platz, D-50923 Köln, Tel.: +49-221-470-6265, Fax: +49-221-470-8838, e-mail: {juliane.bendig}, {andreas.bolten}, {g.bareth}@uni-koeln.de

Dr. Martin Leon Gnyp, Research Centre Hanninghof, Yara International, c/o Yara GmbH & Co KG, Hanninghof 35, D-48249 Dülmen, Tel.: +49-2594-

798-196, Fax.: +49-2594-7455, e-mail: martin.gnyp@yara.com

Dr. András Jung, Institute of Geography, University of Leipzig, Johannisallee 19, D-04103 Leipzig, Tel.: +49-341-97-32785, Fax: +49-341-97-32799, e-mail: andras.jung@uni-leipzig.de

Dr. René Michels, Cubert GmbH, Real Time Spectral Imaging, Helmholtzstraße 12, D-89081 Ulm, Tel.: +49-73-11-42-99-97, e-mail: michels@cubert-gmbh.de

Jussi Soukkamäki, Rikola LTD., Kaitoväylä 1, FI-90570 Oulu, Finland, Tel.: +358-40-540-8794, e-mail: jussi.soukkamaki@rikola.fi

Manuskript eingereicht: Juli 2014
Angenommen: September 2014

PFG 2015 / 1, 0081 – 0094
Stuttgart, February 2015

Article

Comparison of SVM and Boosted Regression Trees for the Delineation of Lacustrine Sediments using Multispectral ASTER Data and Topographic Indices in the Lake Manyara Basin

Felix Bachofer, Geraldine Quénéhervé, Michael Märker & Volker Hochschild, Tübingen

Keywords: SVM, boosted regression trees, ASTER, multispectral, topographic indices

Summary: The lower member of the so called Manyara Beds is a distinct lacustrine sedimentary layer which indicates, with an elevation of more than 140 m above today's lake level, a high stand of the paleolake Manyara in the Monduli District in northern Tanzania. The Manyara Beds are rich in Pleistocene vertebrate fossils. In this study we focus on the delineation of this specific stratigraphic layer in order to yield new insights into paleontological settings, landscape evolution and to plan paleontological fieldwork. We compare the performance of a support vector classifier with a linear as well as a Gaussian kernel, with boosted regression tree approaches to identify the lithostratigraphic layers of the Manyara Beds. For the identification of the lacustrine sediments, multispectral information of ASTER satellite imagery and topographic indices derived from a digital elevation model were utilized as input feature sets. Acceptable classification accuracies were obtained with all methods. Thus, the Manyara Beds can be delineated and new sites with paleolake sediments were detected. The highest overall accuracy with 92% was provided by the support vector machine approach with a linear kernel for a binary classification problem. For a multi-class classification problem with three target classes the support vector classifier achieved 80% accuracy with a linear, as well as a Gaussian kernel.

Zusammenfassung: *Vergleich von SVM und Boosted Regression Trees zur Abgrenzung von lakustrinen Sedimenten anhand von multispektralen ASTER Daten und topographischen Parametern im Einzugsgebiet des Manyara Sees.* Die aus vornehmlich lakustrinen Sedimenten bestehende ältere Gruppe der stratigraphischen Einheit der Manyara Beds beschreibt mit einer Höhe von mehr als 140 m über dem heutigen Seespiegel einen Hochstand des Paläosees Manyara im Monduli Distrikt im nördlichen Tansania. Die Manyara Beds sind reich an pleistozänen Wirbeltierfossilien. Die vorliegende Arbeit beschäftigt sich mit der räumlichen Abgrenzung dieser stratigraphischen Einheit um mehr über die paläontologischen Ablagerungsbedingungen und die Landschaftsgeschichte zu erfahren, sowie die Planung von paläontologischen Geländearbeiten zu unterstützen. Wir vergleichen anhand der lithostratigraphischen Einheit der Manyara Beds die Leistungsfähigkeit eines Support Vector (Stützvektoren) Klassifizierungsansatzes, mit einem linearen und einem Gaußschen Kernel, und mit Klassifizierungsbäumen (Boosted Regression Trees). Um die lakustrinen Sedimente zu unterscheiden, wurden multispektrale Informationen einer ASTER Satellitenaufnahme und topographische Parameter von einem digitalen Höhenmodell als Eingangsvariablen genutzt. Mit allen Klassifizierungsmethoden wurden zufriedenstellende Genauigkeiten erzielt. Somit konnte das Auftreten der Manyara Beds räumlich abgegrenzt und bisher nicht dokumentierte Flächen mit lakustrinen Sedimenten erfasst werden. Die höchste Klassifizierungsgenauigkeit von 92% wurde von der Support Vector Machine Klassifizierung mit einem linearen Kernel für eine binäre Klassifizierung erreicht. Für eine Aufgabenstellung mit Support Vector Machines für drei Zielklassen wurde eine Genauigkeit von 80% sowohl mit einem linearen, als auch mit einem Gaußschen Kernel erreicht.

www.schweizerbart.de
DOI: 10.1127/pfg/2015/0251 1432-8364/15/0251 $ 3.50

1 Introduction

Lacustrine sediments and paleo-shorelines of different Quaternary lake-level high stands can be observed in the north, south and east of the Lake Manyara basin of northern Tanzania. The study area is located in the Gregory Rift in Central North Tanzania. The basin is of paleontological and archeological interest documented by several investigations in recent years (e.g. Schlüter et al. 1992, Kaiser et al. 2010, Prendergast et al. 2013). One of the richest stratigraphic units in vertebrate fossils and artifacts in the region are the Manyara Beds, which indicate a high level of the paleolake Manyara at more than 140 m above today's lake level. The identification of the Manyara Beds contributes to the understanding of landscape evolution and the spatial distribution of potential paleontological sites. Thus, the study also serves for the planning of future fieldwork in the study area.

Remote sensing images are used in different studies to derive information on the extent of paleolakes and other paleo-landscape forms. ElSheikh et al. (2011) and Elmahdy (2012) used remote sensing, GIS and geophysical methods to delineate a paleolake in northern Darfur. Ghoneim et al. (2012) used an integrated approach with optical and microwave data to map a paleo-drainage system. The use of remote sensing in combination with topographic analysis for the delineation of paleolakes has been successfully applied by Gaber et al. (2009) on the Sinai Peninsula.

Mountrakis et al. (2011) review the application of support vector machines (SVM) in the classification of remotely sensed images. SVM and boosted regression tree analysis (BRT) were more and more used in the last decade and yield high accuracies (Foody & Ajay 2004, Esch et al. 2009, Wang et al. 2011, Gómez et al. 2012, Gessner et al. 2013). SVM and BRT analyses are capable of handling multiple input features, outliers, non linear tasks and redundant data (Foody & Ajay 2004, Elith et al. 2008). Hahn & Gloaguen (2008) used SVM to classify soil types and soil texture from ASTER multispectral data and topographic parameters in the Erzgebirge in Germany. BRT methods have been assessed with remote sensing data for land use issues (Pal & Mather 2003, Chan & Paelinckx 2008). The mapping of lithological units and the distribution of soil with multispectral data and terrain attributes as well as classification methods were reviewed by Mulder et al. (2011). In this study we compare the accuracy of SVM and BRT classifier in identifying the Manyara Beds in a small scaled, heterogeneous environment. Pal & Foody (2010) showed that an increase of input features may lead to a decline of classification accuracy. Therefore, we apply a feature selection to choose a subset of different ASTER spectral bands, multispectral indices and topographical indices. From this selected set of features, we expect also improved model interpretability, as well as an enhanced generalisation of the resulting models.

2 Regional setting and data preparation

2.1 *Study Area*

The Lake Manyara catchment in northern Tanzania is an endorheic basin and part of the eastern branch of the East African Rift System (Fig. 1). Today Lake Manyara is a shallow soda lake (954 m a.s.l.) with a maximum depth of 1.18 m (Deus et al. 2013). The basin is an asymmetrically shaped half graben, with a 200 m to 600 m high escarpment along the western shoulder. The eastern shoulder of the Rift is lower in elevation and consists of tectonic blocks that are dipping towards the west. The North-eastern parts of the catchment area are dominated by the volcano Essimingor. Paleo-shorelines can be found especially on the Eastern part of the rift tracing different paleolake levels up to 80 m above today's lake level. The latter forms also the lowest possible outlet into the Engaruka and Lake Natron basin (Keller et al. 1975, Bachofer et al. 2014). The maximum age of the paleo-shorelines was established with radiocarbon dating (Th/U series) to 140,000 a BP (Casanova & Hillaire-Marcel 1992). Besides the springs at the base of the escarpment, Lake Manyara is mainly fed with seasonal drainages of the Tarangire and Makuyuni rivers. Today a bimodal precipitation pattern with an average annual rainfall of about 700 mm can be observed for

the study area. The resulting semiarid vegetation cover is sparse and dominated by bushed grassland (Bachofer et al. 2014).

2.2 *The Manyara Beds*

The lacustrine and fluvial stratigraphic units, known as the Manyara Beds in the east of Lake Manyara, reach up to approximately 140 m above today's lake surface. They describe the maximum extent of the lake (Schwartz et al. 2012). The Manyara Beds are rich in Pleistocene vertebrate fossils. In the Lake Manyara area, especially close to the village of Makuyuni, two hominin-bearing sites (0.63 and 0.78 Ma), vertebrate fossils and handaxes from different periods were found (Kaiser et al. 2010, Frost et al. 2012). The Manyara Beds consist of a lacustrine grayish lower member (mudstones, siltstones, diatomites, marls and tuff) which was deposited between 1.03 and 0.633 Ma, and a fluvial and terrestrial upper member which is composed of up to 13 m thick reddish brown upper member (siltstones, mudstones, conglomerates and breccias) deposited between 0.633 and 0.44 (0.27) Ma. The transition between both members is in most sections marked by a distinct tephra layer (Frost et al. 2012). Sections of the Manyara Beds are best exposed in the surroundings of the town Makuyuni, where Holocene soils and caliche overlay the sediments and where various gully systems erode into the savanna landscape. Laboratory analysis of representative samples of alluvial material of the Low-

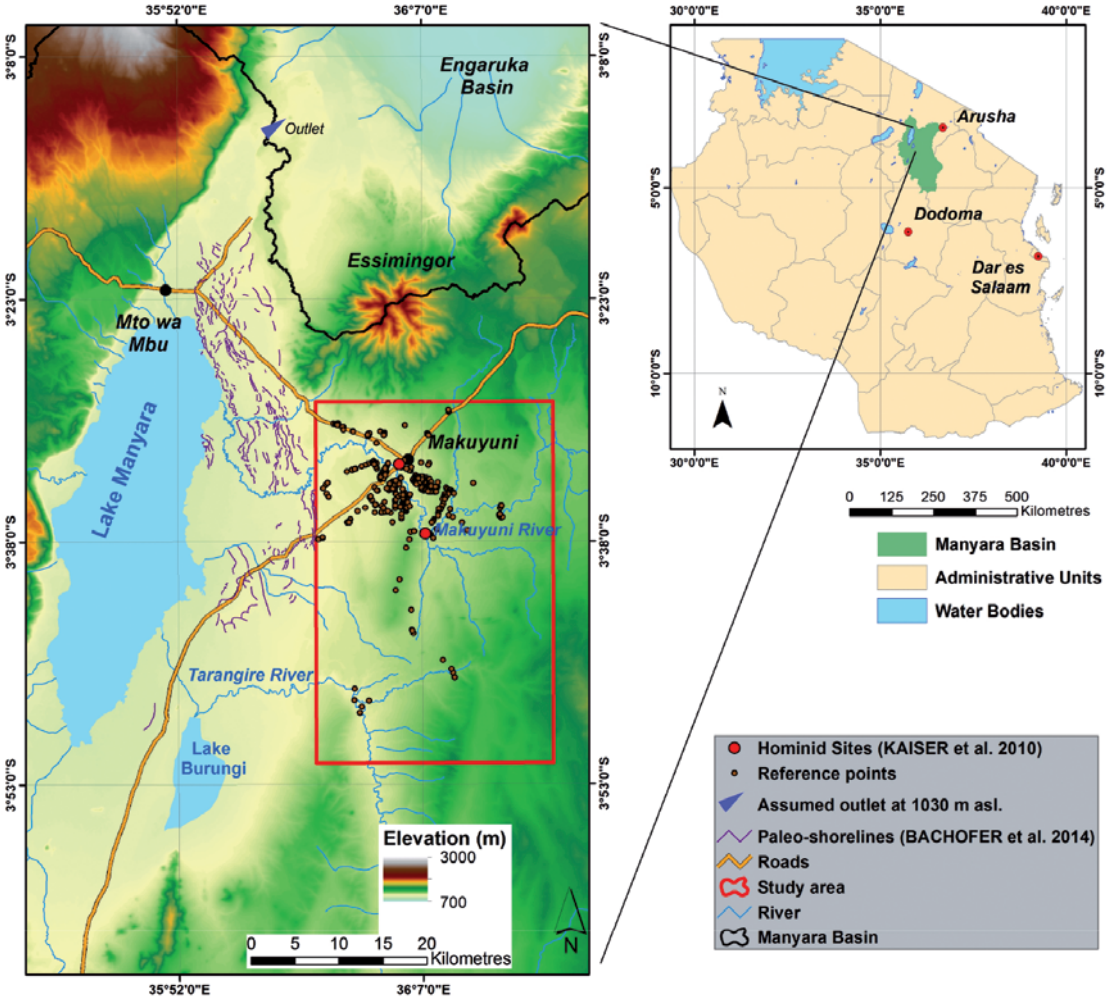

Fig. 1: The study area and the regional setting of Lake Manyara.

er Manyara Beds (LMB) and Upper Manyara Beds (UMB) were taken from the slopes of the Makuyuni river valley. They show heterogeneous texture, but distinct higher carbonate content in LMB and Fe^{2+} content in UMB. Organic carbon is dependent on the topographic position and adjacent soils and vegetation cover. Hence, the Manyara Beds show specific spectral and positional properties. Consequently, a successful delineation of the Manyara Beds with spectral bands, multispectral indices and topographical indices seem possible.

2.3 *ASTER Multispectral Data*

The Advanced Spaceborne Thermal Emission and Reflection Radiometer (ASTER) was launched with NASA's TERRA spacecraft in December 1999 (Yamaguchi et al. 1998). Its subsystems cover three bands in the visible-near infrared (VNIR), six bands in the shortwave infrared (SWIR) and five bands in the thermal infrared (TIR) wavelength regions (Tab. 1). The ground resolution is 15 m, 30 m and 90 m respectively (Fujisada 1995). Yamaguchi et al. (1998) stated that the VNIR spectral information was designed for use in mapping vegetation and iron oxides in soil and rocks, while the SWIR wavelengths were designed for soil and mineral mapping.

A cloud free ASTER L1B scene was obtained at August 23, 2006, 8:07 UTC during dry season. Because the SWIR bands of the L1B data is not corrected for a cross-detector leakage, crosstalk correction was applied following Iwasaki et al. (2002) using the correction software product from Earth Remote Sensing Data Applications Centre (ERSDAC).

The average geometric accuracy of the ASTER scene was validated by own ground control points (GCP) measurements and high resolution WorldView-2 imagery. A mean locational residual error of 61.4 m could be estimated which is close to the residual error calculated by Hewson et al. (2005). The GCPs and a Landsat ETM+ (L1T) panchromatic scene with 15 m ground resolution were used to improve the geometric accuracy using an automatic point matching algorithm. For our GCPs the Landsat scene showed a total RMSE of 16.5 m. The ASTER scene could be aligned with an RMSE of 0.9. However, the TIR bands were excluded from the analysis because of their low spatial resolution and some artifacts which were visible in the L1B and also in the surface emissivity product (AST05). To preserve the spectral information of the VNIR bands, the SWIR bands were resampled to the respective ground resolution of 15 m.

2.4 *Spectral Indices*

Multispectral indices derived from ASTER spectral bands are used in a broad range of studies with a main emphasis on vegetation, soil and lithology (Mulder et al. 2011, Pour & Hashim 2011). The spectral rationing of selective band absorption features of different materials at distinct wavelengths is utilized to emphasize the presence or absence of distinct mineral compositions or vegetation. From an extensive literature review a broad range of indices were collected and processed for this analysis (Tab. 2). Not all minerals, for which the indices were developed, are abundant in the study area. In addition, many of the indices carry redundant information because of the use of similar input bands and band combinations.

Tab. 1: ASTER spectral bands with the minimum lower and maximum upper band edges.

VNIR Green	0.52–0.60 µm	SWIR 3	2.185–2.225 µm
VNIR Red	0.63–0.69 µm	SWIR 4	2.235–2.285 µm
VNIR Near Infrared	0.76–0.86 µm	SWIR 5	2.295–2.365 µm
SWIR 1	1.600–1.700 µm	SWIR 6	2.360–2.430 µm
SWIR 2	2.145–2.185 µm	TIR 1 - 5	8.125–11.65 µm

Tab. 2: Spectral indices of ASTER VNIR and SWIR bands.

Index and literature reference	Formula	Index and literature reference	Formula
AlOH Group (Cudahy 2012)	(5/7)	AKP (Rowan & Mars 2003)	(4+6)/5
Alteration/Laterite (Bierwirth 2002)	(4/5)	Amphibole (Bierwirth 2002)	(6/8)
Alunite (Pour & Hashim 2011)	(7/5)*(7/8)	Calcite (Pour & Hashim 2011)	(6/8)*(9/8)
CCE (Rowan & Mars 2003)	(7+9)/8	Dolomite (Rowan & Mars 2003)	(6+8)/7
Clay 1 (Rowan & Mars 2003)	(5+7)/6	MgOH Group (Cudahy 2012)	(6+9)/(7+8)
Clay 2 (Bierwith 2002)	(5*7)/(6*6)	MgOH 1 (Hewson et al. 2005)	(6+9)/8
Kaolinitic (Hewson et al. 2005)	(7/5)	MgOH 2 (Cudahy 2012)	(7/8)
Kaolin Group (Cudahy 2012)	(6/5)	Ferric Iron³ (Rowan & Mars 2003)	(2/1)
Kaolinite (Pour & Hashim 2011)	(4/5)*(8/6)	Ferrous Iron 1 (Rowan et al. 2005)	(1/2)
Muscovite (Hewson et al. 2005)	(7/6)	Ferrous Iron 2 (Rowan & Mars 2003)	(5/3)+(1/2)
OH 1 (Pour & Hashim 2011)	(7/6)*(4/6)	Ferric Oxide (Cudahy 2012)	(4/3)
OH 2 (Ninomiya et al. 2005)	(4*7/6)/6	Gossan (Volesky et al. 2003)	(4/2)
OH 3 (Ninomiya et al. 2005)	(4*7/5)/5	Opaque Index (Cudahy 2012)	(1/4)
PHI (Hewson et al. 2005)	(5/6)	Ferrous Iron/Silicates (Cudahy 2012)	(5/4)
RBD6 (Rowan et al. 2005)	(4+7)/(6*2)	Burn Index (Hudak et al. 2004)	(3-5)/(3+6)
RBD8 (Rowan et al. 2005)	(7+9)/(8*2)	VI (Tucker 1979)	(3/2)
NDVI (Rouse et al. 1974)	(3-2)/3+2)	Salinity (Al-Khaier 2003)	(4-5)/(4+5)
STVI (Pour & Hashim 2011)	(3/2)*(1/2)		

Tab. 3: Topographic indices.

Slope (Travis et al. 1975)	Aspect (Travis et al. 1975)
Slope height (Boehner & Conrad 2008)	Valley Depth (Boehner & Conrad 2008)
Standardized Height (Boehner & Conrad 2008)	Normalized Height (Boehner & Conrad 2008)
Mid Slope Position (Boehner & Conrad 2008)	Downslope Distance Gradient (Hjerdt et al. 2004)
Plan Curvature (Zevenbergen & Thorne 1987, Dikau 1988)	Profile Curvature (Zevenbergen & Thorne 1987, Dikau 1988)
Negative Openness (Yokoyama et al. 2002)	Positive Openness (Yokoyama et al. 2002)
Morphometric Protection I. (Yokoyama et al. 2002)	Terrain Ruggedness Index (Riley et al. 1999)
Multiresolution Index of Valley Bottom Flatness (Gallant & Dowling 2003)	Multiresolution Index of Ridge Top Flatness (Gallant & Dowling 2003)
Relative Slope Position (Conrad 2005)	Geomorphones (Jasiewicz & Stepinski 2013)
Stream Power Index (Moore et al. 1991)	LS Factor (Moore et al. 1991)
Terrain Classification Index for Lowlands (Bock et al. 2007)	Topographic Position Index (Guisan et al. 1999, Jenness 2006)
Topographic Wetness Index (Beven & Kirkby 1979)	Vertical Distance to Channel Network (Conrad 2005)
Elevation (height above sea level; a.s.l) (DLR 2012)	

2.5 *Topographic Indices*

A track of the shuttle radar topography mission X-band (SRTM-X) digital elevation model (DEM) with 25 m ground resolution covers the study area. To eliminate the noise in the SRTM-X DEM, a multidirectional Lee filter was applied to preserve topographic features (Lee 1980). Different topographic indices (Tab. 3) were derived from the DEM to serve as independent features in the classification. The indices are used to characterize the topographic conditions of the Manyara Bed's location. The selected indices are listed in Tab. 3.

2.6 *Training and Reference Data*

As reference for this study, 498 ground reference points were collected during field campaigns between 2010 and 2014. Because of the time gap between the acquisition of the ASTER scene and the reference point selection, all points were taken with care even though the landscape is considered as relatively stable in relation to the ground resolution of the ASTER and SRTM-X data. Moreover, we assume that the mineral components of the Manyara Beds are conservative, means that in the study area environment they will change insignificantly over such a time period.

Some parts in the south and southeast of the study area are remote and partly inaccessible. Therefore, we applied a random clustered sampling strategy. The reference points are imbalanced with 40 points describing the UMBs, 139 points describing the LMBs, and 320 points with dissimilar landcover. To the latter class we refer to as "other landcover", which involves a rather complete reference selection of soils, minerals and vegetation within the study area, which were merged to take into account a potential landcover change. UMBs are not as abundant in the field as LMBs, which are the more important sediments for the reconstruction of the paleolake history. 20% of points from each class were randomly selected to serve exclusively as test datasets. Soils which are adjacent to or developed from the Manyara Beds were not classified as Manyara Beds. Reference points were collected describing the relative spatial distribution of the Manyara Beds with a minimum size of at least the VNIR resolution (15 m^2) for the UMBs and at least 30 m^2 for LMBs and "other landcover". The relatively small area for the UMBs was defined because they generally appeared as small sections or outcrops of red tuffs on the valley slopes.

3 Methodology

3.1 *Support Vector Machines*

The concept of support vector machines (SVM) based supervised classification originates from machine learning methodology and was introduced by Vapnik (1995, 1999). Due to different characteristics, the SVM algorithm has become very popular for pattern recognition and classification (Foody & Mathur 2004). While most remote sensing classification methods are mainly based on statistical properties of pixel and objects, SVMs maximizes the boundaries between intended classes. The problem of linear separating classes in an n-dimensional feature space, resulting from multiple independent input features is solved by applying kernel functions. By maximizing the margin between classes, an optimal separating hyperplane is strived for (Burges 1998, Hearst 1998). Only a small selection of feature values in the training data, which are close to the margin, are needed to define the hyperplane. These features are referred to as support vectors. Too many outliers within the training dataset would result in an over-fitting of the hyperplane. The cost parameter C determines a penalty for the support vectors which excludes outliers and results in a so called "soft margin". C controls thereby the balance between over-fitting (high values) and generalization (low values) of the maximum margin and must be selected carefully (Vapnik 1995 & 1999, Schölkopf & Smola 2002, Foody & Mathur 2004).

For this analysis, support vector classifier (C-SVC) from the *Library for Support Vector Machines* (LIBSVM) developed by Chang & Lin (2011) was utilized. It implements a "one-against-one" approach, which builds a classifier for each target value pair. The classification was conducted with a linear kernel and

the radial basis kernel function (RBF) which is widely used when a nonlinear relation is expected (Foody & Mathur 2004). The width of the RBF or Gaussian kernel is controlled by the constant γ, with high values describing a far reaching influence of the training sample and a low value for influencing the adjacent feature space. A grid search was applied by iteratively cross-validating the accuracy of test data classification, while optimizing the constants *C* and γ. All input feature sets were scaled to the range [-1, +1]. For the selection of features we applied the recursive feature elimination (RFE) technique which is widely used with SVM approaches following Guyon & Elisseeff (2003). In an iterative process the features are weighted according to their ability of discriminating the target classes. At each step the most insignificant features are eliminated recursively.

3.2 *Boosted Regression Trees*

Boosted regression trees (BRT), also known as stochastic gradient boosting (Elith et al. 2006), combine classification and regression trees with the gradient boosting algorithm (Friedman 2001). This method employs a learning algorithm to identify a model that fits best the relationship between a feature set and the class label of the target classes. We ran the model using the free statistical programming language R (R Development Core Team 2008) with the package *adabag* (Alfaro et al. 2013). The boosting algorithm used in *adabag* is the AdaBoost (adaptive boosting) algorithm based on Freund & Schapire (1996). The goal of the algorithm is to improve the accuracy of a tree by combining single predictor variables into classifiers. The points along the tree where the features are split are called nodes. Bagging reduces the variance and hence increases the prediction accuracy by taking repeated samples from the training dataset to build a prediction model and then averages the resulting predictions. Boosting constructs each tree on the original dataset but each tree is grown using information from previously grown trees. When a binary classification problem is extended to a multi-class classification problem, most boosting algorithms have to reduce the multi-class classification problem to multiple binary-class problems. However, the AdaBoost.M1 and the SAMME algorithms extend the AdaBoost algorithm to the multi-class case (Zhu et al. 2009). The difference between the algorithms is the calculation of the α constant, which estimates the error of the classifier for each tree iteration. For binary classifications SAMME is equivalent to AdaBoost.M1. The measure of the relative importance of the input features uses the gain of the Gini index (Alfaro et al. 2013), which measures the divergences between the probability distribution of the values of a feature. Best results for both approaches were achieved with the building of 500 trees and 5 nodes for each tree.

4 Results

The classification of the Manyara Beds for two classes (LMB, "other landcover") and three classes (LMB, UMB, "other landcover") with SVM and BRT was conducted with different sets of input feature combinations. As shown in Tabs. 4 and 5, the nine "Spectral Bands" of ASTER, the derived "Spectral Indices" and "Topographic Indices" derived from the DEM were considered for classification separately. Additionally, we show also the model performance considering "All Features" as well as a "Selection of Features" which were identified for SVM and BRT as the features with the highest importance for solving the classification problem (Fig. 2). The number of relevant features varies between the different methods and parameterizations. The smallest number of features (20) was identified for the SVM with an RBF kernel and the binary classification problem, the highest number (66) for the BRT approaches (Tabs. 4 and 5). The BRT methods stabilized with about 80 trees for the binary classification and for the multi-class problem between 130 and 500, depending on the feature set (Fig. 3).

The highest accuracy with 92% was achieved with SVM (linear kernel) and all "Spectral Bands" as well as "Spectral Indices" and "Topographic Indices" for the binary classification of LMB against "other landcover" (Tab. 4). Both linear and RBF kernels perform for the two classes with similar ac-

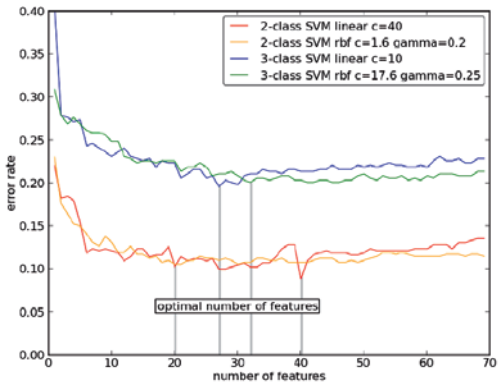

Fig. 2: Relationship between error rate and number of features selected by SVM-RFE.

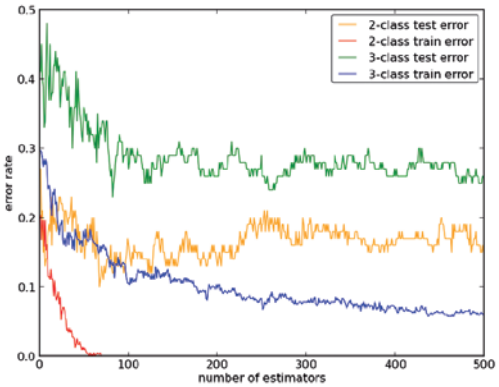

Fig. 3: AdaBoost SAMME error rate in relation to the number of trees for selected features.

Tab. 4: Overall accuracy and applied parameters for SVM and BRT. Binary classification scheme: LMB & "other landcover". Highest overall accuracy displayed in boldface (no = number of features).

	Spectral Bands (no: 9)	Spectral Indices (no: 35)	Topographic Indices (no: 25)	All Features (no: 69)	Selected Features
SVM linear	85% *C*: 75	86% *C*: 8	86% *C*: 8	**92%** *C*: 50	91% (no: 40) *C*: 40
SVM RBF	84% *C*: 29 γ: 1.5	87% *C*: 39.5 γ: 0.135	88% *C*: 50 γ: 1	89% *C*: 1.5 γ: 0.16	89% (no: 20) *C*: 1.6 γ: 0.2
BRT AdaBoost.M1	82%	85%	86%	89%	90% (no: 66)

Tab. 5: Overall accuracy and applied parameters for SVM and BRT. Three-class classification scheme: LMB, UMB & "other landcover". Highest overall accuracy displayed in boldface (no = number of features).

	Spectral Bands (no: 9)	Spectral Indices (no: 35)	Topographic Indices (no: 25)	All Features (no: 69)	Selected Features
SVM linear	74% *C*: 2	73% *C*: 4	72% *C*: 8	79% *C*: 1.5	**80%** (no: 27) *C*: 10
SVM RBF	75% *C*: 20 γ: 1.6	78% *C*: 12.5 γ: 0.105	73% *C*: 3 γ: 0.15	**80%** *C*: 3 γ: 0.235	**80%** (no: 32) *C*: 17.6 γ: 0.25
BRT AdaBoost.M1	75%	76%	72%	78%	78% (no: 66)
BRT SAMME	72%	75%	73%	79%	79% (no: 66)

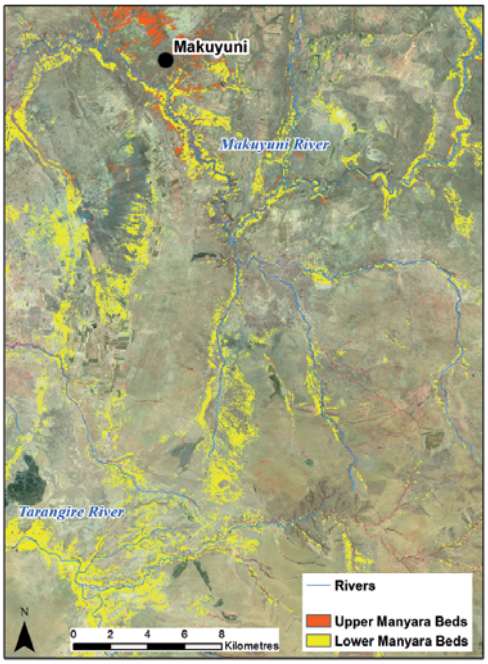

Fig. 4: Three-class SVM RBF result with "All Features", ASTER false colour infrared image (near-infrared, red, green) as background.

curacies. Only for the classification with "All Features" and the "Selected Features" the linear kernel can achieve a higher accuracy. The accuracies show a slightly lower performance for BRT than for both SVM methods.

When expanding the classification problem with the LMBs as the third class the overall accuracy drops with all possible combinations. The RBF kernel and the linear kernel perform similarly well and achieve 80% accuracy with "All Features" (Tab. 5). Fig. 4 shows the associated spatial distribution of the LMBs and UMBs. Stratigraphic units with similar topographic and spectral properties compared to the LMBs were identified in the south of the study area in the Tarangire River valley and further east in the Makuyuni River valley.

5 Discussion

In comparing the SVM classifier with linear and RBF kernels, as well as with the BRT AdaBoost.M1, results show that the binary classification problem can be solved with high accuracies of up to 92%. Regarding the binary

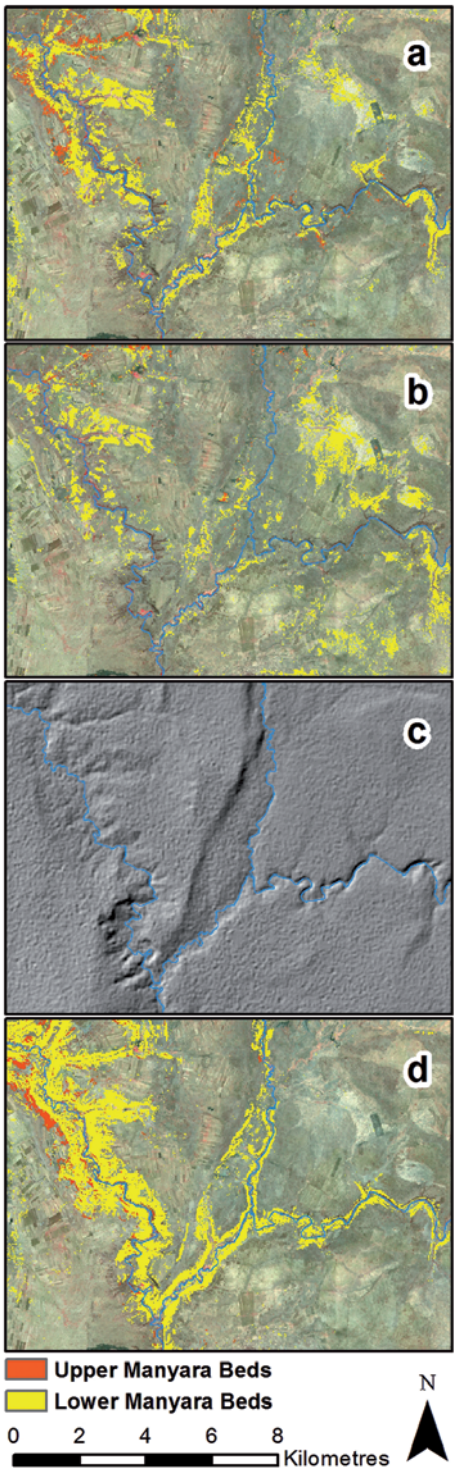

Fig. 5: Three-class SVM RBF comparison of different input features. ASTER false colour infrared image as background; a) SVM RBF with "All Features"; b) SVM RBF with 9 "Spectral Bands" of ASTER; c) hillshade of DEM; d) SVM RBF with "Topographic Indices".

classification problem, the linear and the RBF kernels yielded a very good performance. The BRT model performs marginally lower, but also at a high level. By enlarging the classification problem to three classes the overall accuracy drops by nearly 12% on average (Tabs. 4 and 5). The small number of UMB training features and their irregular spatial distribution result in an imbalanced training set and cause a lower overall accuracy. As for the three-class classification, the SVM with the RBF kernel as well as the SVM paired with the linear kernel perform slightly better than the BRT methods. The SVM three-class problem requires a higher generalization, leading to a wider hyperplane margin. The SVM binary problem however displays no such requirement (lower C values).

"Spectral Bands", "Spectral Indices" and "Topographic Indices" may be used as input features to explain the location of LMBs and UMBs. Both SVM methods perform similarly when using "All Features" and the RFE-"Selected Features". The same is true for the BRT methods. When using only "Topographic Indices" the binary classification approach detects the distribution of the Lower Manyara Beds better than with spectral information. Though for the three-class approach, the Lower and the Upper Manyara Beds seem to be separated better by spectral input features. "Spectral Bands" and "Spectral Indices" identify areas where the spectral information of the target classes is not (or only marginally) disturbed by heterogeneous land cover (Fig. 5b). The use of solely "Topographic Indices" results in a separation of the different topographic positions of the Manyara Beds within the study area (Fig. 5c, d). Consequently, the "Topographic Indices" with the multiclass scheme achieved the lowest accuracies because the topographic characteristics of the LMBs and the UMBs partly overlap. Accordingly, the combination of both spectral and topographic features best explains the distribution of the Manyara Beds (Fig. 5a).

Several optimized feature sets were identified which explain the distribution of the target classes with the training data (Fig. 2). Eight input features are common in all optimized feature sets (Tab. 6). The spectral feature VNIR Green (ASTER band 1) correlates with the

Tab. 6: Features which are common in all feature selection results.

VNIR Green	SWIR 6
Opaque Index	Stream Power Index
Multiresolution Index of Valley Bottom Flatness	Positive Openness
Plan Curvature	Elevation (height a.s.l.)

Manyara Beds. The spectral "Opaque Index" (Cudahy 2012) is sensitive to magnetite-bearing rocks, maghemite gravels, and manganese oxides. Whether the value distribution of the "Opaque Index" for this ASTER scene results from those specific absorption features can only be determined through further laboratory analysis or field spectroscopy. The spectral reflection characteristics may also result from other materials. The topographic information "Elevation (height a.s.l.)" describes the deposition on a distinct paleolake level. The topographic index "Positive Openness" expresses the degree of geometric dominance of one or several convex relief features. It therefore accurately highlights elevated areas (Yokoyama et al. 2002). "Plan Curvature" differentiates between ridges and valleys and may describe the incision of streams and gully systems into the lacustrine sediments. The "Multiresolution Index of Valley Bottom Flatness" (Gallant & Dowling 2003) may describe the depositional areas of the Manyara Beds.

Lacustrine sediments similar to the LMB are identified in the eastern part of the study area. After the first classification results we conducted a field check proving the predicted lacustrine sediments in the eastern part of the study area. In addition, vertebrate fossils are abundant at this location. Since the elevation of these sediments is higher than the LMBs, their elevation can be explained by a tectonic downshift of the block with the LMB as is proposed by Schwartz et al. (2012). This must have happened after or during the sedimentation of the Manyara Beds. The second explanation would propose a lake or swamp situation parallel to the paleolake Manyara. A gneissic ridge that is incised today by the Makuyuni River would have functioned as a barrier. The drainage of this lake was directed into the Tarangire River

in the south. Knick points of tributary river valleys indicate a change of the drainage direction. The third possibility would be a combination of both scenarios. For a further deciphering of the lake history a better dating of volcanic ridges and tuffs is needed.

6 Conclusions

This paper focused on a comparison between SVM and BRT methods, as well as the use of different sets of input features. All methods had performed with similar overall accuracies for the multi-class and the binary problem respectively. The best results were obtained using all spectral and topographic features to explain the distribution of the Manyara Beds. The highest accuracy for the binary classification of LMBs and "other landcover" were achieved with the SVM method and a linear kernel. For the classification of three classes (LMBs, UMBs, "other landcover") the SVM method with a RBF, as well as with a linear kernel performed best. In the case of the Lake Manyara area, small scale lithostratigraphic units could be delineated in a challenging environment, which entails a heterogeneous landcover with spectral similarity between different soils and a patchy vegetation cover. Besides the already known finding localities, new sites with paleolake sediments east of Makuyuni could be identified and may contribute to assessing the paleolake history of Lake Manyara. Lacustrine sediments in the south of the study area have to be validated in the field and their paleontological importance must be evaluated.

Acknowledgements

We would like to thank the editor and the reviewers for their time and valuable remarks. This study was financed by the Heidelberg Academy of Sciences and Humanities research center: "The Role of Culture in Early Expansions of Humans" (ROCEEH). The ASTER L1B data were obtained through the online Data Pool at the NASA Land Processes Distributed Active Archive Center (LP DAAC), USGS/Earth Resources Observation and Science (EROS) Center, Sioux Falls, South Dakota, USA. We would like to thank the DLR and the German Remote Sensing Data Center (DFS) for providing the SRTM/X-SAR data.

References

Alfaro, E., Gamez, M. & García, N., 2013: adabag: An R Package for Classification with Boosting and Bagging. – Journal of Statistical Software **54** (2): 1–35.

Al-Khaier, F., 2003: Soil Salinity Detection Using Satellite Remote Sensing. – Thesis, ITC Enschede, Netherlands.

Bachofer, F., Quénéhervé, G. & Märker, M., 2014: The Delineation of Paleo-Shorelines in the Lake Manyara Basin Using TerraSAR-X Data. – Remote Sensing **6** (3): 2195–2212.

Beven, K. & Kirkby, M.J., 1979: A physically based, variable contributing area model of basin hydrology. – Hydrological Sciences Journal **24** (1): 43–69.

Bierwirth, P., 2002: Evaluation of ASTER Satellite Data for Geological Applications. – Consultancy Report to Geoscience Australia.

Bock, M., Böhner, J., Conrad, O., Köthe, R. & Ringeler, A., 2007: XV. Methods for creating Functional Soil Databases and applying Digital Soil Mapping with SAGA GIS. – JRC Scientific and technical Reports, Office for Official Publications of the European Communities, Luxemburg.

Boehner, J. & Conrad, O., 2008: Terrain Parameters described in the SAGA-GIS Software, v.2.1.0. http://sourceforge.net/projects/saga-gis/files/latest/download?source=files (16.6.2014).

Burges, C., 1998: A Tutorial on Support Vector Machines for Pattern Recognition. – Data Mining and Knowledge Discovery **2** (2): 121–167.

Casanova, J. & Hillaire-Marcel, C., 1992: Chronology and paleohydrology of late Quaternary high lake levels in the Manyara basin (Tanzania) from isotopic data (18O, 13C, 14C, ThU) on fossil stromatolites. – Quaternary Research **38** (2): 205–226.

Chan, J.C.-W. & Paelinckx, D., 2008: Evaluation of Random Forest and Adaboost tree-based ensemble classification and spectral band selection for ecotope mapping using airborne hyperspectral imagery. – Remote Sensing of Environment **112** (6): 2999–3011.

Chang, C.C. & Lin, C.J., 2011: LIBSVM: A library for support vector machines. – ACM Transac-

tions on Intelligent Systems and Technology **2** (3): 1–27.

Conrad, O., 2005: Terrain Parameters described in the SAGA-GIS Software, v.2.1.0. http://sourceforge.net/projects/saga-gis/files/latest/download?source=files (16.6.2014).

Cudahy, T., 2012: Satellite ASTER Geoscience Product. – Notes for Australia; CSIRO: http://c3dmm.csiro.au/WA_ASTER/WA%20ASTER%20Geoscience%20Product%20Notes%2015112011.pdf (16.6.2014).

Deus, D., Gloaguen, R. & Krause, P., 2013: Water Balance Modeling in a Semi-Arid Environment with Limited in situ Data Using Remote Sensing in Lake Manyara, East African Rift, Tanzania. – Remote Sensing **5** (4): 1651–1680.

Dikau, R., 1988: Entwurf einer geomorphographisch-analytischen Systematik von Reliefeinheiten. – Heidelberger Geographische Bausteine, Heidelberg.

DLR, 2012: SRTM X-SAR Digital Elevation Models. Status: 2012-09-28. http://eoweb.dlr.de:8080/eoweb-ng/licenseAgreements/DLR_SRTM_Readme.pdf (23.12.2013).

Elith, J., Graham, C.H., Anderson, R.P., Dudík, M., Ferrier, S., Guisan, A., Hijmans, R.J., Huettmann, F., Leathwick, J.R., Lehmann, A., Li, J., Lohmann, L.G., Loiselle, B.A., Manion, G., Moritz, C., Nakamura, M., Nakazawa, Y., Overton, J.M.M., Townsend Peterson, A., Phillips, S.J., Richardson, K., Scachetti-Pereira, R., Schapire, R.E., Soberón, J., Williams, S., Wisz, M.S. & Zimmermann, N.E., 2006: Novel methods improve prediction of species' distributions from occurrence data. – Ecography **29** (2): 129–151.

Elith, J., Leathwick, J.R. & Hastie, T., 2008: A working guide to boosted regression trees. – Journal of Animal Ecology **77** (4): 802–813.

Elmahdy, S.I., 2012: Hydromorphological Mapping and Analysis for Characterizing Darfur Paleolake, NW Sudan Using Remote Sensing and GIS. – International Journal of Geosciences **2012** (3): 25–36.

ElSheikh, A., Abdelsalam, M.G. & Mickus, K., 2011: Geology and geophysics of the West Nubian Paleolake and the Northern Darfur Megalake (WNPL-NDML): Implication for groundwater resources in Darfur, northwestern Sudan. – Journal of African Earth Sciences **61** (1): 82–93.

Esch, T., Himmler, V., Schorcht, G., Thiel, M., Wehrmann, T., Bachofer, F., Conrad, C., Schmidt, M. & Dech, S., 2009: Large-area assessment of impervious surface based on integrated analysis of single-date Landsat-7 images and geospatial vector data. – Remote Sensing of Environment **113** (8): 1678–1690.

Foody, G.M. & Ajay, M., 2004: A relative evaluation of multiclass image classification by support vector machines. – IEEE Transactions on Geoscience and Remote Sensing **42** (6): 1335–1343.

Foody, G.M. & Mathur, A., 2004: Toward intelligent training of supervised image classifications: directing training data acquisition for SVM classification. – Remote Sensing of Environment **93** (1–2): 107–117.

Freund, Y. & Schapire, R.E., 1996: Experiments with a New Boosting Algorithm. – Thirteenth International Conference on Machine Learning, 148–156, Bari, Italy.

Friedman, J.H., 2001: Greedy function approximation: a gradient boosting machine. – Annals of Statistics, 1189–1232.

Frost, S.R., Schwartz, H.L., Giemsch, L., Morgan, L.E., Renne, P.R., Wildgoose, M., Saanane, C., Schrenk, F. & Harvati, K., 2012: Refined age estimates and Paleoanthropological investigation of the Manyara Beds, Tanzania. – Journal of Anthropological Sciences **90:** 1–12.

Fujisada, H., 1995: Design and performance of ASTER instrument. – SPIE, the Advanced and Next generation Satellites **2583:** 16–25, Paris, France.

Gaber, A., Ghoneim, E., Khalaf, F. & El-Baz, F., 2009: Delineation of paleolakes in the Sinai Peninsula, Egypt, using remote sensing and GIS. – Journal of Arid Environments **73** (1): 127–134.

Gallant, J.C. & Dowling, T.I., 2003: A multiresolution index of valley bottom flatness for mapping depositional areas. – Water Resources Research **39** (12): 1347.

Gessner, U., Machwitz, M., Conrad, C. & Dech, S., 2013: Estimating the fractional cover of growth forms and bare surface in savannas. A multi-resolution approach based on regression tree ensembles. – Remote Sensing of Environment **129:** 90–102.

Ghoneim, E., Benedetti, M. & El-Baz, F., 2012: An integrated remote sensing and GIS analysis of the Kufrah Paleoriver, Eastern Sahara. – Geomorphology **139–140:** 242–257.

Gómez, C., Wulder, M.A., Montes, F. & Delgado, J.A., 2012: Modeling Forest Structural Parameters in the Mediterranean Pines of Central Spain using QuickBird-2 Imagery and Classification and Regression Tree Analysis (CART). – Remote Sensing **4** (1): 135–159.

Guisan, A., Weiss, S. & Weiss, A., 1999: GLM versus CCA spatial modeling of plant species distribution. – Plant Ecology **143** (1): 107–122.

Guyon, I. & Elisseeff, A., 2003: An Introduction to Variable and Feature Selection. – Journal of Machine Learning Research **3:** 1157–1182.

Hahn, C. & Gloaguen, R., 2008: Estimation of soil types by non linear analysis of remote sensing

data. – Nonlinear Processes in Geophysics **15** (1): 115–126.

Hearst, M.A., 1998: Support Vector Machines. – IEEE Intelligent Systems **13** (4): 18–28.

Hewson, R.D., Cudahy, T.J., Mizuhiko, S., Ueda, K. & Mauger, A.J., 2005: Seamless geological map generation using ASTER in the Broken Hill-Curnamona province of Australia. – Remote Sensing of Environment **99** (1–2): 159–172.

Hjerdt, K.N., Mcdonnell, J.J., Seibert, J. & Rodhe, A., 2004: A new topographic index to quantify downslope controls on local drainage. – Water Resources Research **40** (5): W05602.

Hudak, A.T., Robichaud, P., Evans, J.S., Clark, J., Lannom, K., Morgan, P. & Stone, C., 2004: Field validation of Burned Area Reflectance Classification (BARC) products for post fire assessment. – University of Nebraska, Lincoln, NE, USA.

Iwasaki, A., Fujisada, H., Akao, H., Shindou, O. & Akagi, S., 2002: Enhancement of spectral separation performance for ASTER/SWIR. – SPIE, Infrared Spaceborne Remote Sensing **IX 4486:** 42–50, San Diego, CA, USA.

Jasiewicz, J. & Stepinski, T.F., 2013: Geomorphons – a pattern recognition approach to classification and mapping of landforms. – Geomorphology **182:** 147–156.

Jenness, J., 2006: Topographic Position Index (TPI) v.1.3a. – TPI_Documentation.pdf. http://www.jennessent.com/arcview/tpi.htm (17.6.2013).

Kaiser, T.M., Seiffert, C., Hertler, C., Fiedler, L., Schwartz, H.L., Frost, S.R., Giemsch, L., Bernor, R.L., Wolf, D., Semprebon, G., Nelson, S.V., Schrenk, F., Harvati, K., Bromage, T.G. & Saanane, C., 2010: Makuyuni, a new Lower Palaeolithic Hominid Site in Tanzania. – Mitteilungen Hamburgisches Zoologisches Museum und Institut **106:** 69–110.

Keller, C.M., Hansen, C. & Alexander, C.S., 1975: Archaeology and Paleoenvironments in the Manyara and Engaruka Basins, Northern Tanzania. – Geographical Review **65** (3): 364–376.

Lee, J.S., 1980: Digital image enhancement and noise filtering by use of local statistics. – IEEE Transactions on Pattern Analysis and Machine Intelligence **2** (2): 165–168.

Moore, I.D., Grayson, R.B. & Ladson, A.R., 1991: Digital terrain modelling: A review of hydrological, geomorphological, and biological applications. – Hydrological Processes **5** (1): 3–30.

Mountrakis, G., Im, J. & Ogole, C., 2011: Support vector machines in remote sensing: A review. – ISPRS Journal of Photogrammetry and Remote Sensing **66** (3): 247–259.

Mulder, V.L., De Bruin, S., Schaepman, M.E. & Mayr, T.R., 2011: The use of remote sensing in soil and terrain mapping – A review. – Geoderma **162** (1–2): 1–19.

Ninomiya, Y., Fu, B. & Cudahy, T.J., 2005: Detecting lithology with Advanced Spaceborne Thermal Emission and Reflection Radiometer (ASTER) multispectral thermal infrared "radiance-at-sensor" data. – Remote Sensing of Environment **99** (1–2): 127–139.

Pal, M. & Mather, P.M., 2003: An assessment of the effectiveness of decision tree methods for land cover classification. – Remote Sensing of Environment **86** (4): 554–565.

Pal, M. & Foody, G.M., 2010: Feature Selection for Classification of Hyperspectral Data by SVM. – IEEE Transactions on Geoscience and Remote Sensing **48** (5): 2297–2307.

Pour, A.B. & Hashim, M., 2011: Application of advanced spaceborne thermal emission and reflection radiometer (ASTER) data in geological mapping. – International Journal of the Physical Sciences **6** (33): 7657–7668.

Prendergast, M.E., Mabulla, A.Z.P., Grillo, K.M., Broderick, L.G., Seitsonen, O., Gidna, A.O. & Gifford-Gonzalez, D., 2013: Pastoral Neolithic sites on the southern Mbulu Plateau, Tanzania. – Azania: Archaeological Research in Africa **48** (4): 498–520.

R Development Core Team, 2008: R: A Language and Environment for Statistical Computing. – R Foundation for Statistical Computing, Vienna, Austria.

Riley, S.J., Degloria, S.D. & Elliot, R., 1999: A Terrain Ruggedness Index that quantifies topographic heterogeneity. – Intermountain Journal of Sciences **5** (1–4): 23–27.

Rouse, J.W., Haas, R.H., Shell, J.A., Deering, D.W. & Harlan, J.C., 1974: Monitoring the vernal advancement of retrogradation of natural vegetation. – Final Report, Type III, NASA/GSFC, Greenbelt, MD, USA.

Rowan, L.C. & Mars, J.C., 2003: Lithologic mapping in the Mountain Pass, California area using Advanced Spaceborne Thermal Emission and Reflection Radiometer (ASTER) data. – Remote Sensing of Environment **84** (3): 350–366.

Rowan, L.C., Mars, J.C. & Simpson, C.J., 2005: Lithologic mapping of the Mordor, NT, Australia ultramafic complex by using the Advanced Spaceborne Thermal Emission and Reflection Radiometer (ASTER). – Remote Sensing of Environment **99** (1–2): 105–126.

Schlüter, T., Kohring, R. & Mehl, J., 1992: Hyperostotic fish bones ("Tilly bones") from presumably Pliocene phosphorites of the Lake Man-

yara area, northern Tanzania. – Paläontologische Zeitschrift **66** (1–2): 129–136.

Schölkopf, B. & Smola, A.J., 2002: Learning with kernels: support vector machines, regularization, optimization, and beyond. – MIT Press, Cambridge, MA, USA.

Schwartz, H., Renne, P.R., Morgan, L.E., Wildgoose, M., Lippert, P.C., Frost, S.R., Harvati, K., Schrenk, F. & Saanane, C., 2012: Geochronology of the Manyara Beds, northern Tanzania: New tephrostratigraphy, magnetostratigraphy and 40Ar/39Ar ages. – Quaternary Geochronology **7:** 48–66.

Travis, M.R., Elsner, G.H., Iverson, W.D. & Johnson, C.G., 1975: VIEWIT: computation of seen areas, slope, and aspect for land-use planning. – Report PSW-11, Berkeley, CA, USA.

Tucker, C.J., 1979: Red and photographic infrared linear combinations for monitoring vegetation. – Remote Sensing of Environment **8** (2): 127–150.

Vapnik, V.N., 1995: The nature of statistical learning theory. – Springer, New York, NY, USA.

Vapnik, V.N., 1999: An overview of statistical learning theory. – Neural Networks, IEEE Transactions **10** (5): 988–999.

Volesky, J.C., Stern, R.J. & Johnson, P.R., 2003: Geological control of massive sulfide mineralization in the Neoproterozoic Wadi Bidah shear zone, southwestern Saudi Arabia, inferences from orbital remote sensing and field studies. – Precambrian Research **123** (2-4): 235–247.

Wang, X., Niu, R. & Wu, K., 2011: Lithology intelligent identification using support vector machine and adaptive cellular automata in multispectral remote sensing image. – Optical Engineering **50** (7): 076201, 1–12.

Yamaguchi, Y., Kahle, A.B., Tsu, H., Kawakami, T. & Pniel, M., 1998: Overview of Advanced Spaceborne Thermal Emission and Reflection Radiometer (ASTER). – IEEE Transactions on Geoscience and Remote Sensing **36** (4): 1062–1071.

Yokoyama, R., Shirasawa, M. & Pike, R.J., 2002: Visualizing topography by openness: a new application of image processing to digital elevation models. – Photogrammetric engineering and remote sensing **68** (3): 257–266.

Zevenbergen, L.W. & Thorne, C.R., 1987: Quantitative analysis of land surface topography. – Earth Surface Processes and Landforms **12** (1): 47–56.

Zhu, J., Zou, H., Rosset, S. & Hastie, T., 2009: Multi-class AdaBoost. – Statistics and its Interface **2:** 349–360.

Address of the Authors:

Dipl.-Geogr. Felix Bachofer, Dipl.-Geogr. Geraldine Quénéhervé, Prof. Dr. Volker Hochschild, Eberhard Karls Universität Tübingen, Geographisches Institut, D-72070 Tübingen, Tel.: +49-7071-29-77528, Fax: +49-7071-29-5378, e-mail: felix.bachofer@uni-tuebingen.de

Dr. Michael Märker, Heidelberger Akademie der Wissenschaften, ROCEEH, D-72070 Tübingen, Tel.: +49-7071-29-72135, e-mail: michael.maerker@geographie.uni-tuebingen.de

Manuskript eingereicht: Juni 2014
Angenommen: September 2014

PFG 2015 / 1, 0095–00104
Stuttgart, February 2015

Article

An Algorithm to Generate a Simplified Railway Network through Generalization

Paul Czioska, Frank Thiemann, Monika Sester, Robin Giese & Hermann Vogt, Hannover

Keywords: generalization, line merging, railway, skeletonisation

Summary: Maps play a major role in communicating information in the context of public railway transportation, for instance as route maps. In addition, the current position of the trains can be shown on such a map to enrich the information content (*Live Map*). For the positioning and routing of the trains on the track, a graph structure of the traffic network is necessary. Since railway tracks are mostly arranged in a parallel manner, it makes sense to merge the track lines into representative (centre-)lines, which reduces significantly the amount of edges and helps to identify possible topological errors in the input data. This work presents an algorithm which merges track data based on topological properties, so that branches and crossings can be distinguished. The implementation uses generalization techniques like an area collapse operator and methods from computational geometry like polygon triangulation. An evaluation shows that the output graph is capable for routing tasks.

Zusammenfassung: *Ein Algorithmus zur Erstellung eines vereinfachten Bahnnetzes durch Generalisierung.* Karten spielen eine wichtige Rolle bei der Informationskommunikation im Rahmen des öffentlichen Verkehrs, etwa als Liniennetzplan, auf dem zusätzlich die aktuelle Position des Verkehrsmittels dargestellt wird (*Live Map*). Um solche Karten zu erstellen, ist eine routingfähige Graphstruktur der Gleisdaten nötig. Da Gleise meist parallel verlaufen, ist es sinnvoll, die Gleise zu repräsentativen Linien zu aggregieren, um die Redundanz zu verringern und mögliche Topologiefehler der Eingangsdaten zu beheben. In dieser Arbeit wird ein Algorithmus vorgestellt, der einen Gleisdatensatz nach topologischen Eigenschaften zusammenfasst. Der Implementierungsansatz nutzt hierzu Techniken aus dem Bereich der Skelettierung von Polygonen durch Triangulation. Eine abschließende Evaluation zeigt, dass das Ergebnis für Routinganwendungen geeignet ist.

1 Introduction

The sector of public transportation is of outstanding importance for the infrastructure and thereby for the wealth of a country. According to Destatis (2013), approximately 30 million people per day use the public transportation system in Germany. It is obvious that such a huge and complex network needs an efficient way to communicate traffic information to its users.

Maps play a major role in this task. They are able to illustrate connections between different means of transport in a way that every user is able to understand quickly. In most cases, the connections are shown in a schematic manner, like the popular route map of the London Tube. Since this type of map lacks a lot of additional cartographic information, it has become also common to show the geometry of the route as an overlay on a real map, so that the user is able to locate stations and the travelled route in between.

A dynamic enhancement of this type of map is the so called *Live Map*, where, in addition to the tracks, the positions of the moving vehicles are drawn in real-time. The position information can be gathered either directly from GPS or indirectly calculated through spatiotemporal interpolation on the given track, like it can be seen for example at the German "*DB Zugradar*", www.bahn.de/zugradar (Fig. 1).

A basic requirement for the routing of the trains is a graph structure of the track network.

 www.schweizerbart.de
DOI: 10.1127/pfg/2015/0255 1432-8364/15/0255 $ 2.50

The nodes of this graph thus have real world coordinates, so that the correct geometry of the tracks can be shown. Such a graph structure is necessary for different tasks: the edges can be used to interpolate an approximation of the current position of the train when position signals are available only at discrete survey stations along the track, and a routing on the graph can be used to determine the complete route of a train. In some Live Map applications, this route can be highlighted when desired by the user (like the red line in the example of Fig. 1 shows).

A trivial solution to obtain a track graph is to use raw track data without any modification, that is, the line data of the tracks simply converted into a graph structure without any further processing. In fact, many Live Map applications at present use such an unprocessed data basis.

Track datasets for this purpose can be obtained either from official sources (like rail operators or transport associations) or derived from volunteered geographical information (VGI), accessible through portals like OpenStreetMap (OSM). Unfortunately, depending on the quality of the input data, one cannot be sure that the obtained track data is topologically correct, i.e. that line endings are connected properly. If this basic condition is not fulfilled, a routing will lead to unexpected errors, such as confusing detours or no possible connection at all. Especially when VGI is used as input data the quality cannot be ensured, so that an additional check is recommended.

Furthermore, it is apparent that railway tracks are mostly arranged in a parallel manner. If the whole track network is used for a routing application, a significant redundancy of track information is present that slows down the algorithm, while the single tracks are of no importance for a macroscopic routing application. In addition, users could be irritated when the Live Map shows a train pulling into a station on a specific platform, but in reality this platform was only chosen because it represents the shortest way in the graph and not the platform defined in the timetable. Hence, a transformation into a representative geometry is desirable in many cases.

In order to handle those issues, the task is therefore to generalize the redundant tracks while preserving the topologic relationship. In the context of generalization, this procedure can be classified as *merging* (Shea & McMaster 1989). As a by-product, the use of such an operator has the possibility to identify and repair incorrect input data. In detail, the following requirements are necessary:

- Bundle parallel tracks that belong to the same transport route and create a graph with real world coordinates that represents the approximate centre of the route (Fig. 2)
- Preserve the topology of the input data. In other words: insert a node at track switches (Fig. 3), but do not insert a node at crossings, e.g. bridges or tunnels (Fig. 4)
- Repair topological errors in the input data, so that the network is routable (Fig. 5).

In this paper we present an algorithm that fulfils these requirements and generates a simplified rail network graph. It combines different existing computational geometry methods such as buffering and skeletonisation and uses in addition a new technique called *Track Tracing*.

The outline of this paper is as follows. Section 2 gives a brief overview over other topics that are related to the current problem. In

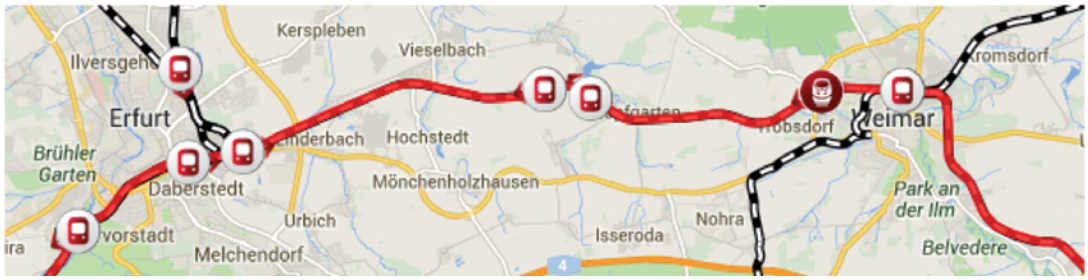

Fig. 1: Screenshot of the Live Map "*DB Zugradar*". Source: www.bahn.de/zugradar (24.6.2014)

Fig. 2: Task: Bundle parallel tracks.

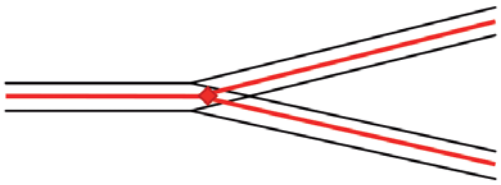

Fig. 3: Task: Insert a node at track route branches.

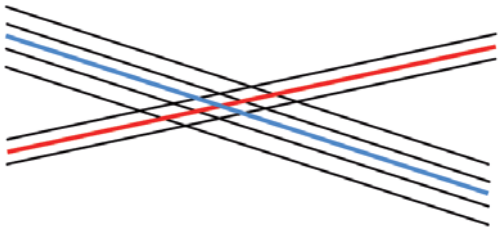

Fig. 4: Task: No node insertion at crossings.

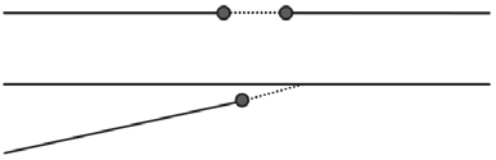

Fig. 5: Task: Handle topologic errors in the input dataset.

section 3, the algorithm is presented. Furthermore, in section 4 results of the process are shown. Section 5 discusses the evaluation of the results with a test routing. Finally, section 6 provides the conclusion and directions for future work.

2 Related Work

The generation of a routable graph network from line data without further simplification is a fairly simple task since it is sufficient to treat all vertices as nodes and add the corresponding line connections as edges to the graph. Problems may only arise when the input data is somehow flawed. Neis et al. (2011) discovered that the amount of topological errors at street connections in OpenStreetMap has declined rapidly in the past several years.

Nevertheless, the street topology is not flawless, so that an additional data preparation is still necessary.

However, most articles focus on street or pedestrian routing, whereas a routing on railway tracks or the quality of its geometry is not examined. Due to the lack of such measurements, we checked the topological integrity of railway track data from OpenStreetMap by a simple check of the distance between every node and its nearest neighbour. If the distance is greater than zero and above a certain threshold (we used an empirical value of 0.75 m), a node pair is marked as erroneous. The result of this systematic analysis showed that the raw railway track data in the region of Germany seems very suitable for the purpose of routing: in 175,000 nodes only 44 errors have been detected, corresponding to an error probability of ~ 0.03%. Certainly, for more accurate results a more sophisticated analysis is necessary since not every error type is covered in this test.

In terms of line network generalization, most previous work focuses also on road networks. A common approach is the principle of *good continuation* proposed by Thomson & Richardson (1999). In this work, a road network is grouped into linear elements called *strokes*, which represents a chain of road sections which have a good continuation. Based on this technique, Thom (2005) presents a method to collapse dual carriageways into a single centre line. Unfortunately, since railway vehicles have a huge turning radius, nearly all rail tracks have a relatively good continuation which makes this principle not applicable.

A topic that also deals with line merging is the map inference from movement trajectories. One of the main research topics in this field is the construction of a road map by processing vehicle tracking data. Due to the uncertainty of GPS measurements, trajectories

are mostly scattered around the true movement path. A reasonable way to infer a road network is therefore the creation of a centreline of all trajectories belonging to a common street segment, which is also a form of a merging operation.

One approach to achieve this goal using k-means clustering is presented by Edelkamp & Schrödl (2003). In the work of Lee et al. (2007), similar trajectories are detected and grouped in order to derive a representative trajectory for common parts, which is close to the problem investigated in this paper. Another inspiring idea comes from Cao & Krumm (2009), who simulate physical attraction between the trajectories. Zhang et al. (2010) describe a method to extract a centreline out of GPS traces with perpendicular lines using fuzzy c-means clustering in order to separate close roads. Biagioni & Eriksson (2012) present a map inference pipeline similar to the workflow described in this paper. First, a kernel density estimation (KDE) is applied on the raw GPS traces, which produces a density raster. Subsequently, a gray-scale skeletonisation is used to derive the road centrelines.

However, car trajectories differ in some characteristics from railway track data. Trajectories have measurement errors, while a track derived from a map is assumed to have the correct coordinates. Also, single lines are often treated as outliers in a car trajectory analysis and are thus neglected, but a single railway track has to be preserved. These differences reveal the requirement of a new algorithm.

3 Merging Operator

The basic concept of the proposed simplification operator is the merging of tracks which are located close to each other while preserving the underlying topological information of the traffic routes. In order to carry out this task, a kind of morphological operation is performed: At first, the tracks are buffered (Dilation), and subsequently the buffered area is transformed back to a line (Erosion), which corresponds to the Closing operation. The major challenge – which is also different from conventional skeleton approaches – is the preservation of the topological relations.

In detail, the algorithm consists of the following four steps, which are explained more in detail in the course of this section:

1) buffering of the tracks and amalgamation of all buffer polygons,
2) removal of holes,
3) triangulation of the buffer polygon,
4) creating the skeleton in consideration of the underlying tracks.

Optionally, point information, e.g. stations, can be added in a fifth step by a map matching operation to enable station-to-station routing. Due to the limited space, this step is not covered in this article.

3.1 *Buffering of the Tracks*

In the first step, a buffer operation is performed on every track segment of the input data. The buffer width has to be defined manually by the user – the smaller the distance value is chosen, the more single tracks will be created in the output dataset. A big value corresponds thereby to a more generalised result. In the experiments, a typical buffer distance of 12 m was selected in order to span all neighbouring tracks, which corresponds to the tripled value of the normal track distance of 4 m. Subsequently, all buffer polygons are amalgamated into one large polygon, respectively multipolygon in the case of an incoherent track network, with holes.

3.2 *Removal of Holes*

In areas with a high track density and many parallel tracks, e.g. at marshalling yards or big stations, some holes may occur in the total polygon when the gap between two tracks is slightly higher than the chosen buffer distance in step one. Those holes lead to disruptive splits in the resulting graph, because an output line will be created on both sides of the hole. This effect can be avoided by a removal of holes which have a size smaller than a defined threshold. The threshold size has to be chosen carefully – too big values may destroy useful information while small values lead to many forks in the graph. In practice, values between 4000 m^2 and 10000 m^2 have lead to

good results, depending on the desired level of detail. For the results shown in this work a threshold of 7500 m^2 was used.

3.3 *Triangulation of the Polygon*

In order to obtain a line dataset based on the created polygon, an area collapse mechanism is needed which returns the *skeleton* of the polygon. Several different approaches for a skeletonisation exist in the literature. A good overview is given for example by Haunert & Sester (2008).

For the algorithm presented in this paper it is required to use the method of skeletonisation by polygon triangulation, as proposed by Chithambaram et al. (1991). A brief description of the procedure is given in section 3.4.

The triangulation itself is based on a constrained Delaunay triangulation of the polygon, where triangles outside the polygon are removed. The more homogeneous the triangles are shaped, the smoother the skeleton gets. Therefore, the algorithm uses a *Conforming Delaunay Triangulation,* where additional *Steiner Points* are inserted into the polygon edges. For further details we refer to Bern & Eppstein (1992).

3.4 *Creation of the Skeleton*

A conventional skeleton based on a triangulated polygon is created by an analysis of the triangles and distinguishes two types of triangles: Normal triangles (1) have at least one common edge with the polygon boundary, while interior triangles (2) have no edge coincident with the polygon and occur on junctions. The skeleton edge is then created for every triangle by linking the midpoints of the interior triangle edges. When triangles of type (2) are processed, a centre point of the triangle is inserted and linked with all three midpoints of the triangle edges.

In contrast to a conventional skeleton operation, the proposed algorithm uses also the topologic relations from the original tracks. All triangles are processed iteratively and the following steps are executed:
1) track search,
2) repairing topology errors,
3) analysis of the track connectivity,
4) inserting connection lines,
5) at interior triangles: track tracing.

Track search

In order to detect the underlying topology of the tracks, the first step is the retrieval of the affected track data in the area of the currently processed triangle. To avoid a wrong connectivity analysis, it is necessary to cut the tracks at the triangle edges.

Repairing topology errors

Depending on the quality of the input data, topological errors like not correctly connected track segments may occur in the input data and can lead to gross errors in the output data. They can be detected by measuring the distance and angle difference between track line endings and/or vertices – if the distance is very small and the track segments have an approximately similar direction, an error may be present. It can be repaired by connecting the separated nodes.

Analysis of the connectivity

The topologically clean tracks are then investigated with regard to the connectivity. Fig. 6 shows exemplarily three possible track constellations in a triangle:
a) two tracks simply pass the triangle,
b) a track merges (Branch),
c) a trac splits (Branch).

The connectivity analysis contains mainly the partition of the tracks into distinct track sets. Distinct means that a track set has no connection to another track set.

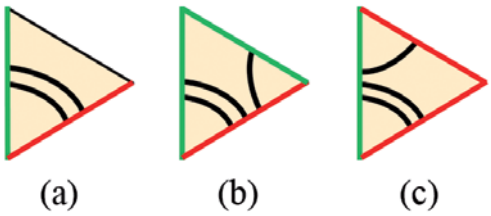

Fig. 6: Examples of different track constellations in a triangle, green: input edge, red: output edge.

Inserting connection lines

This information is now used to determine the necessary connection lines in the output graph. In most cases like in Fig. 6a, this is a trivial task where just the centres of track intersections at two triangle edges are connected. The only exception occurs at interior triangles, which marks the initial situation for a track tracing.

Track tracing

Since it is not possible to distinguish branches from crossings in just one single triangle, it is necessary to trace the tracks further until a proof is found that the tracks that are coming from different triangle edges merge (Branch) or divide without any common node in between (Crossing). For such a tracing, the triangle structure provides a good frame condition since the calculations can thus be locally limited.

An interior triangle of type (2) always marks the start of a tracing function if all three edges are crossed by tracks. An example can be seen in Figs. 7 and 8: The green interior triangle labelled with 1 has different tracks crossing each triangle edge, thus a track tracing over the triangles labelled with 2 is necessary until the decision between branch and crossing can be made. Fig. 7 shows the case of a branch where the tracks meet a few triangles further (labelled with 3). In contrast, Fig. 8 illustrates a crossing where the four tracks of the route from top left to the bottom right do not have a common node with the two tracks of the other route until they diverge again in the triangle labelled with 3.

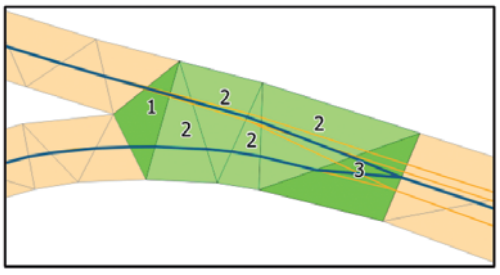

Fig. 7: Branch of two rail routes.

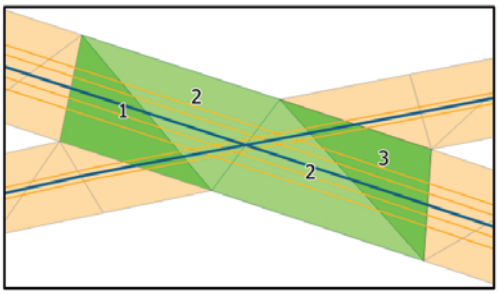

Fig. 8: Crossing of two rail routes.

The proceeding of the track tracing is as follows. At first, all three edges of the starting triangle are classified as *input* or *output edge*. Usually, a starting triangle has two input edges and one output edge where all tracks from both input edges converge, as shown in Fig. 6b. In rare cases it can happen that this assumption is not fulfilled, e.g. when there are direct connections between all three edges. In this case, a tracing is not possible and the algorithm only inserts output edges between the corresponding intersection points.

In all other cases, the following loop is executed:

1) Label distinct track sets All distinct track sets that intersect the same input edge are grouped into a *route track set (RTS)*. This holds also if new tracks accrue during the loop.
2) Go to the neighbouring triangle(s) at the output edge(s) and group the underlying tracks to the RTS.
3) Check for connections All RTS are checked among each other if a connection exists. If so, a branch is present and the RTS are united. If desired by the user, RTS can also be united due to a certain similarity, e.g. if the angle difference and/or distance between the RTS are below a certain threshold.
4) Insert output edges between the intersection centres of the RTS at the triangle edges. Old output edges in the current triangle are removed and overwritten unless a *Collision exit* is present, see below.
5) Check the stop criteria
   - *Branch exit*: Only one RTS remains due to a branch
   - *Crossing exit*: Two RTS leave the triangle through two different output edges
   - *Collision exit*: The current triangle is the end of a tracing from the opposite direction.

Otherwise, if two or more RTS leave through an output edge, continue with step 1.

The track tracing is in principle able to handle an arbitrary number of traced RTS simultaneously. Note that care is necessary when a new tracing overwrites an old tracing but stops at an earlier triangle compared to the old tracing – in this case, the output edges may not match at the triangle edge.

Since the output edges only span the based triangle and are thus relatively short, it is useful to connect those fragments in a final step to create longer polylines.

4 Results

The following examples show the result of processing a German-wide railway dataset obtained from OpenStreetMap. For the calculation, only standard tracks have been used excluding tracks in marshalling and maintenance yards. In Fig. 12 the result network is visualized as a red line on top of an OpenStreetMap background in the area of the main station in Hamburg. It can be seen that the parallel running railway tracks in OSM have been replaced by one single line which follows approximately the medial axis of the tracks.

Fig. 9 shows exemplarily the output of processing a branch with several tracks. Here, the original railway tracks are drawn in orange and the output line is overlaid in blue. Fig. 10 shows a more complex track junction near Kreiensen, Germany, where the original topology is also preserved correctly. In this special case, the stop criterion was a *Collision exit* where the central part was processed from the left side as well as from the right side.

In general, however, it is not always possible to generate a visually attractive appearance in addition to topological correctness. Such visual drawbacks mostly occur at big marshalling yards or junctions with more than three track routes converging, as the complex example of Saarbrücken (Fig. 11) shows. Although the topology of the blue output graph is correct, the visual appearance is not satisfying due to many successive track tracings with overwriting the existing output.

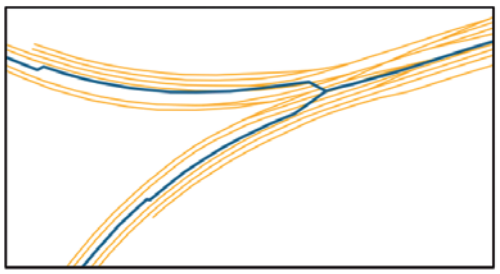

Fig. 9: Example of a simple branch.

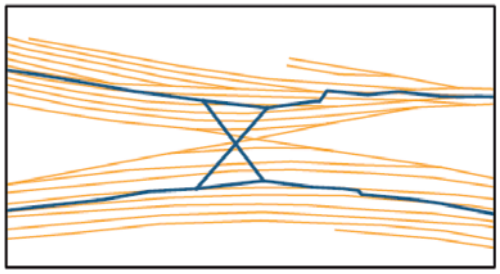

Fig. 10: Example of a more complex branch in Kreiensen, Germany.

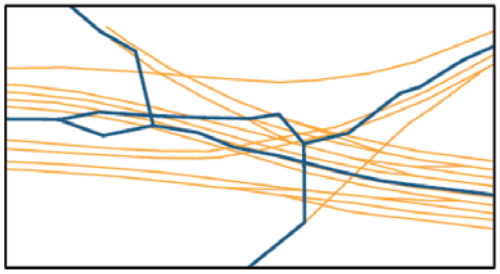

Fig. 11: Example of a very complex track field near Saarbrücken, Germany.

5 Evaluation

Besides the examination of the visual appearance, the results were evaluated concerning the topological correctness and routing ability. The topological correctness of a processed German-wide track network obtained from OSM was estimated by an automatic check for node connections (see Related Work for more information about the test configuration). It yielded only two errors out of 28.528 tested node pairs, which is a rather good result that indicates a highly reliable quality of the topology. On the contrary, it shows also that the algorithm does not work faultlessly since errors

may still appear in rare cases. In various other experiments with different parameter settings, such errors occurred particularly at helical tunnels or huge marshalling yards.

In order to verify the result with respect to the routing ability, it is not sufficient to check only node connections, because other topological errors can as well significantly influence the routing and may result in large detours of the routed trains. Hence, a test routing was carried out. The basis for the test routing was:

- Railway track data from OSM
- Station coordinates from OSM
- Timetable information, accessed at
  www.bahn.de
  www.der-metronom.de

The routing itself was executed by the routing algorithm of the HAFAS journey planner from HaCon. A total of 4 relations in northern Germany have been tested and analyzed (Fig. 13). The evaluation was carried out in two ways: on the one hand manually by visual inspection of the route between the start and end nodes, and on the other hand by calculating the needed train speed between the stations. If the calculated speed of a train rises to unrealistic values, e.g. above 200 km/h for local trains, it can be assumed that this error comes from a topological issue in the routing dataset. The train has to take a detour and thus a longer distance, but the travel time keeps the same, which results in a higher speed.

The result: both the visual inspection of the route and the speed check yielded no problems – all trains could take the assumed route with an appropriate speed.

When processing large datasets, time and memory complexity is an important aspect as it describes how much the time- and memory usage grows with increasing input size. The theoretical complexity mainly determined by the buffering and union steps is $O(n \log n)$. The memory and time usage was determined experimentally. Thereby a near-linear behaviour of both time and memory usage was observed. In our case, the calculation of small datasets (~ 14.000 line segments) took approximately 3 minutes, whereas the whole German railway network (~ 130.000 line segments) required approximately 40 minutes (CPU: Xeon E5 processor with 2,4 GHz).

A drawback in terms of calculation time is the dependence of the processing direction of the tracks; that is, different input datasets result in a different geometry of the output data, even in regions where the original data is congruent. Thus, a tile based partition of the input data in order to parallelize the computation is not directly possible.

6 Conclusion

In this work we presented a new algorithm to derive a routable rail network from detailed railway track data in consideration of the to-

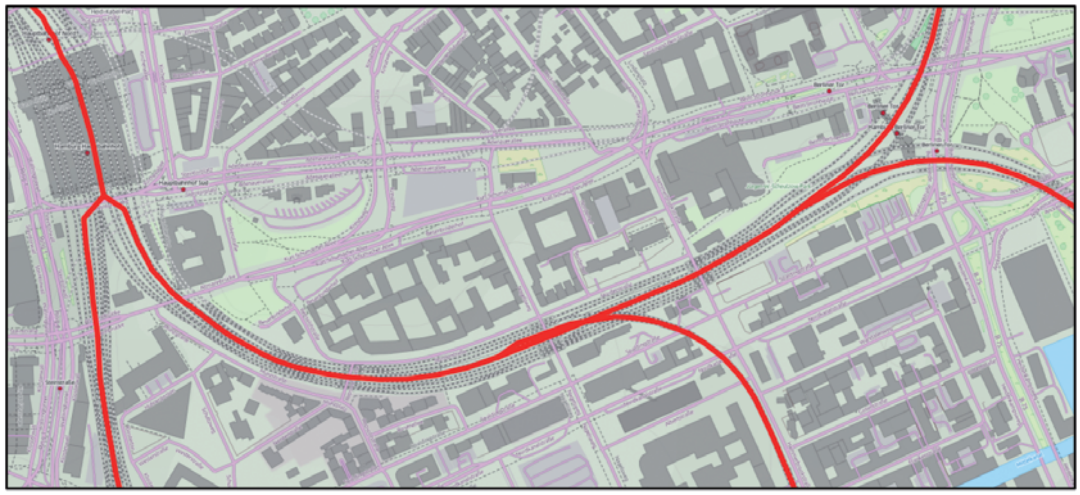

Fig. 12: Output railway network in the area of Hamburg, Germany (background: OpenStreetMap).

pology of the input tracks. The algorithm uses different methods of geometry type change (buffer operation and dimensional collapse) in order to create a representative line of the track routes. The core of the operator is a track tracing mechanism based on triangles in order to distinguish branches from crossings and thus to preserve the topology of the original track network.

Different evaluation approaches like a test routing indicate a very good quality in terms of topological correctness and routing ability of the output graph. The visual appearance of the resulting representative lines is rather good in most cases, although some complex

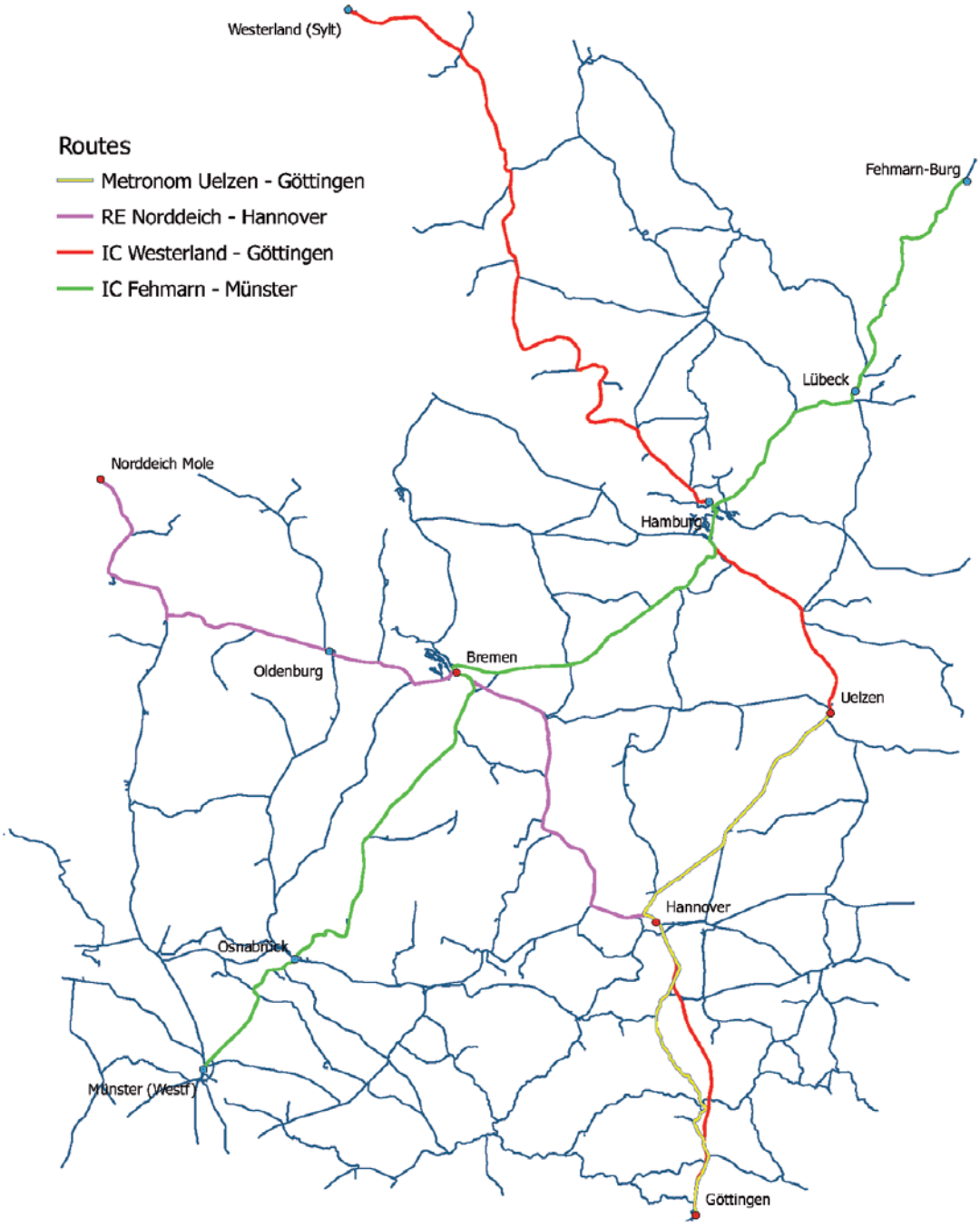

Fig. 13: Routed relations in northern Germany, based on a processed OSM dataset.

junctions may result in a confusing output line constellation. At this point, the visual appearance could benefit from an additional post processing which preserves the topology.

A drawback of the presented method is though the dependence of the processing direction, which complicates a parallelization of the computation. For this purpose, approaches have to be used that deal with overlapping parts (see e.g. Thiemann et al. 2013).

References

Bern, M. & Eppstein, D., 1992: Mesh generation and optimal triangulation. – Computing in Euclidean geometry **1:** 23–90.

Biagioni, J. & Eriksson, J., 2012: Map inference in the face of noise and disparity. – 20th International Conference on Advances in Geographic Information Systems ACM: 79–88.

Cao, L. & Krumm, J., 2009: From GPS traces to a routable road map. – 17th ACM SIGSPATIAL **2009:** 3–12.

Chithambaram, R., Beard, K. & Barrera, R., 1991: Skeletonizing polygons for map generalization. – Technical Papers ACSM-ASPRS Convention, Cartography and GIS/LIS **2:** 44–54.

Destatis (Deutsches Statistisches Bundesamt), 2013: Busse und Bahnen mit neuem Fahrgastrekord. https://www.destatis.de/DE/PresseService/Presse/Pressemitteilungen/2014/04/PD14_127_461.pdf (15.9.2014).

Edelkamp, S. & Schrödl, S., 2003: Route planning and map inference with global positioning traces. – Computer Science in Perspective, Springer: 128–151.

Haunert, J.H. & Sester, M., 2008: Area collapse and road centerlines based on straight skeletons. – Geoinformatica **12** (2): 169–191.

Lee, J., Han, J. & Whang, K., 2007: Trajectory clustering: a partition-and-group framework. – ACM SIGMOD International Conference on Management of Data.

Neis, P., Zielstra, D. & Zipf, A., 2011: The Street network evolution of crowdsourced maps: OpenStreetMap in Germany 2007–2011. – Future Internet **4** (1): 1–21.

Shea, K.S. & McMaster, R.B., 1989: Cartographic generalization in a digital environment: When and how to generalize. – AutoCarto **1989:** 56–67.

Thiemann, F., Werder, S., Globig, T. & Sester, M., 2013: Investigations into partitioning of generalization processes in a distributed processing framework. – 26. International Cartographic Conference, Dresden, http://www.icc2013.org/_contxt/_medien/_upload/_proceeding/395_proceeding.pdf (15.9.2014).

Thom, S., 2005: A Strategy for collapsing OS Integrated Transport Network (ITN) dual carriageways. – 9th ICA Workshop on Generalisation and Multiple Representation, http://generalisation.icaci.org/images/files/workshop/workshop2005/Thom.pdf (15.9.2014).

Thomson, R.C., & Richardson, D.E., 1999: The 'good continuation' principle of perceptual organization applied to the generalization of road networks. – ICA 19th International Cartographic Conference.

Zhang, L., Thiemann, F. & Sester, M., 2010: Integration of GPS Traces with Road Map. – Workshop on Computational Transportation Science in conjunction with ACM SIGSPATIAL, San Jose, CA, USA.

Address of the Authors:

M.Sc. Paul Czioska, Dipl.-Ing. Frank Thiemann, Prof. Dr.-Ing. Monika Sester, Leibniz Universität Hannover, Institut für Kartographie und Geoinformatik (IKG), Appelstr. 9A, D-30167 Hannover, Tel.: +49-511-762-5422, Fax: +49-511-762-2780, e-mail: {czioska} {thiemann} {sester} @ikg.uni-hannover.de

Robin Giese, Dr. Hermann Vogt, HaCon Ingenieurgesellschaft mbH, Lister Str. 15, D-30163 Hannover, Tel.: +49-511-33699-0, Fax: +49-511-33699-99, e-mail: {robin.giese} {hermann.vogt} @hacon.de

Manuskript eingereicht: Juni 2014
Angenommen: Oktober 2014

Berichte von Veranstaltungen

Symposium der ISPRS Commission IV, 14. – 16. Mai 2014, Suzhuo, China

Das ISPRS Symposium der Kommission IV wurde vom 14. bis 16. Mai im Marriott Hotel in Suzhou City, China, veranstaltet. Das Symposium fand damit nur wenige Tage vor dem ISPRS Symposium der Kommission VI (*Data, Information, and Knowledge Sharing for Geo-Education*) in Wuhan, China, statt, so dass es für Interessierte möglich war, beide Symposien mit einer Reise zu besuchen.

Insgesamt nahmen 320 registrierte Teilnehmer aus 17 Ländern an dem Symposium teil. Es wurden 129 Beiträge eingereicht. Diese wurden in 19 Vortragssitzungen (86 Vorträge) und zwei Postersitzungen (43 Vorträge) vorgestellt. Nach einer wissenschaftlichen Begutachtung wurden 83 Beiträge in den ISPRS Archives und 15 Beiträge in den peer-reviewed ISPRS Annals veröffentlicht. Während des Symposiums fand weiterhin eine technische Messe mit acht Ausstellern statt.

Das Symposium startete mit einer Eröffnungszeremonie (siehe Abb. 1), die von Jie Jang, Präsidentin der Kommission IV, geleitet wurde. Christian Heipke, Generalsekretär der ISPRS, überbrachte die Grußworte des ISPRS Councils. Anschließend begrüßte Pende Li, stellvertretender Generaldirektor der „National Administration of Surveying", die Gäste und stellte eine kurze Übersicht über aktuelle Entwicklungen aus dem Bereich der Geomatik in China vor. Danach hielt der Direktor des „Jiangsu Bureau of Surveying and Mapping" und zugleich stellvertretender Bürgermeister von Suzhou City eine Willkommensansprache im Namen der lokalen Regierung. Abschließend übergab Marguerite Madden, zweite Vizepräsidentin der ISPRS, im Namen der ISPRS Foundation Reisestipendien an zwei Studenten aus Russland und Deutschland, wonach Jun Chen, Präsident der ISPRS, das Symposium und die Ausstellung für eröffnet erklärte.

Auf die Eröffnungszeremonie folgte eine Keynote-Sitzung mit drei Vorträgen. Der erste Vortrag wurde von Deren Li, Wuhan University, mit dem Titel *Ortsbezogene Dienste basierend auf Street-View-Karten* gehalten. Danach folgte ein Vortrag von Georg Gartner, Präsident der International Cartographic Association (ICA), über serviceorientierte Kartographie und ortsbezogene Dienste. Der dritte Vortragende war Bryant Austin vom Cosmos Studio USA, der sich mit der Thematik beschäftigte, wie Fotomosaike im Maßstab 1:1 von Walen erzeugt werden können.

Am Nachmittag des ersten Tages wurden zwei Plenarsitzungen abgehalten. Die erste Sitzung wurde von John Trinder, Ehrenmitglied der ISPRS, geleitet. Diese begann mit einem Vortrag von der nächsten ISPRS Kongressdirektorin Lena Halounová. Sie stellte die aktuellen Vorbereitungen zum nächsten ISPRS-Kongress in Prag vor und rief zur zahlreichen Teilnahme auf. Gottfried Konecny, Ehrenmitglied der ISPRS und Co-Leiter der Arbeitsgruppe IV/2, präsentierte die Ergebnisse eines u.a. auch von der UN unterstützen Fragebogens zum Thema *Globale Kartierung und Fortführung*. Danach berichtete Jun Chen über eine Landnutzungskartierung in China. Abschließend zeigte Marguerite Madden einen Ansatz zur Geovisualisierung und -analyse von Tierhabitaten.

Die zweite Plenarsitzung wurde von Jun Chen geleitet. Zunächst berichtet Jan-Peter Muller, Leiter der ISPRS Arbeitsgruppe IV/3, über den Status der *Committee on Earth Observation Satellites Working Group on Calibration and Validation (CEOS-WGCV): Terrain Mapping from Satellites*. Anschließend präsentierte E. Pattabhi Rama Rao, Leiter der ISPRS Arbeitsgruppe IV/4, Anwendungen von Geotechnologien im Bereich *Ocean Information and Advisory Services*. Bert Veenendaal, Leiter der ISPRS Arbeitsgruppe IV/5, stellte Entwicklungen für ein flexibles Bildungsrahmenwerk für die Ausbildung im Geomatik-Bereich vor. In den abschließenden Vorträgen berichteten Sisi Zlatanova, Leiterin der ISPRS Arbeitsgruppe IV/7, über Chancen und Herausforderungen im Bereich der 3D-Innenraummodellierung und -navigation

DOI: 10.1127/pfg/2015/0257 1432-8364/15/0257 $ 1.50

und XIN REN vom Nationalen Astronomischen Observatorium der Chinesischen Akademie der Wissenschaften über die Mission der chinesischen Mondsonde Chang'E3.

In den folgenden zwei Tagen wurden 16 Vortragssitzungen mit 73 Vorträgen und zwei Postersitzungen mit 43 Präsentationen abgehalten. Die Schwerpunkte waren dabei Methoden zur Fortführung und Verifikation von Geodatenbanken, Globaler Status der Kartierung und Fortführung von Geodatenbanken, Globale Interoperabilität von Höhenmodellen, Geodateninfrastrukturen, Web- und Cloudbasierte Dienste und Anwendungen, Sensor Web und Web der Dinge, 3D-Innenraummodellierung und -navigation, Planetare Kartierung und Geodatenbanken, Rechenoptimierung von Geodatenbanken und ortsbezogenen Diensten, Globale Landnutzungskartierung

Abb. 1: Impressionen der Eröffnungszeremonie

und Services sowie Ortsbezogene Dienste und ubiquitäre Kartographie.

Zusammenfassend war das Symposium eine sehr gute Möglichkeit zum gegenseitigen Informationsaustausch. Dazu trug auch der Empfang am Abend des ersten Tages bei, bei dem traditionelle chinesische Musik dargeboten wurde. Mit Suzhou City wurde zudem ein sehr attraktiver Veranstaltungsort mit einer über 2500 Jahre alten Geschichte gewählt, welcher den Aufenthalt sehr angenehm machte.

Volker Walter, Stuttgart

Hochschulnachrichten

Leibniz Universität Hannover

Dissertation von Gholam Reza Dini

Herr Gholam Reza Dini, M.Sc., wurde am 18.7.2014 an der Fakultät für Bauingenieurwesen und Geodäsie der Leibniz Universität Hannover mit der Arbeit „*Toward an Automatic Solution for Updating Building Databases Using Space-borne Stereo Imaging*“ zum Dr.-Ing. promoviert.

1. Referent: Prof. Dr.-Ing. habil. Christian Heipke, Leibniz Universität Hannover
2. Referent: Prof. Dr.-Ing. habil. Monika Sester, Leibniz Universität Hannover
3. Referent: Prof. Dr.-Ing. Markus Gerke, Universität Twente, Enschede

Kurzfassung:
Aufgrund der Entwicklung von hochauflösenden, satellitengetragenen, stereoskopischen Sensoren werden heutzutage auch Digitale Oberflächenmodelle (DOMs), die durch digitale Bildzuordnung generiert wurden, immer häufiger verwendet, besonders für das Kartieren von Stadtgebieten. Diese Arbeit beschäftigt sich mit der automatischen Aktualisierung von Gebäudedatenbanken mittels hochauflösenden, satellitengetragenen Stereobildpaaren unter Einbindung einer möglicherweise veralteten GIS Datenbasis. Die Methode des semi-global matching (SGM) wurde verwendet, um Digitale Oberflächenmodelle (DOM) und daran anschließend normalisierte Oberflächenmodelle (nDOM) abzuleiten. Die Aktualisierung von Gebäudedatenbanken wird hierzu in zwei Hauptteile unterteilt: (1) ein System zur Erkennung von 3D Änderungen der Gebäude und (2) ein System zur Erfassung der Abgrenzung der neuen Gebäudegrundrisse bzw. deren Aktualisierung.

Zwei verschiedene Szenarien werden getestet, um das Potenzial von hochauflösenden Stereobilddaten für die Aktualisierung von Gebäuden zu evaluieren: ein Vergleich zweier Oberflächenmodelle (DOM vs. DOM) und eine Vergleich von Oberflächenmodell zu GIS Daten.

Im ersten Szenario werden zwei DOM subtrahiert, anschließend werden Gebiete größer als 2,5 m² betrachtet. Es wird angenommen, dass größere Höhenunterschiede vertikale Änderungen darstellen. Vor der DOM Subtraktion wird eine relative Referenzierung durchgeführt, um Fehler der Bildorientierung auszugleichen. Zusätzlich ist es notwendig, Artefakte aus der Bildzuordnung durch Filtermethoden zu entfernen, um die Anzahl der Fehlalarme zu minimieren. Abschließend wird eine morphologische Filterung mit Schwellwerten für Höhe, Form und Größe durchgeführt, um das Ergebnis zu verbessern.

Das zweite Szenario verwendet alle Pixel oberhalb des Schwellwertes von 2,5 m im nDOM für die Generierung von Gebäudehypothesen. Darauffolgend werden alle Gebäudepolygone aus der Datenbank mit den Hypothesen verglichen. Ein Gebäudepolygon wird dabei verifiziert, wenn es zumindest zu 75% von der zugehörigen Hypothese belegt ist. Die verifizierten Polygone entsprechen dann weiterhin den Gebäudegrenzen.

Im Falle einer Gebäudeveränderung werden die neuen Gebäudegrundrisse auf zwei unterschiedliche Methoden extrahiert: 3D-Kanten-

zuordnung und 3D-Segmentation. Um eine 3D-Kantenzuordnung durchzuführen, werden zuerst einzelne Kanten in den Epipolarbildern durch Anwendung des Canny-Operators detektiert. Nachdem kurze Kanten entfernt und gerade Linien extrahiert wurden, können die am besten korrespondierenden Linien mittels verschiedener Geometrie- und Lageeinschränkungen gefunden werden. Schließlich werden Topologiebeziehungen der abgeleiteten 3D-Kanten genutzt, um die Gebäudegrundrisse mittels einer Quaderanpassung zu rekonstruieren. In der vorgestellten 3D Segmentationsmethode wird der Startbereich durch die Nutzung eines Schwellwertes von 2,5 m für das nDOM definiert. Die Segmentierung ist ein iterativer Prozess und wird wiederholt, bis keine Verbesserung der Gebäudegrenzen mehr erreicht wird. Schlussendlich werden die Segmente in eine rechteckige Form gebracht, um die Gebäudegrundrisse mit den Neubauten zu aktualisieren.

In der Testphase der Methode wurden IKONOS und GeoEye-1 Stereobilder von Riad, der Hauptstadt Saudi-Arabiens, verwendet. Die hier verwendete Methode eignet sich für einfache rechteckige Gebäude mit flachen Dächern, wie im Testgebiet vorhanden. Eine Evaluierung der Ergebnisse mittels Vergleichen zu Referenzdaten hat gute Ergebnisse gezeigt. Die Rauschunterdrückung verringert die Anzahl der Fehlalarme um etwa 32%, die Anzahl der aufgedeckten Änderungen wurde um ca. 15% erhöht. Eine quantitative Evaluierung der Ergebnisse hat gezeigt, dass im ersten und zweiten Szenario die geringere GSD der IKONOS Daten einen signifikanten Einfluss auf die Häufigkeit von Fehlalarmen hat. Unsere Tests zur 3D Kantenzuordnung liefern nur gute Ergebnisse, wenn die Gebäude groß genug sind, eine einfache Form haben und große Kontrastunterschiede gegenüber dem Hintergrund besitzen. Ist dies nicht der Fall, sind die Ergebnisse fehlerhaft und unvollständig. Im Vergleich dazu liefert die 3D Segmentierung der Gebäudedächer bessere Ergebnisse im Hinblick auf die Vollständigkeit, allerdings versagt die Methode, wenn ein Gebäude einen sehr geringen Kontrast gegenüber dem Hintergrund aufweist.

Die Dissertation ist in der Schriftenreihe „Wissenschaftliche Arbeiten der Fachrichtung Geodäsie und Geoinformatik der Leibniz Universität Hannover“ (ISSN 0174-1454) als Heft Nr. 314 erschienen.

Neue persönliche Mitglieder

Die DGPF begrüßt herzlich die neuen persönlichen Mitglieder:
Lena Albert, Hannover
Dr. Muhamad Alrajhi, Riyadh, Saudi Arabien
Dr. Damian Bargiel, Darmstadt
Yasmin Dadas, Berlin
Björn Dullek, Berlin
Prof. Dr. Jan-Henrik Haunert, Osnabrück
Prof. Dr. Bernhard Höfle, Heidelberg
Prof. Joel Igbokwe, Awka, Nigerien
Prof. Dr. Martin Kada, Wallenhorst
Izabella Karut, Berlin
Prof. Dr. Thomas Klauer, Lampertheim
Tobias Klinger, Hannover
Dr. Buhalqem Mamtimin, Mainz
Tomasz Oberski, Świeszyno, Polen
Prof. Dr. Christine Pohl, Johor Bahru, Malaysia
Anna Poznanska, Berlin
Martin Reich, Hannover
Eric Schmalen, München
Maurice Schönert, Berlin
Akarsh Seggemu, Berlin
Zhan Shi, Nanjing Jiangsu, China
Maximilian Sindram, Zorneding
Nora Tilly, Köln
Jakob Unger, Hannover
Kerstin Wegner, Nürnberg
Zhihang Yao, München
Birgit Zander, Berlin

Neuerscheinung

Kummer, K., Kötter, T. & Eichhorn, A. (Hrsg.) 2015: *Das deutsche Vermessungs- und Geoinformationswesen 2015.* Wichmann-Verlag, 1042 Seiten. ISBN 978-3-87907-547-8

Das Jahrbuch bildet eine Klammer für die in den letzten Jahren ausgeweiteten Bereiche Vermessung und Geoinformation. Es bietet in dieser Form eine Zusammenschau der einzelnen Fachthemen, die bislang nur weit verstreut, d.h. nicht zusammengefasst, in einem Gesamtwerk zu finden waren. Die Ausgabe 2015 widmet sich schwerpunktmäßig u.a. den Themen gesellschaftliche Verankerung und institutionelles Gefüge, Aufgabenfelder und Wirkungsbereiche, Technische Netzwerke und Transfer, Forschung und Lehre.

Veranstaltungskalender

2015

4.–5. Februar: **Oldenburger 3D Tage** in **Oldenburg**. jade-hs.de/fachbereiche/bauwesen-und-geoinformation/geoinformation/oldenburger-3d-tage

25.–27. Februar: **CIPA + 3D-ARCH'2015** in **Avila**, Spanien. 3d-arch.org

16.–18. März: **35. Jahrestagung der DGPF** in **Köln**. dgpf.de/con/jt2015.html

23.–27. März: **ESA FRINGE Workshop** in **Frascati**, Italien. seom.esa.int/fringe2015

25.–27. März: **PIA15 + HRIGI: Joint Conference of Photogrammetric Image Analysis and High Resolution Earth Imaging for Geospatial Information 2015** in **München**. pf.bgu.tum.de/isprs/pia15/index.html

30. März–1. April: **JURSE – IEEE Joint Urban Remote Sensing Event 2015** in **Lausanne**, Schweiz. jurse2015.org

11.–15. Mai: **ISRSE36 – International Symposium on Remote Sensing of the Earth** in **Berlin**. isrse36.org

7.–12. Juni: **CVPR 2015 – Conference on Computer Vision and Pattern Recognition 2015** in **Boston**, USA. pamitc.org/cvpr15/

5.–11. Juli: **Innsbruck Summer School on Alpine Research 2015: Close Range Sensing Techniques in Alpine Terrain** in **Obergurgl**, Österreich. uibk.ac.at/geographie/summerschool

26.–31. Juli: **IGARSS 2015 – International Geoscience and Remote Sensing Symposium 2015** in **Mailand**, Italien. igarss2015.org

23.–28. August: **ICC – International Cartographic Conference** in **Rio de Janeiro**, Brasilien. icc2015.org

30. August – 2. September: **UAV-g: Unmanned Aerial Vehicles in Geomatics** in **Toronto**, Kanada. uav-g2015.org

15. –17. September: **INTERGEO** in **Stuttgart**. intergeo.de

6.–9. Oktober: **GCPR (DAGM): German Conference on Pattern Recognition** in **Aachen**.

7.–13. Dezember: **ICCV 2015 – International Conference for Computer Vision 2015** in **Santiago**, Chile.

Weitere Konferenzen und Workshops finden sich beispielsweise unter:
isprs.org/calendar
conferences.visionbib.com

Korporative Mitglieder

Firmen

AEROWEST GmbH
AICON 3D Systems GmbH
aphos Leipzig AG
ASTEC GEODATA GmbH
Bernhard Harzer Verlag GmbH
Black Bridge AG
Blom Deutschland GmbH
Brockmann Consult GmbH
bsf swissphoto GmbH
Büro Immekus
DB Netz AG
DELPHI IMM GmbH
Deutsches Bergbau-Museum
EFTAS Fernerkundung Technologietransfer GmbH
ESG Elektroniksystem- und Logistik-GmbH
Esri Deutschland GmbH
EUROPEAN SPACE IMAGING
Eurosense GmbH
Exelis Visual Information Solutions GmbH
fokus GmbH
GAF GmbH
GeoCart Herten GmbH
Geoinform. & Photogr. Engin. Dr. Kruck & Co. GbR
geoplana Ingenieurgesellschaft mbH
GEOSYSTEMS GmbH
GGS - Büro für Geotechnik, Geoinformatik, Service
Hansa Luftbild AG
Herbert Wichmann, VDE Verlag GmbH
IAGB mbH
IGI - Ingenieur-Gesellschaft für Interfaces mbH
ILV-Fernerkundungs GmbH
Infoterra GmbH
INVERS - Industrievermessung & Systeme
Linsinger ZT GmbH
Leica Geosystems GmbH
Luftbilddatenbank Dr. Carls GmbH
map/x/tek
Messbildstelle GmbH
Microsoft Photogrammetry
MILAN Geoservice GmbH
M.O.S.S. Computer Grafik Systeme GmbH
PHOENICS GmbH
PMS - Photo Mess Systeme AG
RIEGL Laser Measurement Systems GmbH
RWE Power AG, Geobasisdaten/Markscheidewesen
technet GmbH
Terra-Messflug GmbH
topometric GmbH
TRIGIS GmbH
Trimble Germany GmbH
trimetric 3D Service GmbH
Z/I Imaging Ltd.

Behörden

Amt für Geoinformationswesen der Bundeswehr
Bayerische Landesanstalt für Wald und Forstwirtschaft
Bundesamt für Kartographie und Geodäsie
Bundesministerium für Ernährung, Landwirtschaft und Verbraucherschutz
Hessisches LA für Bodenmanagement und Geoinformation
Innenministerium NRW, Gruppe Vermessungswesen
Institut für Umwelt- und Zukunftsforschung
LA für Geoinformation und Landentwicklung, BW
LA für Vermessung und Geoinformation, Bayern
LA für Vermessung und Geoinformation, Schleswig-Holstein
LB Geoinformation und Vermessung, Hamburg
LB für Küstenschutz, Nationalpark und Meeresschutz, SH
Landeshauptstadt Düsseldorf, Vermessungs- und Liegenschaftsamt
Landesvermessung und Geobasisinformation Niedersachsen
Märkischer Kreis, Vermessungs- und Katasteramt
Regierungspräsident Tübingen, Abt. 8 Forstdirektion
Regionalverband Ruhr
Staatsbetrieb Sachsenforst
Stadt Köln, Amt für Liegenschaften, Vermessung und Kataster
Stadt Wuppertal, Vermessung, Katasteramt und Geodaten
Thüringer LA für Vermessung und Geoinformation

Hochschulen

BTU Cottbus, Lehrstuhl für Vermessungskunde
FH Frankfurt a.M., FB 1, Studiengang Geoinformation
FH Mainz, Institut für Raumbezogene Informations- und Messtechnik
HCU HafenCity Universität Hamburg, Geomatik
HfT Stuttgart, Vermessung und Geoinformatik
HS Bochum, FB Vermessung und Geoinformatik
HS Karlsruhe, Fakultät für Geomatik
HTW Dresden, FB Vermessungswesen/Kartographie
Jade Hochschule, Institut für Angewandte Photogrammetrie und Geoinformatik
LUH Hannover, Institut für Kartographie und Geoinformatik
LUH Hannover, Institut für Photogrammetrie und Geoinformation
MLU Halle, FG Geofernerkundung
Ruhr-Uni Bochum, Geographisches Institut
RWTH Aachen, Geodätisches Institut
TU Bergak. Freiberg, Institut für Markscheidewesen und Geodäsie
TU Berlin, Computer Vision & Remote Sensing
TU Berlin, Institut für Geodäsie und Geoinformationstechnik
TU Braunschweig, Institut für Geodäsie und Photogrammetrie
TU Clausthal, Institut für Geotechnik und Markscheidewesen
TU Darmstadt, Institut für Geodäsie, FG Fernerkundung und Bildanalyse
TU Dresden, Institut für Photogrammetrie und Fernerkundung
TU München, FG Photogrammetrie und Fernerkundung
TU Wien, FG Photogrammetrie und Fernerkundung
Uni Bonn, Institut für Photogrammetrie
Uni Göttingen, Abt. Waldinventur und Fernerkundung
Uni Heidelberg, IWR Interdisziplinäres Zentrum für Wissenschaftliches Rechnen
Uni Kassel, FG Grünlandwissenschaften und Rohstoffe
Uni Kiel, Geographisches Institut
Uni Stuttgart, Institut für Photogrammetrie
Uni Trier, Institut für Umweltfernerkundung und Geoinformatik
Uni Würzburg, Geographisches Institut
Uni zu Köln, Geographisches Institut